LUND UNIVERSITY

Light Propagation and Gas Absorption Studies in Turbid Media Using Tunable Diode Llaser Techniques

Mei, Liang

2014

Light Propagation and Gas Absorption Studies in Turbid Media Using Tunable Diode Laser Techniques

Liang Mei

Doctoral Thesis
2014

Light Propagation and Gas Absorption Studies in Turbid Media
Using Tunable Diode Laser Techniques

Printed in Sweden by Media-Tryck, Lund, 2014

Atomic Physics Division
Department of Physics
Faculty of Engineering, LTH
Lund University
P.O. Box 118
SE–221 00 Lund
Sweden

http://www.atomic.physics.lu.se/

ISSN 0281-2762
Lund Reports on Atomic Physics, LRAP-486

ISBN: 978-91-7473-907-7 (print)
ISBN: 978-91-7473-908-4 (pdf)

To my family

Abstract

Optical absorption spectroscopy is a widely used analytical tool for constituent analysis in many applications. According to the Beer-Lambert law, the transmitted light intensity through a homogeneous medium is an exponential function of the product of the concentration, the total pathlength, and the absorption cross-section of the absorbing substance. By studying the intensity loss at the unique absorption band of the absorbing substance, its concentration can be retrieved. However, this method will encounter some difficulties if the light is not only absorbed but also strongly scattered in the material, e.g., in a turbid medium (biological tissues, porous ceramics, wood), which results in an unknown absorption pathlength. Such a problem can be solved by studying light propagation with different theoretical models, and the scattering and absorption properties are then retrieved. One aim of the present thesis work is to develop a new experimental approach to study light propagation in turbid media – frequency-modulated light scattering interferometry (FMLSI), originating from the well-known frequency-modulated continuous-wave technique in telecommunication field. This method provides new possibilities to study optical properties and Brownian motion simultaneously, which is particularly useful in biomedical applications, food science, and for colloidal suspensions in general.

Another important application of absorption spectroscopy is to monitor gas concentration in turbid media, where the gas absorption pathlength is *a priori* unknown due to heavy light scattering in the porous medium. The technique is referred to as gas in scattering media absorption spectroscopy (GASMAS), and is based on the principle that the absorption spectrum of gases is much narrower than that for the solid- or liquid-phase host materials. By linearly scanning the wavelength of the light source across an absorption line of the gas and examining the absorption imprint superimposed on the transmitted light signal, the very weak intensity loss due to the gas of interest can be measured for gas concentration assessment.

In order to obtain the absolute gas concentration, a focus in the present thesis work is to determine the gas absorption path-

length in turbid media. The FMLSI technique is proposed to obtain the mean optical pathlength – the total pathlength through both the pores and the matrix material. The combined method of the FMLSI and GASMAS techniques is then developed to study porous media, where an average gas concentration in the porous media can be obtained. A conventional method for pathlength or optical properties determination – frequency domain photon migration – is also combined with the GASMAS technique to study the total gas absorption pathlength and the porosities of ceramics, which, as a result, also contributes to further understanding of light propagation in porous media. Another method is also proposed to get the absolute gas concentration without knowing the optical pathlength. It is based on absorption line shape analysis – relying on the fact that the line shape depends upon the concentration of the buffer gas. This method is found to be very useful for, e.g., gas concentration monitoring in food packaging.

Populärvetenskaplig Sammanfattning

Gaser är viktiga i de mest skilda sammanhang, inte minst inom energi-, miljö- och medicinområdena. Naturgas har en viktig del i energiförsörjningen. Atmosfärens gaser står i nära koppling till livsprocesser i människor, djur och växter. Gasformiga föroreningar ställer till stora problem. Inom medicinen är syrgas livsviktig, men även andra gaser kan utnyttjas inom anestesi och för analys av sjukdomstillstånd. Mätmetoder för gaser är viktiga, och tekniker som är baserade på optiska metoder är särskilt kraftfulla. Oftast finns gasen fritt, men ibland är den innesluten i porer i olika material. Då har det varit svårt att studera den. Föreliggande avhandling beskriver studier av gas, som finns i porer eller större inneslutningar i en mängd material, t.ex. trä, keramik, livsmedel, eller i medicinska sammanhang, t.ex. bihålor eller lungor. Undersökningar av dylik gas är ett forskningsområde som nyligen utvecklats i Lund, och som synes ha många tillämpningar. Laserspektroskopiska metoder används, dvs man utnyttjar en laser, vars färg kan ändras så att men successivt kan komma i kontakt med olika av gasens energinivåer och därigenom få ett karakteristiskt fingeravtryck av den. Eftersom porösa material ej är homogena sker en starkt ljusspridning inom materialet, vilket leder till att den väg, som ljuset tillryggalägger genom provet blir odefinierad – båda korta och långa vägsträckor finns samtidigt i en viss fördelning. Detta gör att en bestämning av gaskoncentrationen blir mycket mera komplicerad än i det konventionella fallet, där ljuset går en bestämd sträcka, genom t.ex. en kyvett. Avhandlingen handlar om metoder för att trots de föreliggande svårigheterna lösa problemet, och ett antal olika tillvägagångssätt presenteras. Att göra referensmätningar med känd gaskoncentration, eller att samtidigt mäta två gaser, där den enas koncentration är känd (t.ex vattenånga, vars koncentration bestäms av temperaturen) medger att koncentrationen för den sökta gasen kan fastställas. Ibland kan detta inte praktiskt genomföras, och då erfordras andra angreppssätt. Genom

att sända mycket korta ljuspulser genom provet och uppmäta ljuspartiklarnas olika ankomsttider till detektorn kan den effektiva väglängden genom det spridande provet bestämmas. Ett problem är då att gängse utrustning för detta är helt annorlunda är den som används för gasmätningen, vilket gör tillvägagångssättet komplicerat och kostsamt. Inom ramen för avhandlingen har istället utvecklats alternativa metoder, som utnyttjar den smalbandiga och kontinuerligt arbetande halvledarlaser, som ändock används i gasmätningen. Bara lite extrautrustning med känd och kostnadseffektiv radiofrekvens-teknik behövs. En metod bygger på interferometri, där olika ljuskomponenters frekvensavvikelser på grund av tidsfördröjningen genom provet utnyttjas. I ett annat fall moduleras intensiteten på lasern mycket snabbt, och fasförskjutningar i det detekterade ljuset, som fördröjts, bestäms. I alla dessa metoder är det dock den totala vägsträckan, även den genom det i sammanhanget ointressanta fasta materialet, som mäts. Ofta kan dock den intressanta vägsträckan relateras till mätresultatet. Speciellt har porositeten i olika typer av keramer kunnat studeras. Slutligen visas, att man kan använda små förändringar i den uppmätta spektroskopiska linjeformen för att bestämma koncentrationen av de i gasen kolliderande molekylerna. Nu kommer inte alls vägsträckan in i bilden och problemet är i princip löst, men istället fordras mycket hög kvalitet på de signaler som uppmäts. Resultatet av avhandlings-arbetet kan göra praktiska tillämpningar inom materialvetenskap, livsmedelsförpackning och medicinsk diagnostik mera kraftfulla.

List of Publications

This thesis is based on the following papers, which will be referred to by their Roman numerals in the text.

I **Gas spectroscopy and optical path-length assessment in scattering media using a frequency-modulated continuous-wave diode laser**
L. Mei, H. Jayaweera, P. Lundin, S. Svanberg, and G. Somesfalean.
Optics Letters **36**, 3036–3038 (2011).

II **Characterization and validation of the frequency-modulated continuous-wave technique for assessment of photon migration in solid scattering media**
L. Mei, P. Lundin, S. Andersson-Engels, S. Svanberg, and G. Somesfalean.
Applied Physics B **109**, 467–475 (2012).

III **Frequency-modulated light scattering in colloidal suspensions**
L. Mei, S. Svanberg, and G. Somesfalean.
Applied Physics Letters **102**, 061104 (2013).

IV **Frequency-modulated light scattering interferometry employed for optical properties and dynamics studies of turbid media**
L. Mei, G. Somesfalean, and S. Svanberg.
in manuscript (2014).

V **Combined optical porosimetry and gas absorption spectroscopy in gas-filled porous media using diode-laser-based frequency domain photon migration**
L. Mei, S. Svanberg, and G. Somesfalean.
Optics Express **20**, 16942–16954 (2012).

VI **Optical porosimetry in wood using oxygen absorption spectroscopy and frequency domain photon migration**
L. Mei, J. Larsson, S. Svanberg, and G. Somesfalean.
Asia Communications and Photonics Conference **AS1E.5**, (2012).

VII **Light propagation in porous ceramics: optical properties and porosity studies using tunable diode laser spectroscopy**
L. Mei, G. Somesfalean, and S. Svanberg.
Applied Physics A **114**, 393–400 (2013).

VIII **Laser spectroscopic gas concentration measurements in situations with unknown optical path length enabled by absorption line shape analysis**
P. Lundin, L. Mei, S. Andersson-Engels, and S. Svanberg.
Applied Physics Letters **103**, 034105 (2013).

IX **Pathlength determination for gas in scattering media absorption spectroscopy**
L. Mei, G. Somesfalean, and S. Svanberg.
Sensors **14**, 3871-3890 (2014).

Abbreviations

ADC	Analog-digital converter
APD	Avalanche photo diode
CEAS	Cavity enhanced absorption spectroscopy
CFD	Constant fraction discriminator
CRDS	Cavity ring-down absorption spectroscopy
CTTD	Cathode transit time difference
DAQ	Data acquisition card
DC	Direct current
DLS	Dynamic light scattering
DWS	Diffusing wave spectroscopy
FDOR	Frequency domain optical reflector
FDPM	Frequency-domain photon migration
FEM	Finite element method
FMCW	Frequency-modulated continuous wave
FMLSI	Frequency modulated light scattering interferometry
FMS	Frequency modulation spectroscopy
GASMAS	Gas in scattering media absorption spectroscopy
GPU	Graphics processing unit
LCI	Low coherence interferometry
LDV	Laser Doppler velocimetry
MCP	Microchannel plate
MOPL	Mean optical pathlength
MTOF	Mean time-of-flight
NICE-OHMS	Noise-immune cavity enhanced optical heterodyne molecular spectroscopy
OFDR	Optical frequency domain reflector
PAS	Photoacoustic absorption spectroscopy
PC	Principal component

PCA	Principal component analysis
PD	Photo diode
PMT	Photomultiplier tube
pptv	part per trillion volume
ppbv	part per billion volume
ppmv	part per million volume
QCL	Quantum cascade laser
RF	Radio frequency
RTE	Radiative transfer equation
SNR	signal-to-noise ratio
SSB	Single sideband
TCSPC	Time-correlated single photon counting
TDLAS	Tunable diode laser absorption spectroscopy
TEC	Thermoelectric cooler
TIA	Transimpedance amplifier
TOF	Time-of-flight
TOFS	Time-of-flight spectroscopy
TTS	Transit time spread
WMS	Wavelength modulation spectroscopy

Contents

Papers

Chapter 1

Introduction

Optical techniques, where light is studied and measured, have found very broad applications due to their high accuracy, high selectivity and non-intrusive property. Absorption spectroscopy, as one of the most important methods in the catalogue of optical techniques, has also found tremendous applications or even provoked new scientific fields, e.g., gas absorption spectroscopy [1], spectrophotometry in chemical [2] and biological [3, 4] applications, astronomical spectroscopy [5] and fundamental atomic/molecular spectroscopy [6]. By examining light attenuation through the absorptive materials, absorption spectroscopy can measure the concentration of the absorbing substance based on the Beer-Lambert law, which states that the light attenuation is dependent upon the product of the concentration and the pathlength. In many of the applications mentioned above, the pathlength through the absorbing substance can be readily obtained since scattering is much weaker than absorption, and the concentration is then retrieved. However, there are also numerous applications where scattering is equally important or even dominant, e.g., in turbid media. Thus, the absorption pathlength becomes unknown, which significantly increases the difficulties of applying absorption spectroscopy, since the concentration and the pathlength are entangled.

The present thesis work focuses on absorption spectroscopy in applications to turbid media. Two research topics are covered. One is to develop a new experimental approach to study light propagation in turbid media, based on which the absorption spectroscopy can be employed to characterize the turbid media. The other one – the main work of the thesis – is to measure the absolute gas concentration enclosed in the pores or cavities of turbid media, e.g., human sinuses, ceramics, and food packages. The enclosed gases can actually be considered as special absorbing substances, which have extremely narrow absorption lines or fingerprint and can be detected by gas absorption spectroscopy. In both

situations, the absorption pathlength is unknown, constituting the main problem of absorption spectroscopy in the application of turbid media, which hopefully could be partly solved by employing different approaches provided in this thesis.

In the following sections, we will start from the basis of absorption spectroscopy – the Beer-Lambert law, and then discuss the challenges and solutions when applying the Beer-Lambert law to turbid media. Furthermore, the applications of absorption spectroscopy towards gas monitoring are introduced in Sect. 1.3. The problem of unknown gas absorption pathlength in turbid media is discussed, and the possible solutions studied in this work are also briefly described. Finally, the aims and conclusions of the present thesis work are summarized.

1.1 Beer-Lambert law

In 1729, Pierre Bouguer pointed out that the transmission of light through a substance has a logarithmic dependence on the absorbance [7], i.e.,

$$\kappa = \log_{10}\left(\frac{I_0}{I}\right). \tag{1.1}$$

Here I and I_0 are the transmitted and incident light intensity, respectively, and κ is the absorbance which is unit-less. Johann Heinrich Lambert later proposed that the absorbance is linearly proportional to the light pathlength L [cm] [8], while August Beer in 1852 suggested that the absorbance is also linearly proportional to the concentration of the substance N [cm^{-3}] [9]. According to the conclusions given by these pioneers, the absorbance is then expressed as

$$\kappa = \frac{\alpha L}{\ln 10} = \frac{\sigma N L}{\ln 10}, \tag{1.2}$$

where $\alpha = \sigma N$ is absorption coefficient [cm^{-1}], and σ is absorption cross section [cm^2] describing the possibility of light being absorbed by the substance, which primarily depends upon the atomic and molecular structures of the substance. With the above two equations, we can then conclude the modern derivation of the Beer-Lambert-Bouguer law based on natural logarithm, which is also often referred to as the Beer-Lambert law:

$$I = I_0 \exp(-\sigma N L). \tag{1.3}$$

If there are many absorbing substances, the total absorption coefficient is then the sum of the individual absorption coefficients, i.e., $\sum_i \sigma_i N_i$. Notably, the absorption coefficient is sometimes denoted by μ_a [cm^{-1}], e.g., to describe the absorption of solid- or liquid-phase material in turbid media.

Obviously, by measuring the loss of light through samples, the concentration of the absorbing substance in the host material can

be deduced if the absorption cross-section and absorption pathlength are known. The species of the absorbing substance can also be identified in some cases due to their unique absorption imprints.

1.2 Absorption spectroscopy in turbid media

One critical prerequisite when applying the Beer-Lambert law is that the absorption pathlength must be known which means that the absorbing medium cannot scatter light. In other words, the Beer-Lambert law is not applicable to turbid media where the light is not only absorbed but also substantially scattered. Unfortunately, turbid media, to some extent, even more widely exist in our daily life compared with the non-turbid materials. The scattering effect, described by the scattering coefficient μ_s [cm^{-1}], frequently dominates over absorption, e.g., in biological tissues probed in the near infrared region. However, by employing different experimental approaches, e.g., time-dependent measurements, and theoretical modeling methods such as diffusion theory and Monte Carlo simulations to study light propagation in turbid media, the absorption and scattering coefficients can be separated. These approaches yield new opportunities of the absorption spectroscopy techniques in the application to turbid media, especially in biomedical field [10–13]. On the other hand, the broadband absorption spectrum can also be resolved to study the constituents of turbid media, e.g., wood materials [14, 15], granular samples or diary products [16–19]. Apart from direct optical diagnosis based on absorption spectroscopy, modeling light propagation or studying the scattering and absorption coefficients is also fundamentally important in many biomedical applications [20–22]. Inspired by the broad applications, one of the aims of the present thesis work is to investigate the possibility of using a new experimental approach – frequency modulated light scattering interferometry (FMLSI) to study light propagation in turbid media; see Papers **II**, **III**, and **IV**.

Aside from applications mentioned above, another motivation of studying light propagation in turbid media is to understand the structure and sometimes dynamics of turbid media, since the scattering coefficient significantly depends on the structure of the turbid media. The possible applications include particle sizes assessment in colloidal suspension [23–25], viscosity or rheology studies in dynamic turbid media [26], and pore sizes measurement in porous media [27–29], etc.

1.3 Gas monitoring in turbid media

Another important area of absorption spectroscopy is gas concentration monitoring based on the unique narrow-band absorption "fingerprint" of gases. Different types of optical techniques have

been developed, such as differential absorption lidar [30, 31], differential optical absorption spectroscopy [32] and tunable diode laser absorption spectroscopy (TDLAS) [33]. Typical applications include, e.g., atmospheric gas monitoring [34, 35], exhaust gas or gas pollutant monitoring in industry [36, 37], and combustion or plasma diagnostics [38]. In all those techniques or applications, the gas absorption pathlengths are well defined or can be calibrated. Thus the concentration of the gases can be easily deduced according to the Beer-Lambert law. However, there is the case where one is interested in the gases enclosed in turbid media such as human sinuses and food packages, which promoted the invention of the gas in scattering media absorption spectroscopy (GASMAS) technique in 2001 as a variety of the TDLAS technique. The principles of the GASMAS technique are based on the fact that the gas absorption spectrum is substantially narrower than that of the solid- or liquid-phase host materials [39]. Unfortunately, we again come to the situation mentioned above, i.e., the gas absorption pathlength is unknown because of the strong light scattering in the host material. This thus composes the main aim of the thesis work, i.e., fighting with the unknown gas absorption pathlength to measure the absolute gas concentration in turbid media. The first approach is to study light propagation in the turbid medium, and measure the total optical pathlength using e.g., the FMLSI technique and the frequency domain photon migration (FDPM) method. The total pathlength can then be used to estimate the gas absorption pathlength, as shown in Papers **I** and **V**. On the other hand, the combination of pathlength measurement techniques and the GASMAS techniques also provides the new possibility to non-intrusively study the porosity of porous media; see Papers **VI** and **VII**. Another approach is to measure the absorption of a specific gas to determine the concentration of other gases in the gas mixture, by studying the gas absorption line shape which depends upon the concentrations of buffer gases; see Paper **VIII**. This method enables gas concentration monitoring without knowing the absorption pathlength, and provides great possibilities for gas monitoring in turbid media. In Paper **IX**, different approaches for measuring gas concentration in turbid media and possible applications of the GASMAS technique are summarized.

Although the aim of investigating the FMLSI technique is to figure out the gas absorption pathlength, it finally turned out that it is actually a very promising approach to study light propagation in turbid media, as discussed in Sect. 1.2.

1.4 Aims and outline of the thesis

Two general aims of the thesis work can be summarized below:

(i) To retrieve the absolute gas concentration in turbid media;

(ii) To provide a new experimental approach to study light propagation in turbid media.

The thesis is organized as follows:

Chap. 2 is focused on the theoretical aspects of light propagation in turbid media. The photon diffusion equation is retrieved from transport theory based on spheric harmonic and diffusion approximations. The frequently used time-of-flight spectroscopy (TOFS) as well as the FDPM method are discussed in detail.

Chap. 3 introduces the FMLSI technique, which can also be used to study light propagation in turbid media, but utilizing a coherent tunable light source. The theoretical aspects as well as the instrumentation are discussed in detail. Furthermore, the applications towards static and dynamic turbid media are discussed.

Chap. 4 describes the principles of TDLAS, which is the also the basis of the GASMAS technique. The working mechanism of tunable diode lasers is briefly introduced. Finally, a sensitivity enhancement technique – wavelength modulation spectroscopy, is discussed in detail.

Chap. 5 discusses the principles, challenges and applications of the GASMAS technique, including the solutions for absolute gas concentration measurements, and porosity studies in porous turbid media.

Chapter 2

Light Propagation in Turbid Media

Light propagation in turbid media is a very complicated process. Generally, three different phenomena can occur, i.e., absorption, emission (e.g., fluorescence) and scattering. One commonly used modeling approach is the transport theory, which takes the particle nature of light into consideration. In the context of the present thesis work, we focus on the transport theory which only deals with two interactions, namely, absorption and scattering. This chapter will briefly give the theoretical description of the transport theory and its approximation – the photon diffusion equation, as well as the analytical solutions for media with simple geometries. For details of the transport theory and photon diffusion equation, the readers are referred to, e.g., [40–42]. The experimental techniques for studying light propagation in turbid media are also discussed. By fitting different theoretical models to the experimental results, the optical properties – absorption and scattering coefficients – can be retrieved.

2.1 Absorption and scattering in turbid media

When light is irradiated on a turbid sample, it will be absorbed and scattered by the host medium. Absorption is generally described by the absorption coefficient μ_a [cm^{-1}], giving the probability of a photon being absorbed per unit pathlength. Its reciprocal yields the average pathlength before the photon is absorbed. Similarly, the scattering coefficient μ_s [cm^{-1}] describes the probability that the photon is scattered per unit pathlength. The reciprocal, $1/\mu_s$, is referred to as mean free pathlength. However, additional treatment for scattering event is required, since the directions of the photons are changed by scattering. This can be modeled by the

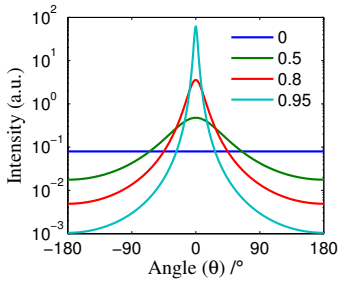

Figure 2.1. Phase function for different anisotropy factors.

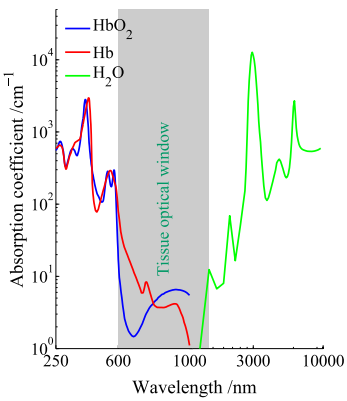

Figure 2.2. Absorption coefficients of water, oxygenated hemoglobin (HbO_2) and deoxygenated hemoglobin (Hb) [44, 45]. The low absorption wavelength region (600-1400 nm) is often referred to as the tissue optical window.

phase function $p(\hat{\mathbf{s}}', \hat{\mathbf{s}})$, indicating the possibility of the photon being scattered from $\hat{\mathbf{s}}'$ to $\hat{\mathbf{s}}$. For large particles with sizes comparable with the optical wavelength or even larger, the scattering in turbid media shows a forward tendency, meaning anisotropic scattering and frequently assumed to be only dependent upon the scattering angle $\theta = \hat{\mathbf{s}}' \cdot \hat{\mathbf{s}}$. The forward tendency can be described by the anisotropy factor g (g-factor):

$$g =< \cos(\theta) >= \int_0^{\pi} p(\hat{\mathbf{s}}', \hat{\mathbf{s}})(\hat{\mathbf{s}}' \cdot \hat{\mathbf{s}}) d\Omega'. \tag{2.1}$$

However, the phase function is almost impossible to retrieve if the material structures are unknown. One frequently used approximate phase function is the Henyey-Greenstein phase function, given by [43]:

$$p(\theta) = \frac{1}{4\pi} \frac{1 - g^2}{(1 + g^2 - 2g\cos\theta)^{3/2}}. \tag{2.2}$$

Figure 2.1 gives the phase function for different g values. One could see that larger g values indicates that the forward scattering is more dominant, with isotropic scattering described by $g = 0$.

Another aspect regarding absorption and scattering coefficients is the wavelength dependency. The absorption spectrum for different materials can vary a lot, as shown in Fig. 2.2. The wavelength dependency of the scattering coefficient generally follows the law of Mie scattering, given by

$$\mu_s(\lambda) = a \left(\frac{\lambda}{\lambda_0} \right)^{-b}. \tag{2.3}$$

Here λ_0 is the reference wavelength. The parameters of a and b must be determined experimentally for individual media depending on the particle sizes and spatial structures.

2.2 Radiative transfer equation

Considering the photon distribution $N(\mathbf{r}, \hat{\mathbf{s}}, t)$ in a small volume V, the net change of photon distribution must obey the energy conservation principle, i.e., be equal to the difference between photon gain and loss, as shown in Fig. 2.3. The variation of the photon density can then be described by the radiative transfer equation (RTE) [46]. Normally, the radiance $L(\mathbf{r}, \hat{\mathbf{s}}, t) = h\nu c N(\mathbf{r}, \hat{\mathbf{s}}, t)$, which is defined as the power per unit area and steradian at the time of t and position $\mathbf{r}$ ($\mathrm{Wm^{-2}sr^{-1}}$), is utilized to formulate the RTE:

$$\frac{1}{c}\frac{\partial L}{\partial t} = \underbrace{q}_{i)} \underbrace{+ \mu_s \int_{4\pi} p(\hat{\mathbf{s}}', \hat{\mathbf{s}}) L d\Omega'}_{ii)} \underbrace{- (\mu_s + \mu_a) L}_{iii)} \underbrace{- \hat{\mathbf{s}} \cdot \nabla L}_{iv)}. \tag{2.4}$$

Here $c = c_0/n_{\text{eff}}$ is the light speed in the medium, c_0 is the light speed in vacuum and n_{eff} is the effective refractive index of the medium. The net change of the radiance originates from different contributions, and is explained as follows:

(i) Radiance gain due to the light source $q(\mathbf{r}, \hat{\mathbf{s}}, t)$ inside the volume;

(ii) Radiance gain due to scattering, i.e., the photons scattered from position $\hat{\mathbf{s}}'$ to position $\hat{\mathbf{s}}$, which is an integration from all possible direction of $\hat{\mathbf{s}}'$;

(iii) The radiance loss due to the absorption and scattering, which is proportional to the absorption (μ_a) and scattering (μ_s) coefficients, i.e., $(\mu_a + \mu_s)cL$;

(iv) Another type of loss is due to photons crossing the volume boundary, i.e., $\oint_S cL\hat{\mathbf{s}}\hat{\mathbf{n}}dS = -\int_V c\nabla L \cdot \hat{\mathbf{s}}dV$. The volume integration is disregarded in Eq. (2.4).

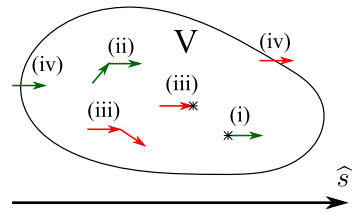

Figure 2.3. Energy conservation principle of radiative transport theory in a volume V; the direction of light propagation is given by $\hat{\mathbf{s}}$. The energy gain due to (i) light source in the volume and (ii) scattering from other positions, the energy loss due to (iii) scattering and absorption, and (iv) the energy gain and loss when photons enter or exit the boundary.

The RTE is hard to solve. One widely used method to provide numerical solutions is Monte-Carlo simulations. By launching enormous numbers of photons and tracking them individually with predefined absorption and scattering coefficients, the fluence rate or photon density at each location is obtained [47, 48]. Thus, Monte-Carlo simulation is a statistic method and time consuming, and the accuracy significantly relies on the launched photon numbers. In recent years, the computation time has been greatly reduced up to an order of 10^3 by using graphics processing units (GPU) [49, 50]. With the effort of many different methods to reduce the computation time, Monte-Carlo methods become more and more popular for simulating light propagation in turbid media [51–54].

In the next section, approximations are made and the diffusion equation can be obtained, from which analytical solutions are also deduced for several simple geometries.

2.3 Photon diffusion equation

The RTE can be reduced to a system of coupled equations by expanding the angular-dependent radiance and light source into an infinite series of spherical harmonics. By truncating the harmonics at N^{th} order, the RTE is reduced to $N+1$ coupled equations, and the corresponding approximation is referred to as P_N approximation [55]. Normally, only low-order spherical harmonics are used, e.g., the P_1 and P_3 approximation [56–58]. Higher order approximation can give higher accuracy, but with an increased complexity. Recent work has also shown that the simplified P_N (SP_N) approximation can significantly reduce the complexity [59, 60]. In the present thesis work, the P_1 (i.e., $N = 1$) approximation is made

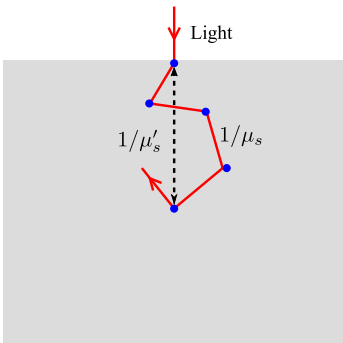

Figure 2.4. The relationship between scattering coefficient and reduced scattering coefficient.

followed by diffusion approximation, resulting in a so-called diffusion equation. The diffusion equation is a very general equation, which has been widely used to describe different physical problems in different fields, e.g., heat transfer, hydrodynamics, and nuclear physics. We thus hereby refer to the diffusion equation obtained for light propagation in turbid media as the photon diffusion equation.

The P_1-approximations of the radiance and light source are given by:

$$L(\mathbf{r},\hat{\mathbf{s}},t) = \frac{1}{4\pi}\Phi(\mathbf{r},t) + \frac{3}{4\pi}\mathbf{F}(\mathbf{r},t)\cdot\hat{\mathbf{s}}, \tag{2.5}$$

$$q(\mathbf{r},\hat{\mathbf{s}},t) = \frac{1}{4\pi}q_0(\mathbf{r},t) + \frac{3}{4\pi}\mathbf{q}_1(\mathbf{r},t)\cdot\hat{\mathbf{s}}. \tag{2.6}$$

Here $\Phi(\mathbf{r},t)$ is the fluence rate [W/m^2], given by the integration of radiance over all $\hat{\mathbf{s}}$, and $\mathbf{F}(\mathbf{r},t)$ is the flux [W/m^2] which is a vector quantity describing the net photon flux. However, the above approximations are only valid when the scattering dominates over the absorption, i.e., $\mu_\mathrm{s} >> \mu_\mathrm{a}$ and the detector is far from the source [41, 61]. Substituting the above equations into the RTE equation, one can get two separate coupled equations

$$\left(\frac{1}{c}\frac{\partial}{\partial t} + \mu_\mathrm{a}\right)\Phi(\mathbf{r},t) + \nabla\cdot\mathbf{F}(\mathbf{r},t) = q_0, \tag{2.7}$$

$$\left[\frac{1}{c}\frac{\partial}{\partial t} + \mu_\mathrm{a} + (1-g)\mu_\mathrm{s}\right]\mathbf{F}(\mathbf{r},t) + \frac{1}{3}\nabla\cdot\Phi(\mathbf{r},t) = -\mathbf{q}_1. \tag{2.8}$$

Equation (2.7) is obtained by integration over all $\hat{\mathbf{s}}$, and Eq. (2.8) is obtained by multiplying $\hat{\mathbf{s}}$ before integration. From Eq. (2.8), one could see that the anisotropy factor and the scattering coefficient are combined together, and only their product, i.e., the reduced scattering coefficient $\mu_\mathrm{s}' = (1-g)\mu_\mathrm{s}$ is possible to retrieve. The reciprocal $l^* = 1/\mu_\mathrm{s}'$ gives the distance needed for the light to become totally randomized, and is often referred to as transport mean free path, as shown in Fig. 2.4. The diffusion equation can be derived based on the following two assumptions:

(i) The light source is isotropic, i.e., $\mathbf{q}_1 = 0$. The collimated source can always be considered as an isotropic source at the depth of one transport mean free path, as discussed below. The isotropic condition can be satisfied if the detector is far from the boundaries and source [62], i.e., to detect light in the diffusive region.

(ii) The temporal change of the flux is negligible over the distance of $1/\mu_\mathrm{s}'$, i.e., $\partial\mathbf{F}/\partial t = 0$. This requires that the light pulse duration should be longer than $1/\mu_\mathrm{s}'c$. For the sinusoidally intensity-modulated light source, the modulation frequency (ω) must satisfy $\omega \ll \mu_\mathrm{s}'c$.

Equation (2.8) can then be rewritten as Fick's law:

$$\mathbf{F}(\mathbf{r},t) = -D\nabla\Phi(\mathbf{r},t). \tag{2.9}$$

Here D is defined as the diffusion coefficient, given by

$$D = 1/\left[3(\mu_s' + \mu_a)\right]. \tag{2.10}$$

Some arguments suggest that the diffusion coefficient is independent of absorption, i.e., $\widetilde{D} = 1/(3\mu_s')$ [63, 64]. However, large discrepancies for the diffusion coefficient between different definitions only occur for large absorption coefficient. Thus, this is not significant in diffusion theory, since it is not valid any more in this case. The diffusion coefficient $\widetilde{D}$ is actually more frequently used in Monte-Carlo simulation, which can give much more accurate results even if the absorption is substantially large [65]. Substituting Eq. (2.9) into Eq. (2.7), the photon diffusion equation for homogeneous media is obtained:

$$\frac{1}{c}\frac{\partial\Phi(\mathbf{r},t)}{\partial t} - D\nabla^2\Phi(\mathbf{r},t) + \mu_a\Phi(\mathbf{r},t) = q_0(\mathbf{r},t). \tag{2.11}$$

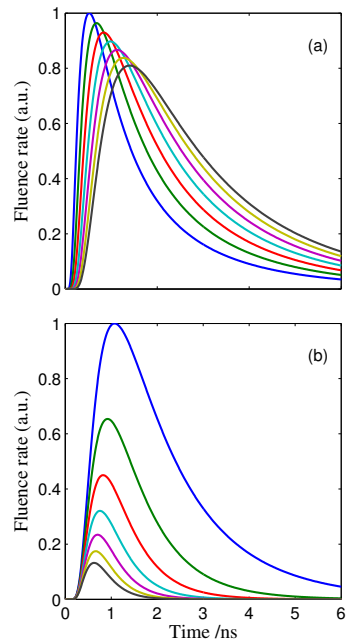

Figure 2.5. The impulse response for different optical properties. (a) $\mu_a = 0.01$ cm^{-1}, $\mu_s' = 6, 8, ...18$ cm^{-1}; (b) $\mu_s' = 15$ cm^{-1}, $\mu_a = 0.02, 0.04, ...0.14$ cm^{-1}.

2.4 Time and frequency domain solutions

Although the RTE has been greatly simplified when transformed into the photon diffusion equation, it is still difficult to solve analytically for media with complicated geometries. The numerical finite element method (FEM) can render solutions to the photon diffusion equation. The FEM method discretizes geometrically large volumes into small volume elements, leading to a linear equation system, since the fluence rate in a small volume can be considered linear. The linear equation is then solved for each element, and the solutions can be obtained in principle for any arbitrary geometry. However, the FEM method has high demands on computer memory, which might cause computational problems. Notably, the RTE equation, in principle, could also be solved by the FEM method [66]. Here, we briefly introduce the analytical solutions of the photon diffusion equation for several simple geometries in the time and frequency domains, which have been extensively used in this thesis work. For a detail discussion regarding the solutions, we refer to [57, 67, 68].

2.4.1 Infinite medium

Considering an isotropic light pulse with unit intensity $q_0 = \delta(\mathbf{r}{=}\mathbf{0})\delta(t)$, the impulse response for an infinite medium can be simply given by the Green's function:

$$\Phi(\mathbf{r},t) = \frac{c}{(4\pi Dct)^{3/2}}\exp\left(-\frac{r^2}{4Dct} - \mu_a ct\right). \tag{2.12}$$

Figure 2.5 shows the time-dependent fluence rate at a certain source-detector separation for different optical properties. Obviously, the changes of the absorption and scattering coefficients result in quite different behaviors of the time-of-flight (TOF) distribution. This enables the separation of μ_a and μ_s' by analyzing the time-dependent fluence rate. However, they are also very sensitive for measurement errors due to their relatively strong correlations [69–71]. Thus, good signal-to-noise ratio (SNR) is required to obtain accurate results.

From the time-dependent fluence rate or TOF distribution, the mean time-of-flight (MTOF) τ_{MTOF} can be deduced from the weighted average:

$$\tau_{\mathrm{MTOF}} = \int_0^\infty \Phi(\mathbf{r},t)t dt \Big/ \int_0^\infty \Phi(\mathbf{r},t)dt, \tag{2.13}$$

and the mean optical pathlength (MOPL) is then simply given by $L_m = c\tau_{\mathrm{MTOF}}$, which can be used for concentration measurements of absorbing substances or chromophores in human tissue [72], and gas enclosed in turbid media [73].

2.4.2 Semi-infinite and slab-shaped media

In the case of a semi-infinite medium, the light source illuminates as a small spot on the surface of the sample. This can be treated as an isotropic light source at the depth of $z_0 = 1/\mu_s'$, where the photons have completely lost their initial directions. Another challenge for a semi-infinite medium is the boundary, where internal reflection can occur and there is no diffusive light coming back once they are emitted from the scattering media. One commonly used method to treat the boundary condition is to add a negative mirror source outside the scattering medium, as illustrated in Fig. 2.6(a) [74]. An extrapolated boundary at the position of z_e is introduced in order to compensate for different refractive indices of the medium and the outside air. With this approach, the fluence rate at the extrapolated boundary becomes zero, and the loss due to the real boundary in the semi-infinite medium is then considered by the negative source. The position of the extrapolated boundary can be analytically given by $z_e = 2AD$, where A can be approximated by

$$A = \frac{2/(1-R_0) - 1 + |\cos\theta_c|^3}{1 - |\cos\theta_c|^2}, \tag{2.14a}$$

$$R_0 = \left(\frac{n-n_0}{n+n_0}\right)^2, \tag{2.14b}$$

$$\theta_c = \arcsin\left(\frac{n_0}{n}\right). \tag{2.14c}$$

Here n and n_0 are the effective refractive indices of the turbid medium and air, respectively. The impulse response at an arbitrary position within the medium can then be described as the sum of the contributions from the positive and negative light sources:

$$\Phi_{\mathrm{R}}(\mathbf{r},t) = \frac{c}{(4\pi Dct)^{3/2}}\exp(-\mu_{\mathrm{a}}ct) \times\left[\exp\left(-\frac{r_+^2}{4Dct}\right)-\exp\left(-\frac{r_-^2}{4Dct}\right)\right], \tag{2.15}$$

where

$$\begin{cases} r_+ = \sqrt{\rho^2+(z-z_0)^2}, \\ r_- = \sqrt{\rho^2+(z+z_0+2z_{\mathrm{e}})^2}. \end{cases} \tag{2.16}$$

For a slab-shaped medium with a thickness of s, extrapolated boundaries are introduced on both sides of the samples, i.e., at the positions $-z_{\mathrm{e}}$ and $s+z_{\mathrm{e}}$, by introducing negative mirror sources at $z_{-,0}$ and $z_{-,1}$, respectively. However, these two mirror sources will result in a violence of the boundaries condition when they are placed simultaneously. Thus, instead of a single negative mirror source, an infinite numbers of positive and negative mirror sources are introduced, as shown in Fig. 2.6(b) [75]. Similarly, the impulse response is the sum of the contributions from all sources. The transmitted light intensity, which has been studied for polystyrene foams and Intralipid® samples in Papers **II** and **III**, is given by [57]

$$\Phi_{\mathrm{T}}(\mathbf{r},t) = \frac{c}{2}(4\pi D)^{-3/2}(ct)^{-5/2}\exp\left(-\frac{\rho^2}{4Dct}-\mu_{\mathrm{a}}ct\right) \times\sum_{m=-\infty}^{+\infty}\left[z_{+,m}\exp\left(-\frac{z_{+,m}^2}{4Dct}\right)-z_{-,m}\exp\left(-\frac{z_{-,m}^2}{4Dct}\right)\right], \tag{2.17}$$

where

$$\begin{cases} z_{+,m} = s(1-2m)-4mz_{\mathrm{e}}-z_0, \\ z_{-,m} = s(1-2m)-(4m-2)z_{\mathrm{e}}+z_0. \end{cases} \tag{2.18}$$

2.4.3 Frequency domain solutions

The frequency domain solutions are the response when the turbid medium is irradiated by a sinusoidally intensity-modulated continuous-wave light [76]. The meaning of "frequency domain" originates from the fact that a pulse light source can always be decomposed into an infinite number of sinusoidally intensity-modulated light waves. The light intensity with modulation frequency f and amplitude A_{m} can be described by

$$q_0'(\mathbf{r},t) = \delta(\mathbf{r}=0)[1+A_{\mathrm{m}}\exp(i2\pi ft)]. \tag{2.19}$$

For a linear system, the response for any input is the convolution of the impulse response and the input function. Thus, the response

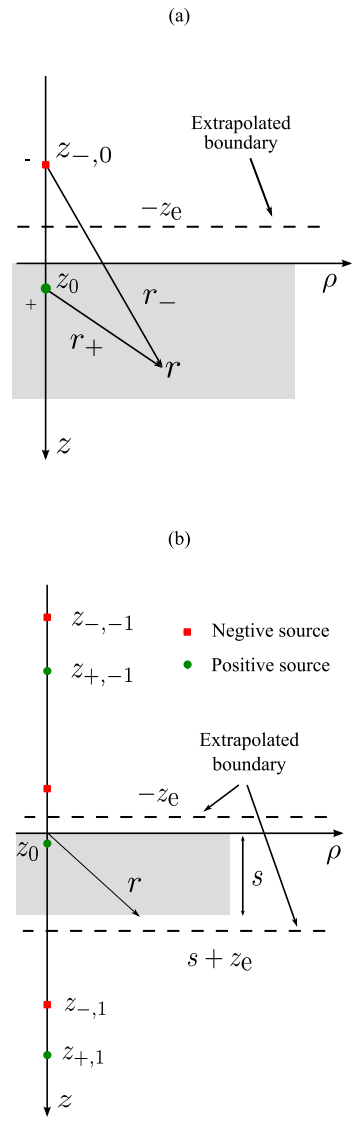

Figure 2.6. Extrapolated boundaries and mirror sources for (a) semi-infinite and (b) slab-shaped media.

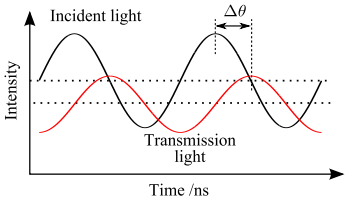

Figure 2.7. Principle of the FDPM technique. The light source is sinusoidally intensity-modulated. Due to scattering and absorption, the transmitted light intensity is phase shifted, and the modulation depth is also reduced.

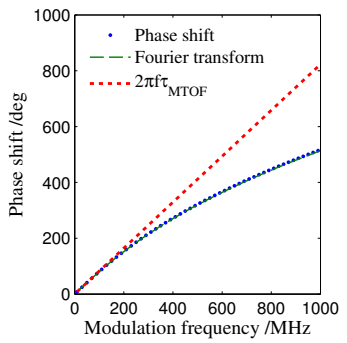

Figure 2.8. Simulated phase shifts at different modulation frequencies. The optical properties are $\mu_s' = 30\ \mathrm{cm}^{-1}$, $\mu_a = 0.05\ \mathrm{cm}^{-1}$, and the refractive index is 1.4.

for an sinusoidally intensity-modulated light is the convolution between the Green's function and the light source radiance $q_0'(\mathbf{r},t)$:

$$\begin{aligned}\Phi(\mathbf{r},f,t) =& \frac{1}{\sqrt{2\pi}}\int_{-\infty}^{\infty} q_0'(\mathbf{r},t-t')\Phi(\mathbf{r},t')dt' \\ =& \frac{1}{\sqrt{2\pi}}\int_{-\infty}^{\infty}\Phi(\mathbf{r},t')dt' \\ &+ \frac{A_m\exp(i2\pi ft)}{\sqrt{2\pi}}\int_{-\infty}^{\infty}\Phi(\mathbf{r},t')\exp(-i2\pi ft')dt'.\end{aligned} \tag{2.20}$$

Equation (2.20) shows that the response for the intensity modulated light is a Fourier transform of the impulse response in the time domain. By measuring the phase shift and the reduced modulation depth, one can retrieve the optical properties of the turbid medium. Such a method is then referred to as the frequency domain photon migration (FDPM) technique. For the transmission measurement on the medium with slab geometry, the solution in the frequency domain $\Phi_T(\mathbf{r},f,t)$ is given by:

$$\begin{aligned}\Phi_T(\mathbf{r},f,t) =& \frac{\exp(i2\pi ft)}{(2\pi)^{3/2}}\sum_{m=-\infty}^{+\infty}\left[\frac{z_{+,m}^2}{r_{+,m}^2}(1+\alpha r_{+,m})\exp(-\alpha r_{+,m})\right. \\ &\left. - \frac{z_{-,m}^2}{r_{-,m}^2}(1+\alpha r_{-,m})\exp(-\alpha r_{-,m})\right].\end{aligned} \tag{2.21}$$

Here

$$\begin{cases} r_{\pm,m} = \sqrt{\rho^2 + z_{\pm,m}^2}, \\ \alpha = \sqrt{(\mu_a c + i2\pi f)/cD}. \end{cases} \tag{2.22}$$

The direct-current (DC) signal is neglected in Eq. (2.21), since it can always be obtained by simply setting $f = 0$. For relatively low modulation frequencies, the phase shift is approximated by [72]

$$\phi = 2\pi f \tau_{\mathrm{MTOF}}. \tag{2.23}$$

Equation (2.23) has been utilized for MOPL assessment in Papers **V**, **VI** and **VII**. The validation of the above equation depends upon optical properties and sample thickness. In general, equation (2.23) holds if $f\tau_{\mathrm{MTOF}} \ll 1$; however, it is not a necessary condition. Simulation results are given in Fig. 2.8. Clearly, the phase shifts obtained from Eq. (2.21) and the Fourier transform of Eq. (2.17) are in good agreement. As can be seen, equation (2.23) gives a very good approximation in the low frequency region, while the discrepancy increases substantially as the modulation frequency increases.

2.5 Time-of-flight spectroscopy

Originating from absorption and scattering, photons emitted at the position of the light source will arrive at the detector with different traveling times, i.e., experiencing different flight times. The TOF distribution, equivalent to the time dependent fluence rate, can be measured by photon time-of-flight spectroscopy (TOFS), as shown in Fig. 2.5. By modeling a measured time-of-flight distribution with e.g., diffusion theory, the optical properties can easily be deduced.

The TOFS technique was first demonstrated by Shimizu *et al.* in 1979 for studying backscattering of picosecond light pulse in aqueous solutions with latex micro-spheres as scattering particles [77]. In the early stage of TOFS, light propagation in turbid media was mainly modeled by diffusion theory [78–80], and Monte-Carlo simulation was introduced later [81–83]. In 1988, Chance *et al.* utilized the TOFS technique to study the oxygenation process of hemoglobin [84, 85], and Delpy *et al.* measured the optical pathlength of tissue phantoms for absorption calibration [81]. Since then, the applications of TOFS have been extensively explored especially in biomedical applications [86–90].

The main idea of TOFS is quite straight forward, as shown in Fig. 2.9(a). Briefly, a very short light pulse (typically in the picosecond range) is delivered to the turbid medium studied, the time dispersion of this pulse is then examined by a highly sensitive detector and fast electronics. The values of μ_a and μ_s' are retrieved by performing non-linear fitting on the TOF distribution based on, e.g., diffusion theory or Monte-Carlo simulation.

Figure 2.9 shows a typical schematic of a TOFS system. A frequently used light source is a high-repetition rate picosecond (e.g., 2 ps) mode-locked Titanium Sapphire (Ti:Sapphire) laser.[1] Its tuning range is, however, limited, e.g., from 760-840 nm [91, 92]. Recently, broadband tunable laser sources (500-1850 nm) based on the non-linear optical processes in a photonic crystal fiber [93] were also employed in TOFS system, enabling full absorption and scattering spectral studies for turbid media in the near infrared region [15, 94, 95]. The detectors used are normally the extremely sensitive photon multiplier tube (PMT) or avalanche photo diode (APD), which are capable to detect single photons.

Apart from the complicated light sources and the sensitive detectors, one significant challenge in the TOFS systems is to detect the ns-scale time dispersion, which is beyond the detection limit of normal electronics. Fortunately, this can be fulfilled through the time-correlated single photon counting (TCSPC) technique, as shown in Fig. 2.9(b). The main idea of the TCSPC technique

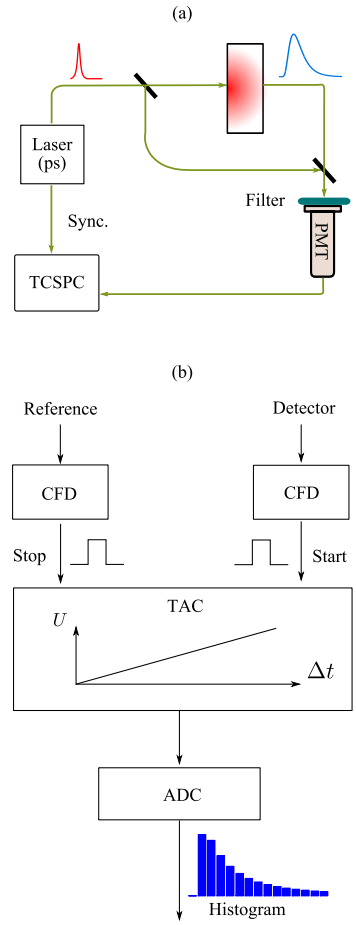

Figure 2.9. (a) System schematic of a TOFS system; (b) the schematic of the TCSPC technique. The input reference and detected signals are first converted to digital pulses by the constant fraction discriminators (CFD), and the time difference between the two digital pulses is converted to a voltage by a time-to-amplitude converter (TAC), followed by an analog-digital converter (ADC).

[1] Femtosecond (fs) light pulse can be readily obtained from a mode-locked Ti:Sapphire laser.

is to detect the time delay of individual photons with respect to the reference pulse. A histogram of the photon distribution for many TOF events is built up, beneficial from the high repetition frequency (typically 80 MHz) of the pulsed laser source. Most importantly, only the first photon for each period is detected, with later photons ignored. The TCSPC must therefore work on the condition of extremely weak light – one can only observe at most one photon per injected light pulse. Otherwise, one will not consider all photons and photon pile up will occur, resulting in measurement errors. The details of the TCSPC technique can be found in [96, 97]. The TOFS system used in Paper **II** is based on the TCSPC technique. Alternatively, streak cameras can also be used for ns-scale pulse detection, where the photoelectrons are deflected into a spatial distribution by applying a rapidly modulated electric field [98].

2.6 Frequency domain photon migration

The frequency domain photon migration (FDPM) technique, sometimes also referred to as diffuse photon density wave (DPDW), originates from the phase shift method utilized for fluorescence lifetime measurement in atomic physics [99–101]. It was for the first time demonstrated by Lakowicz and Berndt to study photon migration in tissues in 1989 [102], and was soon followed by Chance *et al.* to study hemoglobin deoxygenation [103].

The FDPM technique utilizes an intensity-modulated (typically in the 100 MHz range) continuous wave light source and measures the phase shifted light intensity through a scattering medium. Thus, it can avoid using short light pulses and thus sophisticated detection schemes employed in the TOFS system. By evaluating the phase shift and modulation depth variation, the optical properties can be retrieved. The MOPL can either be directly deduced from Eq. (2.23), or modeled once the optical properties are known. Tunable diode lasers, which are capable to be intensity-modulated directly through injection current, are perfect light sources for this application. The transmitted light signal is detected by a PMT or an APD, and then the phase difference with respect to the reference modulation signal can be measured. Figure 2.10(a) shows a typical system schematic of the FDPM technique, where the phase shift and amplitude are measured by a homodyne detection scheme. Due to the compact diode lasers and the well-developed radio frequency (RF) electronics, the FDPM system is much more robust and cheap compared with the TOFS technique. These great advantages push the FDPM technique forward to numerous *in vivo* biomedical applications, such as optical properties studies of tissues [104–106], hemoglobin oxygenation studies [87, 107], breast tumor diagnosis [108–111], and biomedical tomography and imag-

ing [90, 112–119]. Hand-held devices are also possible for FDPM systems, and normally multi-wavelength detections are employed [120, 121].

The most challenging issue for a FDPM system is to accurately detect the phase shift and amplitude originating only from the absorption and scattering of the turbid medium, but eliminating the effect due to the instrument. Chance *et al.* have given a detailed description of the phase measurements in a review article [122]. In the following sections, we will briefly introduce the phase/amplitude detection schemes, and discuss the phase shift introduced by the detectors in detail.

2.6.1 Phase detection schemes

The frequently used phase/amplitude detection schemes are of the following three types:

(a) Homodyne detection
Figure 2.10(a) gives a typical homodyne-detection system. The phase difference can be easily measured by the in-phase and quadrature (IQ) demodulator. The amplitude and phase shift are simultaneously obtained from the in-phase output I_{dc} and quadrature output Q_{dc} [123, 124]. The homodyne detection system becomes quite compact by employing commercial IQ demodulators. The drawback is that the phase error increases as the modulation frequency increases [122]. However, by employing a digital IQ-demodulator, the phase error can be reduced. For instance, Roblyer *et al.* reported a homodyne detection system based on an integrated digital chip (ADC12D1800, National Semiconductor), with a sampling frequency of 3.6 GHz [125].

(b) Heterodyne detection
The heterodyne-detection scheme greatly reduces the phase measurement errors by converting the high frequency down to the audio frequency range, i.e., 1-100 kHz [126], as shown in Fig. 2.10(b). The phase difference of the low frequency signals can then be easily measured by an IQ demodulator or a zero-cross phase detector. The drawback is that two phase-coherent RF sources are needed.

(c) Single sideband detection
The single sideband (SSB)-detection scheme utilizes one RF source and one audio frequency source, and a sum/difference frequency signal is generated to modulate the light source [127]. The detected RF signal is then converted down to the audio frequency signal again by utilizing a signal mixer. Thus, the phase difference can also be measured at low frequency.

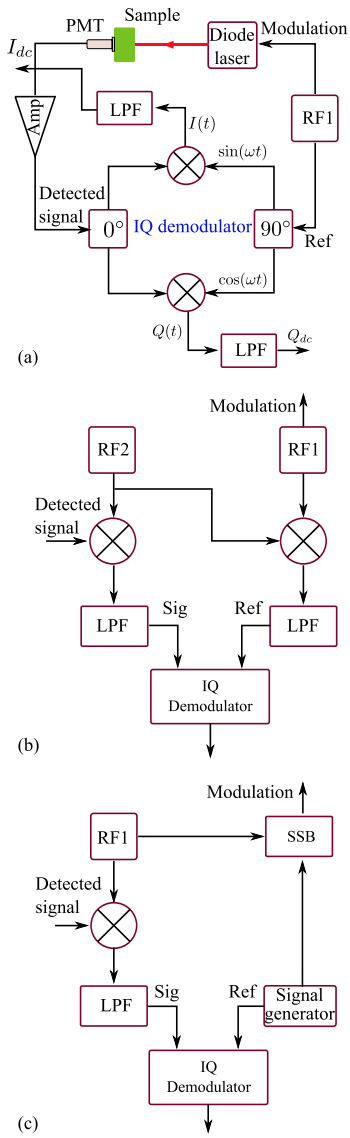

Figure 2.10. (a) Homodyne, (b) heterodyne and (c) single sideband (SSB) detection schemes for the FDPM technique. Amp – amplifier, LPF – low pass filter, IQ – in-phase and quadrature.

The optical properties can be extracted according to diffusion theory from the measured values of phase shift and amplitude. However, sometimes, the optical properties are obtained by measuring the phase shifts at several different modulation frequencies. In Paper **V**, the homodyne-detection scheme was built up by using a digital oscilloscope with a high sampling frequency, while in Paper **VII**, a heterodyne-detection scheme was employed. In both applications, the phases were measured by digital IQ demodulators.

2.6.2 Amplitude-phase crosstalk

Since the instrument itself, e.g., amplifier and detector, also introduces a phase shift and affects the amplitude, a very careful calibration procedure is required to retrieve the absolute phase/amplitude. However, the phase shift introduced by optical detectors depends on many factors, e.g., the uniformity of the detector surface, PMT voltages, and light intensities, which increase the difficulties of phase calibration. Different PMT voltages will produce different electric fields. Thus the transit times[2] changes with PMT voltage. High PMT voltage will greatly increase the speed of the electrons, which thus reduce the time spent in the PMT and introduce a smaller phase shift. To avoid phase errors induced by different PMT voltages, it is important to keep PMT voltage constant when calibrating the phase shift.

The intensity-dependent phase shift, often referred to as amplitude-phase crosstalk, is the main challenge for the phase calibration. One need to keep the same light intensities when measuring the sample and the system response. Otherwise, phase error would be introduced. In the present thesis work, only PMTs are used for FDPM measurements, we will thus explain the originations of the phase shift introduced by PMTs. However, to be noted, APD also has the amplitude-phase crosstalk effect [128].

The amplitude-phase crosstalk actually has already been observed when the phase shift method was utilized to measure the lifetime of fluorescence [129]. It also attracted much attention in FDPM systems [128, 130, 131]. The amplitude-phase crosstalk mainly originates from the transit time spread (TTS), which is primarily due to the different trajectories of photoelectrons. Photoelectrons generated at different positions of the cathode can definitely experience different trajectories, and thus increase TTS. This is often referred to as cathode transit time difference (CTTD). However, even if the photoelectrons come from the same position of the cathode, they can still have different trajectories because of

[2]The transit time is the time interval between the arrival of the photon at the cathode and the arrival of the pulse at the anode.

different ejection angle from the cathode and from the subsequent dynodes.

Generally, the TTS is inversely proportional to the square root of the photoelectron number, or the light intensity (See Fig. 4-20 in Ref. [132]). The PMT rise/fall time,[3] which directly depend on the TTS, will thus increase as the input average light intensity decreases. Thus, lower light intensity will result in a larger phase delay, as has been observed in Paper **VII**. To be noted, the CTTD is not intensity dependent but rather illumination pattern dependent. This will contribute to a phase error especially when the illumination patterns are different between the measurements on the instrument response and the samples.[4] The non-uniformity of the cathode surface, resulting in different response on the different positions of the cathode surface, could also contribute to the phase errors. The phase errors induced by nonuniform surface or CTTD are often not considered in FDPM system, since the illumination areas are generally quite small, typically a few millimeter. This is especially true when using a proximity-focused[5] microchannel plate PMT (MCP-PMT). However, one should note that sometimes it could be a problem, as has been observed in Paper **V**. Muller *et al.* have observed different phase shifts for different illumination areas [129] as early as 1965.

It is worth mentioning that the space charge effect could increase the TTS as the light intensity increases. The underlying mechanism of the space charge effect is that the photoelectrons will generate an opposite electric field with respect to that in the PMT when the photoelectrons form a cluster at the last few dynode stages. This will slow down the speed of the electrons which come up later. However, the space charge effect occurs when the number of photoelectrons substantially increases, and it mainly affects the anode linearity.[6]

According to the criteria proposed by Chance *et al.* (3% measurement accuracy), the amplitude-phase crosstalk should be less than 0.03° at modulation frequencies of 50-200 MHz when the light intensity is attenuated by a factor of 10 dB [122]. In practice, many FDPM systems exhibit larger amplitude-phase crosstalk. Thus, real-time phase calibration is normally necessary for many applications.

[3] Rise time: the time of the anode signal rises from 10% to 90% of its final level. Correspondingly, fall time is the time that the anode signal falls from 90% to 10% of its peak pulse height.

[4] However, it can be reduced by using special geometrical designs.

[5] The distance between the photocathode and the MCP is approximately 2 mm.

[6] For details, see the PMT handbook from Hamamatsu [132].

Chapter 3

Frequency Modulated Light Scattering Interferometry

3.1 Introduction

In this chapter, we will discuss a new technique, i.e., frequency modulated light scattering interferometry (FMLSI) which studies light propagation in turbid media by using a coherent tunable continuous-wave diode laser. The FMLSI technique can actually be dated back to the 1920s, when the concept of frequency modulated continuous wave (FMCW) was first introduced by Appleton and Barnett to find out the evidence of the existence of the ionosphere [133]. Since the 1940s, FMCW radio detection and ranging (radar) was more and more extensively used for ranging systems, especially in military applications [134]. As given in Fig. 3.1, by transmitting a frequency-modulated RF signal, the change in frequency of the echo signal from the remote target experiences a delay. The time delay of the change of frequency can be detected by using a heterodyne-detection scheme with a reference signal from the same RF source [135]. Thus, a beat signal is produced, the frequency of which is linearly proportional to the distance R (or light traveling time) between the base station and the remote target. The distance R can be evaluated as

$$R = \frac{c \cdot f_{\mathrm{b}}}{2 \cdot d\nu/dt}. \tag{3.1}$$

Here c is the speed of the electro-magnetic wave or light, f_{b} is the frequency difference or the so-called beat frequency, and $d\nu/dt$ is the change of frequency per unit time which can be given by $\Delta\nu/T_{\mathrm{m}}$ for a sawtooth modulation. Here $\Delta\nu$ is the frequency modulation range, and T_{m} is the modulation period. Instead of a sawtooth modulation, other modulation patterns can also be used

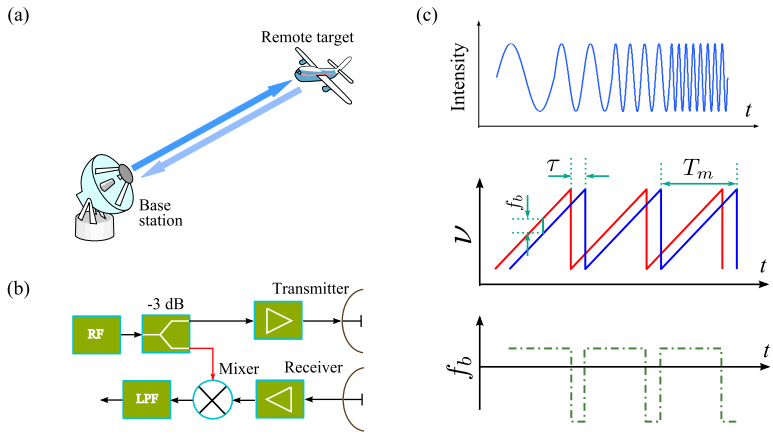

Figure 3.1. (a) Application of FMCW radar, (b) system schematics of FMCW radar, LPF - low-pass filter (c) Transmitted signal, the delay (τ) of the change of frequency between the echo and the reference signals, and the diagram of the corresponding frequency difference (f_b). The period of the change in frequency is T_m.

for different applications, e.g., triangular and sinusoidal modulations [136]. The great advantage of the FMCW technique is that a high spatial resolution can be achieved although with a much simpler architecture compared with the traditional pulsed radar technique, which makes it more attractive for civil use. Actually, the FMCW radar has always been a very hot research topic, and widely used during recent decades in e.g., mapping/imaging radar [137–139], snow depth detection [140, 141], and local positioning [142–144].

When applying the FMCW technique to an optical interferometer, there are two critical prerequisites. First, the optical frequency of the light source must be continuously tunable. Second, the coherence length must be sufficiently long to make the FMCW technique applicable, i.e., a narrow linewidth is needed. The application of an optical FMCW interferometer was difficult until a coherent narrow-band semiconductor tunable diode laser was introduced in the early 1980s [145, 146]. Figure 3.2(a) shows a typical optical FMCW interferometer, where the distance between the Michelson interferometer to the target can be precisely measured by analyzing the frequency of the beat signal. Since then, the optical FMCW interferometer has been widely used for positioning or ranging systems [147–151], velocity measurements [152, 153], distributed strain or stress sensors [154–156] and gas sensing [157–159]. Especially in the telecommunication field, the FMCW interferometer has become one of the standard methods

for fiber fault detection, which is often referred to as optical frequency domain reflectometry (OFDR) [160, 161]. In contrast, the fiber fault detector using a pulsed light source is named as optical time domain reflectometer (OTDR).

Actually, there is another type of "frequency-domain" fiber fault detector, utilizing light as a carrier wave. The light intensity is modulated by a RF signal with linearly increased frequency. This technique is referred to as frequency domain optical reflector (FDOR) [162], which, however, cannot be considered as an optical FMCW interferometer since the beat signal is generated not from the light waves but from the RF signals. However, FDOR is a good complementary approach when the coherent tunable light source is not readily available.

In the above discussions, the FMCW technique is traditionally used to detect a single or a few single reflections from the target objects. The details of the relevant theories and applications of the FMCW technique are covered in the book written by J. Zheng [163]. However, in principle, it can also be used to detect an infinite number of reflection signals. In 2009, the optical FMCW interferometer was introduced to the broad field of optical diffusing spectroscopy for light propagation assessment through scattering media [164]. As given in Fig. 3.2(b), there is now an infinite number of "echoes" or "fiber faults" due to heavy light scattering, instead of a single delay or a finite number of delays. Since then, the FMLSI technique has been thoroughly studied and utilized for light propagation assessment both in static and dynamic turbid media by employing a linear frequency modulation; see Papers **I** to **IV**. In the latter work (Papers **III** and **IV**) the applications of the optical FMCW interferometer in turbid media were referred to as FMLSI to specify the special application field.

Actually, sinusoidal modulation of optical frequency can also be used in FMCW interferometers for light propagation studies, as has been demonstrated by Tualle *et al.* since 2001 [165–169]; however, without any connections to the optical FMCW interferometer. In the present thesis, we would also take the sinusoidal modulation scheme as a part of the FMLSI family, although special consideration must be taken in practice. In order to clearly describe the principles of the FMLSI technique, we will first introduce the basic mathematics for the optical FMCW interferometer and then extend the theory to scattering media. In the following sections, we would also give a very brief introduction to the FMLSI technique employing sinusoidal frequency modulation, and the differences between the linear and sinusoidal frequency modulation schemes are also discussed.

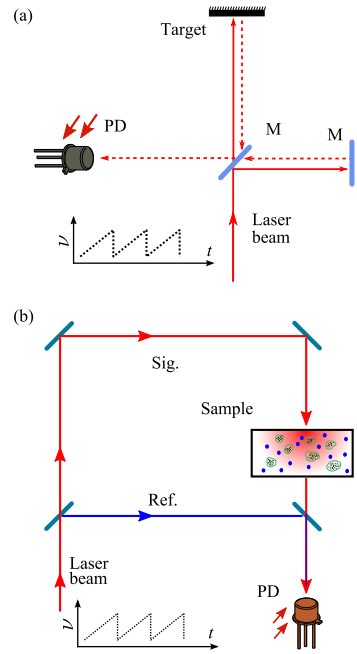

Figure 3.2. (a) Optical FMCW interferometer with Michelson [150] interferometer, (b) schematic of the FMLSI technique employing a Mach-Zehnder interferometer. The pathlength of the reference arm is normally shorter in the FMLSI system, in order to give an increased beat frequency when the pathlength of the signal arm increases due to scattering.

3.2 Principles

As shown in Fig. 3.2(b), a Mach-Zehnder interferometer is normally employed for heterodyne detection in scattering media. The light waves through the signal and reference arms undergo different pathlength, thus experiencing different propagation time. When the two light waves arrive at the detector, there would be a delay for the change of frequency between these two light waves. Thus, a beat signal would be generated. We will first consider the case without scattering medium.

3.2.1 Frequency modulated continuous wave interferometer

Linear frequency modulation

If we define $f_{\mathrm{m}} = 1/T_{\mathrm{m}}$ as the optical frequency modulation rate, ν_0 as the optical center frequency and $\Delta\nu$ as the optical modulation range, the optical frequency of the light wave is given by

$$\nu(t) = \nu_0 + \beta t. \tag{3.2}$$

Here, $\beta = f_{\mathrm{m}}\Delta\nu$ is the modulation coefficient. The phase of the emitted light wave is then given as

$$\begin{aligned}\theta(t) =& \int 2\pi\nu(t)dt \\ =& \int 2\pi\left(\nu_0 + \beta t\right)dt \\ =& 2\pi\left(\frac{1}{2}\beta t^2 + \nu_0 t\right) + \theta_0.\end{aligned} \tag{3.3}$$

Here, θ_0 is the initial phase. The optical waves through the reference and signal arms can be expressed as

$$E_{\mathrm{ref}}(t) = A_{\mathrm{ref}}\cos\left[2\pi\left(\frac{1}{2}\beta t^2 + \nu_0 t\right) + \theta_{\mathrm{ref}}\right], \tag{3.4}$$

$$E_{\mathrm{sig}}(t) = A_{\mathrm{sig}}\cos\left[2\pi\left(\frac{1}{2}\beta(t-\tau)^2 + \nu_0(t-\tau)\right) + \theta_{\mathrm{sig}}\right]. \tag{3.5}$$

Here τ is the time difference between the signal and the reference light waves. The intensity of the beat signal is then given by

$$\begin{aligned}I(t) =& \left\langle\left[E_{\mathrm{ref}}(t) + E_{\mathrm{sig}}(t)\right]\left[E^*_{\mathrm{ref}}(t) + E^*_{\mathrm{sig}}(t)\right]\right\rangle \\ =& \underbrace{\frac{1}{2}\left(A^2_{\mathrm{sig}} + A^2_{\mathrm{ref}}\right)}_{I_{\mathrm{DC}}} \\ &+ A_{\mathrm{ref}}A_{\mathrm{sig}}\cos\left[2\pi\left(\beta\tau t - \frac{1}{2}\beta\tau^2 + \nu_0\tau\right) - \theta_{\mathrm{sig}} + \theta_{\mathrm{ref}}\right].\end{aligned} \tag{3.6}$$

Since τ is much smaller than t, the term $\frac{1}{2}\beta\tau^2$ can be neglected.[1] If we denote

$$\theta_{\text{diff}} = 2\pi\nu_0\tau - \theta_{\text{sig}} + \theta_{\text{ref}}, \tag{3.7}$$

Equation (3.6) can be rewritten as

$$I(t) = I_{\text{DC}} + A_{\text{ref}}A_{\text{sig}}\cos\left(2\pi\beta\tau t + \theta_{\text{diff}}\right). \tag{3.8}$$

From the above equation, the beat frequency is found to be $f_{\text{b}} = \beta\tau$. By measuring the beat frequency, the optical pathlength difference (OPD) or the time delay (τ) between the reference and signal paths can be retrieved. Since the minimum detectable frequency of the beat signal is equal to the modulation rate f_{m},[2] the time resolution is given by $\tau_{\text{min}} = f_{\text{m}}/\beta = 1/\Delta\nu$.[3] This indicates that the modulation range should be as large as possible in order to achieve a high time resolution.

Sinusoidal frequency modulation

When employing sinusoidal frequency modulation, the center frequency is given by

$$\nu(t) = \nu_0 + \frac{1}{2}\Delta\nu\cos(2\pi f_{\text{m}}t), \tag{3.9}$$

and the phase of the light wave can be written as

$$\theta(t) = 2\pi\left[\nu_0 t + \frac{\Delta\nu}{4\pi f_{\text{m}}}\sin(2\pi f_{\text{m}}t)\right] + \theta_0. \tag{3.10}$$

Following the same procedure given above, the intensity of the beat signal is given as

$$I(t) = I_{DC} + A_{\text{ref}}A_{\text{sig}}\cos\left[\pi\Delta\nu\tau\cos\left(2\pi f_{\text{m}}t\right) + \theta_{\text{diff}}\right]. \tag{3.11}$$

If the beat signal is multiplied by the following reference signal

$$Ref(t,\tau') = \sin^{2n}(2\pi f_{\text{m}}t)\exp\left[\pi\Delta\nu\tau'\cos(2\pi f_{\text{m}}t)\right], \tag{3.12}$$

the average value over a half period would be linearly proportional to the power at the corresponding time delay [165]:

$$S_{\text{DC}}(t,\tau') = \int_0^{T_{\text{m}}/2} I(t)Ref(t,\tau')dt. \tag{3.13}$$

In Eq. (3.12), the value of n can be 1,2,3..., and the term $\sin^{2n}(2\pi f_m t)$ represents a window function. Such a mathematical manipulation is actually equivalent to the Fourier transform

[1] Considering $\Delta\nu = 100$ GHz, $f_{\text{m}} = 100$ Hz, optical pathlength difference of 1 m (3.3 ns), we obtained $2\pi\cdot\frac{1}{2}\beta\tau^2 = 3.5\times10^{-4}$ rad.

[2] In practice, it could be slightly larger.

[3] 100 GHz modulation range corresponds to a time resolution of 10 ps.

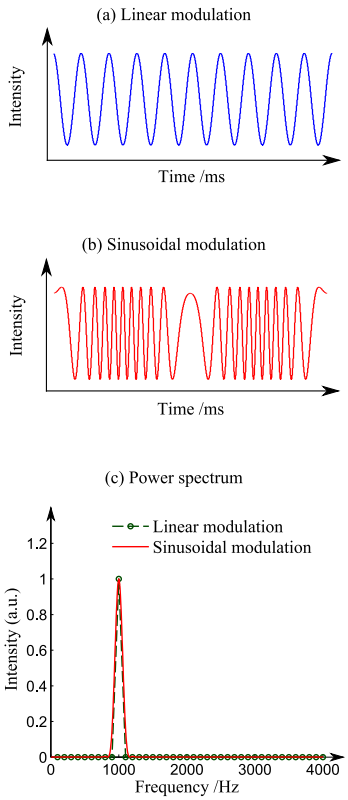

Figure 3.3. (a) and (b) simulated beat signals for the linear and sinusoidal frequency modulation, (c) the corresponding power spectra for the beat signals. However, we should note that the power spectrum for the sinusoidal frequency modulation is not obtained directly from the Fourier transform of the beat signal, but from Eqs. (3.12) and (3.13), which can be considered equivalent to the Fourier transform. Simulation parameters: $f_{\mathrm{m}} = 100$ Hz, $\Delta\nu = 50$ GHz, $\tau = 200$ ps.

performed on the beat signal for linear frequency modulation. Figure 3.3 shows the simulated beat signals for the linear and sinusoidal frequency modulations; the corresponding power spectra are also presented. Clearly, for linear frequency modulation, the power spectrum gives the location of the beat frequency, corresponding to the time delay. However, the Fourier transform of the beat signal for the sinusoidal modulation does not give any useful information since the beat frequency is not a constant value as can be seen from Eq. (3.11). Instead, the spectrum obtained through Eqs. (3.12) and (3.13) gives an equivalent power spectrum for the sinusoidal frequency modulation, as shown in Fig. 3.3(c).

Coherence consideration

Obviously, an *a priori* assumption for the optical FMCW interferometer is that an optical light waves with different frequencies could interfere. However, a question might be raised that how the FMCW interferometer could work at all, since the frequency difference (e.g., kHz range) between the reference and signal light waves is much smaller than the bandwidth of the diode laser (e.g., 10 MHz). In practice, this is actually also the case for the laser Doppler velocimeter, and sometimes very broadband lasers are employed.

Let us first consider an interferometer without frequency modulation. The light source has a certain bandwidth and consists of a series of incoherent components with different optical frequencies. Each incoherent component can only persistently interfere with itself, but not with other components with different frequencies. Thus, a larger bandwidth of the light source results in a lower-contrast interference pattern. This has been well-known in coherence theory. When modulating the center frequency of the light source, the incoherent components of the optical light waves for each center frequency do not change, and most importantly they are modulated in the same manner. Thus, each incoherent component can still interfere, although the interference contrast would be decreased due to the non-infinitely-narrow bandwidth [170].

3.2.2 Optical interferometer with scattered light

For a scattering medium, the signal light wave will be scattered and become diffuse. Instead of a single time delay, there are now an infinite number of delays. We hereby make the assumption that, for each TOF, the light can travel along different paths through the scattering medium. Thus for each possible path the light will experience a different phase shift, depending upon the TOF and the scattering events. In other words, diffused light waves can have different wavefronts although they arrive at the detector at the

same time. We must note here that the phase shift is not related to the light propagation time but due to phase changes during scattering events, although mathematically they can be related to each other.

Let us consider a discretized number (M) of TOFs, i.e., τ_i ($i = 1, 2, ..., M$), and there are N_i different paths (components) for each τ_i. The amplitude for each path is denoted as $A_{\text{sig}}^{i,j}$ and $\theta_{\text{sig}}^{i,j}$ ($j = 1, 2, ..., N_i$) is the corresponding phase term. Thus, for a certain TOF (τ_i), the signal wave can be written as

$$E_{\text{sig}}^{i}(t) = \sum_{j=1}^{N_i} A_{\text{sig}}^{i,j} \cos\left[2\pi\left(\frac{1}{2}\beta(t+\tau_i)^2 + \nu_0(t+\tau_i)\right) + \theta_{\text{sig}}^{i,j}\right]. \tag{3.14}$$

Similar to Eq. (3.7), the heterodyne-detected beat signal is then given as

$$I_i(t) = I_{\text{DC}}^{i} + A_{\text{ref}} \sum_{j=1}^{N_i} A_{\text{sig}}^{i,j} \cos\left(2\pi\beta\tau_i t + \theta_{\text{diff}}^{i,j}\right). \tag{3.15}$$

Here the interferences between the signal wave components are neglected by assuming that the reference wave is much stronger than each of the signal wave components, which can be easily fulfilled since the signal waves are generally attenuated millions of times due to heavy light scattering. Since there is a pathlength difference between the reference and signal paths in the interferometer itself, as shown in Fig. 3.2(b), the time offset τ_0 should also be considered. Equation (3.15) is then further simplified (see Appendix A) and can be given by

$$I_i(t) = I_{\text{DC}}^{i} + A_{\text{ref}} C_{\text{sig}}^{i} \cos\left[2\pi\beta\left(\tau_i + \tau_0\right)t + \theta_{\text{diff}}^{i}\right], \tag{3.16a}$$

$$C_{\text{sig}}^{i\ 2} = \sum_{j=1}^{N_i} A_{\text{sig}}^{i,j\,2} + \sum_{j=1}^{N_i}\sum_{k\neq j}^{N_i} A_{\text{sig}}^{i,j} A_{\text{sig}}^{i,k} \cos\left(\theta_{\text{diff}}^{i,j} - \theta_{\text{diff}}^{i,k}\right), \tag{3.16b}$$

$$\theta_{\text{diff}}^{i} = \arctan\frac{\sum_{j=1}^{N_i} A_{\text{sig}}^{i,j} \sin\left(\theta_{\text{diff}}^{i,j}\right)}{\sum_{j=1}^{N_i} A_{\text{sig}}^{i,j} \cos\left(\theta_{\text{diff}}^{i,j}\right)}. \tag{3.16c}$$

Equation (3.16b) is actually very similar to the laser Doppler velocimetry (LDV) equation as given in [171]. Actually, the laser Doppler technique and the FMLSI technique utilize the same principles, i.e., the interference signals are generated from optical waves with different frequencies. From the second term in Eq. (3.16b), we note that the amplitude of the beat signal depends upon the phase differences due to the different traveling paths. Obviously, the amplitude of the beat signal would also vary at different positions of the detector, which is referred to as speckles, similar to the situation in the LDV case [172]. However, the speckle patterns

vary in time due to the movement of the scattering particles in LDV, which is not the case for static turbid media. By neglecting the DC component and the amplitude of the reference arm, the power spectrum of the beat signal measured through a static scattering medium is given by

$$|\mathcal{F}[I(t)]|^2 = \sum_i^M {C_{\text{sig}}^i}^2 \delta[f - \beta(\tau_i + \tau_0)]. \tag{3.17}$$

As is well-known, TOFS measures the light intensity for each TOF, resulting in a TOF distribution, which can be given by $\sum {A_{\text{sig}}^{i,j}}^2$, since the interference terms vanish due to the broadband light source. Clearly, it is independent from the phase differences. Equation (3.17) actually gives the TOF distribution of light propagation through the turbid medium, if the ensemble average of the second term in Eq. (3.16b) is very small or even equal to zero.

For the static turbid media, linear or sinusoidal frequency modulation can give similar results [165]. However, different "Fourier transform" must be performed, as has been discussed above.

3.3 Instrumentation

3.3.1 Measurement system

In the early work of the present thesis, a free space FMLSI system was employed. The advantage of a free space system is that much more scattered light can be collected; however, with the disadvantage of less flexibility of measurement geometry – only transmission geometry measurements can be readily performed. Thus, a fiber based system is highly demanded to explore different applications.

A typical systematic diagram of a fiber based FMLSI system is given in Fig. 3.4. A narrow-band tunable DFB diode laser with a linewidth of 2 MHz is used as the light source. The frequency/wavelength of the diode laser is modulated with a triangle waveform at a repetition frequency of, e.g., 400 Hz. The time resolution can be improved by increasing the modulation range. However, a larger modulation range will reduce the SNR. One should also note that the frequency response of the diode laser is not flat – the faster the modulation, the smaller the optical frequency modulation coefficient. In order to minimize the mode dispersion, which is a very critical problem not only for the FMLSI technique but also for other techniques mentioned in Chap. 2, graded index multimode fibers are used to deliver the illumination light and collect the scattered light. A beam splitter (92:8) is utilized to build up the interferometer, and the interference signal is detected by an avalanche photo diode (APD). The detected photocurrent is fed into a trans-impendence amplifier with a bandpass filter, and then sampled by a data acquisition (DAQ) card and transferred to

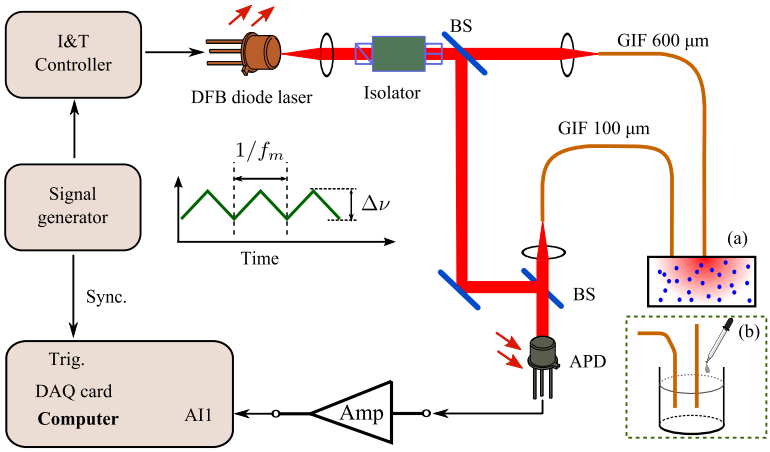

Figure 3.4. Schematic of the fiber based FMLSI system, (a) reflectance measurement for static turbid medium, (b) dynamic turbid medium measured in infinite geometry. DFB – distributed feedback, BS – beam splitter, APD – avalanche photo diode, Amp – amplifier.

computer for data analysis. Obviously, the FMLSI system is much more compact compared with the TOFS and FDPM techniques.

One should always keep in mind that the FMLSI is born to measure fringes, thinking about the weak backscattering light from fiber faults. As has been pointed out by Tualle *et al.*, "*there is a forest of parasitic signals of various origins*" [166]. It is very important to reduce the reflectance of various optical components, since the scattered light is extremely weak. An optical isolator is used to eliminate the effect of the backscattering light from, e.g., the fiber connector, as shown in Fig. 3.4. On the other hand, the free space light beam is used as a reference arm to construct the interferometer which would have less fringes. In practice, the free space FMLSI system exhibits much weaker fringes due to much weaker back reflections from optics. This is actually another advantage of using a free space FMLSI system. In spite of the fringes problem and the reduced SNR, the fiber based FMLSI system gives the possibilities to measure turbid media in different context or geometries.

Another issue of the FMLSI technique is to measure the frequency offset ($\beta\tau_0$) originating from the pathlength difference between the reference and the signal arms of the interferometer. The value of $\beta\tau_0$ can be obtained by sending the light through a neutral density filter or paper, before collecting by the multimode fiber. Notably, the thickness of the sample must be considered when measuring samples in transmission geometry. The value of $\beta\tau_0$ is quite stable, as long as the temperature of the diode laser is stabilized

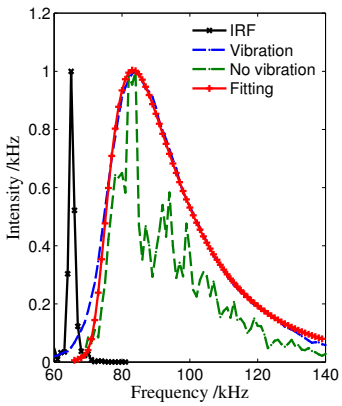

Figure 3.5. Power spectrum of a 12-mm polystyrene foam, measured in transmission geometry. The reduced scattering coefficient and absorption coefficient were found to be 34 cm^{-1} and -0.01 cm^{-1}, respectively. Both the power spectra measured without any vibration and with vibration on the collecting fiber are recorded. The power spectrum with out any vibration shows significant "spikes". If a narrow band picosecond pulsed light source exist, we would expect a TOF distribution with many spikes because of interference.

by the thermoelectric cooler (TEC). On the contrary, substantial effort must be devoted to stabilize the TOFS system.

3.3.2 Signal processing

Considering that the light intensity fluctuation $I(t)$ of the beat signal is sampled by a window function $W_N(t)$ during a time period of T'_{m}, the power spectrum of the beat signal is given by

$$P(f) = \left|\mathcal{F}\left[I(t)W_N(t)\right]\right|^2 \tag{3.18}$$

Because of non-integral data sampling, an inherent problem when performing discrete Fourier transform (DFT) is the frequency leakage, i.e., the energy from one frequency is leaked out to their neighbouring frequencies. This effect will cause measurement errors, and can only be reduced by applying different window functions, e.g., a Hamming window, or a Hanning window. When performing the nonlinear fitting to the measured power spectrum, the instrument response should also be considered. If the power spectrum for a non-scattering medium, e.g., neutral density filter or paper, is denoted by $H(f)$, referred to as instrument response function (IRF), the nonlinear fitting can follow the equation

$$P(f) = \int \Phi(\mathbf{r}, f')H(f - f')df', \tag{3.19}$$

where $\Phi(\mathbf{r}, f)$ is the fluence rate $\Phi(\mathbf{r}, t)$ when the time t is substituted by the beat frequency ($f = \beta t$).

Figure 3.5 shows a typical power spectrum measured through a 10-mm polystyrene foam with transmission geometry, corresponding to the TOF distribution. However, the x-axis is now frequency, which is linearly proportional to the TOF. We also note that there are many "spikes", mainly originating from the speckle patterns, which are not negligible for the static scattering medium studied. Apart from that, the frequency leakage can also contribute to the spikes of the power spectrum, as has been discussed in Paper **II**. Although the power spectrum presents many "spikes", it can still give a very good approximation for the MTOF, as has been demonstrated in Papers **I** and **II**. On the other hand, the "spikes" can actually be eliminated if one can randomly change the phase term and thus the ensemble average of the second term in Eq. (3.16b) is approximately zero. As given in Fig. 3.5, a smooth power spectrum was obtained by randomly vibrating the collection fiber and performing ensemble averaging. The reduced scattering coefficient and absorption coefficient are also available by performing nonlinear fitting based on the diffusion theory according to Eq. (3.19) (see Paper **IV**).

3.4 Dynamic turbid media studies

In previous sections, we have discussed in detail the theory and application of the FMLSI technique in static turbid media. When applying the FMLSI technique to dynamic turbid media, one must consider the movement of the scattering particles, since the Doppler effect also induces beat signals with different beat frequencies related to the movement of the particles. In the present thesis, we mainly focus on the scattering particles undergoing random walk movement – Brownian motion. Particles which move with certain velocity and direction, e.g., blood cell movement, are not treated here. Before going into the details of the applications of the FMLSI technique in dynamic turbid media, we will first discuss the theory of other similar techniques, the concept of which has been utilized in the FMLSI technique. These technique has already been widely used to examine Brownian motion, or more generally, movements of various scattering particles.

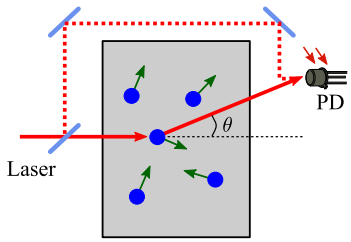

Figure 3.6. Examination of Brownian motion using the DLS technique, based on heterodyne-detection scheme.

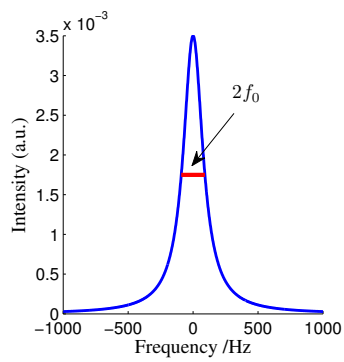

Figure 3.7. Power spectrum of the heterodyne-detected light intensity for the particles undergoing Brownian motion. Simulation parameters: $\lambda = 632$ nm, $\theta = 60°$, $T = 298$ K, $\eta = 8.9 \times 10^{-4}$ Pa·s, $a = 150$ nm. The effective refractive index is 1.33, and the theoretical linewidth is $f_0 = 90.9$ Hz.

3.4.1 Brownian motion

Brownian motion was first observed in 1827 by the botanist Robert Brown in pollen grains in water. It is defined as the random motion of particles suspended in a fluid resulting from the collision with atoms or molecules. Brownian motion was later theoretically explained by Albert Einstein in 1905 and verified by Jean Perrin in 1908. The mean squared displacement in three dimensions for a Brownian particle is given by

$$\overline{x^2} = 6D_{\mathrm{B}}t. \tag{3.20}$$

Here D_{B} is the diffusion constant given by

$$D_{\mathrm{B}} = \frac{k_{\mathrm{B}}T}{3\pi\eta a}, \tag{3.21}$$

where T and η are the temperature and viscosity of the fluid, respectively; k_{B} is the Boltzmann constant and a is the particle diameter. One simple optical method to examine the Brownian motion is the dynamic light scattering (DLS) technique [26], which measures the intensity fluctuation due to single scattering based on a heterodyne or homodyne detection scheme, as given in Fig. 3.6. Due to the movement of the Brownian particle, a Doppler shift is produced for the light scattered by the particle. Thus, beat signals would be generated when the scattered light waves with different frequency shifts arrive at the detector. The power spectrum of the light signal obtained in a heterodyne detection scheme is given by Lorentzian function (see Appendix B)

$$S(f) = \frac{1}{\pi f_0}\frac{1}{1+(f/f_0)^2}. \tag{3.22}$$

Here f_0 is the linewidth of the power spectrum, given by $f_0 = q^2 D_B/2\pi$, where $q = 2k\sin(\theta/2)$ is the scattering vector and k is the optical wave vector. A typical power spectrum is given in Fig. 3.7. From the power spectrum or the more frequently used autocorrelation function, the dynamics and structure of the turbid medium could be studied. In general, the Doppler shift is much smaller than the optical frequency. Thus, DLS is also often referred to as quasi-elastic light scattering (QELS). The DLS technique has been widely used for e.g., particle sizing [173, 174], rheology processes [175, 176] and biomedical applications [20].

3.4.2 Diffusing wave spectroscopy

As we have pointed out above, the DLS technique can only examine light that is singly scattered, which limits its applications. For a highly turbid medium where the light has been scattered a significant number of times before arriving at the detector, the original direction of the light is totally lost and the frequency shift is accumulated along the scattering paths. In the late 1980s, the diffusing wave spectroscopy (DWS) was introduced to study turbid media with multiple scattering [177–180], which is also well-known as diffuse correlation spectroscopy in biomedical field [181]. The electric field amplitude autocorrelation function for the detected light intensity is then given by

$$G^{(1)}(\tau) \propto \int_0^\infty \rho(s) \exp\left([-2(\tau/\tau_0')(s/l^*)]\right) ds. \tag{3.23}$$

Here $\tau_0' = 1/(D_B k^2)$ is the characteristic diffusion time, $\rho(s)$ is the photon density function for the pathlength s, and l^* is the transport mean free path which is equal to $1/\mu_s'$. As noted from Eq. (3.23), the autocorrelation of the detected light intensity considers all possible pathlengths through the turbid medium. Obviously, *a priori* knowledge to fully employ the DWS technique is to figure out the photon density function $\rho(s)$, corresponding to the TOF distribution discussed in previous chapters. Thus, a pre-condition for DWS techniques is that $s >> l^*$, and the value of l^* must be determined independently [182]. By studying the decay of the autocorrelation function, one can extract valuable information on the dynamics and structure of the turbid media [21, 183–185].

In many applications, the power spectrum instead of the autocorrelation function is used. However, it is the integration of the power spectra for all possible pathlengths. Thus, the power spectrum for each pathlength s is actually not available through the DWS technique. Instead, by employing the low coherent interferometry (LCI) [186, 187], the power spectrum for all possible pathlengths can be resolved [188–190] since only the photons with a certain pathlength can be examined due to the low coherence of

the light source. The LCI technique is often referred to as optical coherent tomography (OCT) in the biomedical field [191].

The power spectrum for the scattered light with a pathlength s can also be given by Eq. (3.22). However, the linewidth depends upon the times that the photons have been scattered. We now denote the power spectrum as $S(t, f)$, where $t = s/c$ and c is the speed of light in the medium. The linewidth of the power spectrum is given by

$$f_0 = \frac{k^2}{\pi} D_{\mathrm{B}}(ct)/l^*. \tag{3.24}$$

To be noted, the TOF distribution or the photon density function could also be constructed by integrating the power spectrum for each possible pathlength measured by the LCI technique, but with relatively low SNR [190].

3.4.3 Time delay and Doppler shift

As the light is scattered by the moving particles, it does not only change the propagation direction but also experiences a frequency shift. Thus, when using the FMLSI technique to measure dynamic turbid media, e.g., a colloidal suspension such as Intralipid, the light waves in the signal arm would experience both Doppler frequency shifts and time delays compared with the light traveling in the reference arm. Both of the two effects will contribute to the beat signal. Thus, the power spectrum of the light intensity is the combined effect of the light scattering and the Brownian motion. The power spectrum measured by the FMLSI technique can be interpreted as the accumulation of the power spectrum for each possible pathlength:

$$P(f) = \int_0^\infty S\left(t, f - (t + \tau_0)\beta\right) \rho(t) dt. \tag{3.25}$$

Compared with the DWS technique, the main advantage of the FMLSI technique is that the power spectrum for each pathlength is integrated with a frequency shift linear proportional to the corresponding pathlength. Thus, the light scattering information is retained in the FMLSI technique, which is not the case for the DWS technique. Theoretical simulations for the power spectrum are given in Fig. 3.8. As can be seen, the power spectrum exhibits similar variation behaviors with the TOF distribution shown in Figure 2.5. The applications of the FMLSI technique in tissue phantom studies are discussed in detail in Papers **III** and **IV**.

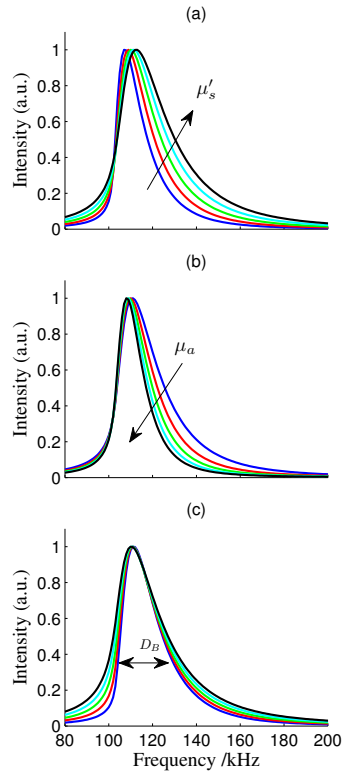

Figure 3.8. Power spectra of the transmitted light intensity through dynamic turbid media. Simulation parameters: (a) $\mu_{\mathrm{s}}' = 10, 12, 14, 16, 18$ cm^{-1}, $\mu_{\mathrm{a}} = 0.05$ cm^{-1}, $D_{\mathrm{B}} = 4 \times 10^{-12}$ m^2/s; (b) $\mu_{\mathrm{s}}' = 15$ cm^{-1}, $\mu_{\mathrm{a}} = 0.05, 0.15, 0.25, 0.35, 0.45$ cm^{-1}, $D_{\mathrm{B}} = 4 \times 10^{-12}$ m^2/s; (c) $\mu_{\mathrm{s}}' = 15$ cm^{-1}, $\mu_{\mathrm{a}} = 0.05$ cm^{-1}, $D_{\mathrm{B}} = 2, 3, 4, 5, 6 \times 10^{-12}$ m^2/s.

3.5 Discussion

The techniques employed in this thesis, which can measure the optical properties of turbid media, are actually connected with

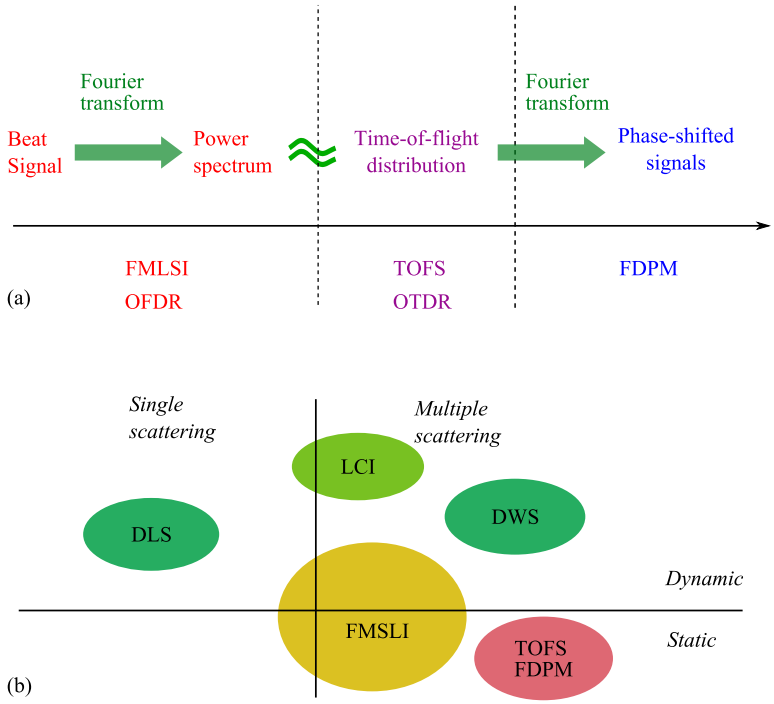

Figure 3.9. Interconnections between different measurement techniques for turbid media. FMLSI – frequency modulated light scattering interferometry, TOFS – TOF spectroscopy, FDPM – frequency domain photon migration, OFDR – optical frequency domain reflectometer, OTDR – optical time domain reflectometry, DLS – dynamic light scattering, LCI – low coherent interferometer, DWS – diffusing wave spectroscopy.

each other through Fourier transforms, as given in Fig. 3.9(a). The FMLSI technique measures the time dispersion as beat frequencies, and the power spectrum of the beat signal is equivalent to the TOF distribution measured by the TOFS technique, while the phase-shifted and demodulated light signals obtained in the FDPM technique is the Fourier transform of the TOF distribution measured by the TOFS technique. In practice, these three techniques used for light propagation studies in scattering media are the most widely used methods in optical or RF ranging system, but just with different names [192].

Another interesting observation is the different nomenclatures for the same techniques in different fields. The fiber fault detector employing the FMCW method, i.e., the OFDR technique, is referred to as the "frequency domain" technique of the OTDR technique in telecommunication field. However, when applying all these techniques for light propagation studies in turbid media, the

phase-shift (FDPM) method is referred to as the "frequency domain" technique of the TOFS technique. Such a connection is dedicated to the transform from time domain to frequency domain, while the connection between the OTDR and the OFDR techniques is from the time domain to "optical" frequency domain.

The power spectrum measured by the FMLSI technique is also related to pathlength-resolved light intensity distribution deduced from the integration of the power spectrum for each pathlength measured by the LCI technique. The FMLSI technique measures the integrated Doppler power spectrum for all possible pathlengths, while the LCI technique measures the power spectrum individually. The pathlength information is retained both in the FMLSI and the LCI techniques, but not for the DWS technique. The DLS technique examines dynamic turbid medium in the single scattering regime, while the LCI technique can measure the Doppler effect from ballistic to diffusive regions because of the low coherence of the light source – "coherence gate". Obviously, the FMLSI technique interconnects the light scattering effect and the Doppler effect, and thus the relevant techniques, as shown in Fig. 3.9(b). If single scattering is dominant, what the FMLSI technique records is actually the same as what is measured by the DLS technique. On the other hand, if the movement is negligible, the power spectrum obtained from the FMLSI technique is equivalent to the TOF distribution. In summary, the FMLSI technique cannot only be used for optical properties assessment, but also for dynamics studies.

Chapter 4

Tunable Diode Laser Absorption Spectroscopy

Each atom or molecule existing in gas phase exhibits a unique spectroscopic fingerprint, enabling high-selectivity measurements using gas absorption spectroscopy. To fully utilize the high selective gas sensing feature, one simple solution is to employ a tunable narrow-band diode laser as the light source and detect the absorption imprint in the light transmitted through the gas. The particularly convenience of using tunable diode lasers is that the laser wavelength/frequency can be easily tuned through the driving current and temperature. The technique of employing tunable diode lasers for trace gas monitoring or spectroscopic studies is referred to as tunable diode laser absorption spectroscopy (TDLAS), which has become a standard analytical tool and is widely used for many applications [33, 193]. The great advantages of the TDLAS technique are high selectivity, immunity to interference from other gases and high sensitivity. Moreover, it can support short response time *in situ* measurements.

The work of the present thesis is definitely founded on the well-developed TDLAS technique. In this chapter, We will discuss the TDLAS technique in detail, and the applications towards scattering media will be the topic of next chapter. In the following sections, we first briefly overview the history of the TDLAS technique, and describe the basic principles and fundamental physics behind. The development history and the working mechanism of the tunable diode lasers are also discussed. Finally, sensitivity enhancement techniques, and in particular the frequently used wavelength modulation spectroscopy, is also discussed in detail.

4.1 Introduction

TDLAS was first demonstrated in 1970 by Hinkley using a lead-salt semiconductor diode laser [194] to study the absorption spectrum of sulfur hexafluoride (SF_6) at 10.6 μm [195]. The mid-infrared[1] continuous wave $Pb_{0.88}Sn_{0.12}Te$ diode laser running at 10.6 μm can achieve a current-tunable range over 50 GHz and a narrow linewidth of 100 kHz, enabling high resolution spectroscopic studies. Since then, the TDLAS technique based on the mid-infrared lead-salt diode laser was further developed by Hinkley and other researchers for many trace gases in the early 1970s [197, 198], e.g., SF_6 [199], methane (CH_4) [200], carbon oxide (CO) [201, 202], sulfur dioxide (SO_2) [203], formaldehyde (HCHO) [204] and water vapor (H_2O) [205]. The mid-infrared TDLAS can provide extremely high detection sensitivity due to high probability for fundamental transitions, which is typically 30 to 300 times[2] stronger than that in the near infrared (or overtone) region below 2 μm [206]. However, the application of lead-salt diode lasers is limited by the requirement of cryogenic cooling,[3] occurrence of mod-hops, low output power and system complexity [207]. Despite of the drawbacks, mid-infrared TDLAS based on lead-salt diode lasers was still widely used for high-resolution and -sensitivity spectroscopy applications in the 1980s and 1990s [208–213]. The compact and robust mid-infrared quantum cascade lasers (QCLs) with much higher power running at room temperature [214, 215], invented in 1994 in the group of Federico Capasso [216], lead to further development and applications of mid-infrared TDLAS in recent years [196, 217, 218].

In the 1980s, near infrared tunable diode lasers, made of III-V semiconductor materials, were also widely used for trace gas monitoring because of their remarkably improved performance as a result of the high demand in optical communications [219–223]. The drawback of the reduced detection sensitivity in the near infrared region is outweighed by the robust and reliable near infrared diode lasers operating at room temperature. This also enables the near infrared TDLAS to be used for *in situ* measurements or industrial applications [224, 225]. Moreover, the detectors used in this region are much cheaper, and no special cooling is needed while lack of cooling would greatly increase the noise in the mid infrared region. On the other hand, further development of sensitivity enhancement techniques, such as wavelength modulation spectroscopy (WMS) [226], frequency modulation spectroscopy [227], Faraday rotation absorption spectroscopy [228], cavity ring-down absorption spectroscopy (CRDS) [229], cavity enhanced absorption spectroscopy (CEAS)[4] [230, 231], and photoacoustic absorption spectroscopy (PAS) [200, 232–234], can significantly increase the detection sensitivity of the TDLAS technique up to ppmv or ppbv level for many species even in the near infrared region [235–239]. The drawback of

[1] Mid-infrared: 2-25 μm [196]; near-infrared: 0.7-2 μm.

[2] Line intensity for NH_3: 5×10^{-19} at 10.3 μm, and 1×10^{-20} at 2 μm; Line intensity for CO_2: 3×10^{-18} at 4.23 μm, 3×4^{-22} at 1.955 μm or even lower at the communication wavelengths.

[3] Cryogenic cooling means extremely low temperature cooling, i.e., below -150°C.

[4] CEAS is also called integrated cavity output spectroscopy (ICOS).

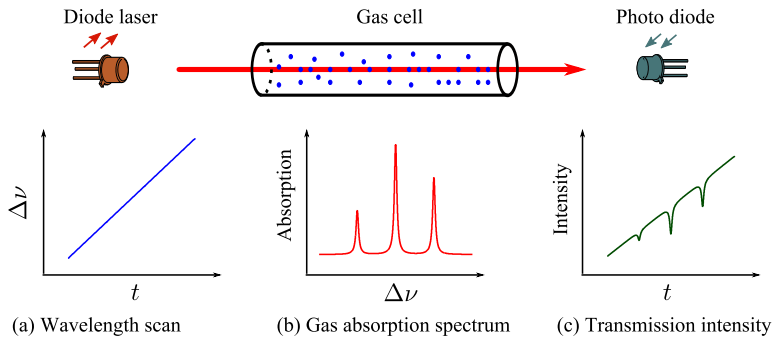

Figure 4.1. Principles of the TDLAS technique. (a) The optical frequency of the laser diode is linearly scanned across the gas absorption line; (b) the absorption spectrum of the gas in the gas cell; (c) the detected light intensity with gas absorption imprints.

low overtone transition probability can thus be compensated and high sensitivity can still be achieved. Unfortunately, many gases do not have any readily available absorption lines (or too weak) in the near infrared region, e.g., HCHO, NO and SF_6. Thus, mid-infrared TDLAS is still a good choice for spectroscopic measurements for many species [240]. On the other hand, for extremely low gas concentration measurement, e.g., human breath gas analysis, mid infrared TDLAS is still preferable to achieve a detection sensitivity of ppbv level for, e.g., NH_3 detection [241].

During recent years, the TDLAS field has developed through the new applications motivated by QCLs [242, 243] and the development of various sensitivity enhancement techniques [244–249], in particular the state-of-art technique – noise-immune cavity-enhanced optical heterodyne molecular spectroscopy (NICS-OHMS) [250, 251]. The applications of the TDLAS technique in, e.g., industrial processing [225], environmental monitoring [34, 252], plasma diagnostics [253], and breath analysis for biomedical applications [254], have also brought up great interest in recent decades.

4.2 Principles

The principles of the TDLAS technique are quite straight forward. As illustrated in Fig. 4.1, a laser beam with intensity $I(\nu)$ passes through a gas cell with a length of L, and the wavelength of the tunable diode laser is linearly scanned across the absorption lines of the target gas by ramping the driving current of the diode laser. The absorption imprint due to the gas of interest can be detected by measuring the transmission light intensity ($I(\nu)$), which is de-

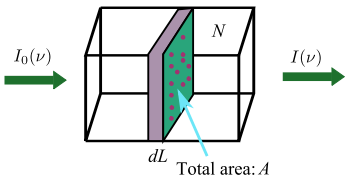

Figure 4.2. Light absorption by a gas. Considering a parallel beam passing through a gas cell with gas concentration of N, the possibility of a photon is absorbed by a single molecule is $\sigma(\nu)/A$. In an infinite thin area A, the number of molecules is given by $N \cdot A \cdot dL$. Thus, the fraction of absorbed light by passing through an infinite short distance is given as $dI(\nu)/I(\nu) = (N \cdot A \cdot dL) \cdot [\sigma(\nu)/A] = \sigma(\nu)NdL$, the integration of which gives the Beer-Lambert law.

scribed by the Beer-Lambert law:

$$I(\nu) = I_0(\nu) \exp\left[-LN\sigma(\nu)\right]. \tag{4.1}$$

In the case of weak absorption, we have

$$I(\nu) \approx I_0(\nu) - I_0(\nu)LN\sigma(\nu). \tag{4.2}$$

Here N is the gas concentration and $\sigma(\nu)$ is the gas absorption cross-section. A simple derivation of the Beer-Lambert law based on absorption cross-section is given in the caption of Fig. 4.2. The value of $\sigma(\nu)$ can be obtained from the standard spectroscopic database or by using a reference measurement with known gas concentration. For a well-defined gas cell with known pathlength L and $\sigma(\nu)$, one can readily retrieve the gas concentration according to the Beer-Lambert law. Larger values of $\sigma(\nu)$ give larger absorption imprints and thus increase the detection sensitivity, as in the case for the mid-infrared gas absorption lines discussed above. Apart from being used for concentration measurement, absorption cross-section also contains many other important information regarding the ambient environment, e.g., temperature, pressure and concentration of buffer species. Thus it plays an extremely important role in gas absorption spectroscopy. We will introduce the basic concept of the absorption cross-section as well as molecular absorption spectra in Sect. 4.3.

Further processing on the detected light signal in Fig. 4.1 is to convert the photocurrent to voltage by the trans-impedance amplifier (TIA). The voltage signal is then digitized for signal processing or directly detected through an analogue lock-in amplifier. The absorption imprint shown in Fig. 4.1 is actually often much weaker, especially when the approximation condition is satisfied. Thus, sensitivity enhancement techniques, such as WMS and CEAS, are frequently employed to detect trace gas concentration up to the ppbv level. Clearly, the basic equipment used in TDLAS techniques are diode lasers, gas cells, detectors and relevant electronics. The simplicity of the system structure enables the possibility to build up a compact and robust TDLAS instrument. We will discuss the details of the tunable diode lasers in Sect. 4.4, and then in Sect. 4.6 give the mathematical description of the WMS technique, which has been extensively used in this thesis. The gas cells, which often employ high reflectivity mirrors to increase the absorption pathlength and thus the sensitivity, would be part of the topic of Sect. 4.5.

4.3 Gas absorption spectroscopy

Considering a two-energy system with energy difference of $\Delta E = h\nu_0$, the transition probability, often described by line strength,

from the lower state to the upper state when absorbing an electromagnetic wave with frequency ν_0 is governed by quantum mechanics. However, the transition does not correspond to a strictly monochromatic spectral line, but rather to a frequency distribution around the center frequency ν_0, due to different broadening mechanism, e.g., the finite lifetime of the molecules on the upper state. For molecules at a certain condition (e.g., room temperature, 1 atm pressure), the absorption cross-section $\sigma(\overline{\lambda} - \overline{\lambda}_0)$ is formulated to describe the possibility of a photon being absorbed over a spectral range, with the unit of $\mathrm{cm}^2\mathrm{molecule}^{-1}$. The absorption cross-section can be described by two terms, i.e., line intensity $S_{\overline{\lambda}_0}$ and line shape function $g(\overline{\lambda} - \overline{\lambda}_0)$:

$$\sigma(\overline{\lambda}) = S_{\overline{\lambda}_0} g(\overline{\lambda} - \overline{\lambda}_0), \tag{4.3}$$

$$S_{\overline{\lambda}_0} = \int \sigma(\overline{\lambda}) d\overline{\lambda}. \tag{4.4}$$

For simplicity, the center wavenumber/frequency of absorption cross-section is neglected. The line intensity,[5] depending upon the transition probability from the lower energy state to an upper energy state and the population of atoms/molecules in the lower state, can be given by [255]

$$S_{\overline{\lambda}_0} = \frac{g_2}{g_1} \frac{A_{21}\lambda_0^2}{8\pi c} \frac{g_1 \exp\left(-hcE''/kT\right)}{Q(T)} \left[1 - \exp(h\nu_0/kT)\right]. \tag{4.5}$$

Here g_2 and g_1 are the degeneracies of the upper and lower energy state, $1/A_{21}$ is the lifetime of the upper energy state, h is the Planck constant, k is the Boltzmann constant, T is the temperature, E'' is the energy of the lower state, $Q(T)$ is the partition function which is the weighted sum of atoms/molecules for all possible energy states. The line intensity defined using optical frequency ν is then given by

$$S_{\nu_0} = \int \sigma(\nu) d\nu = \int \sigma(\overline{\lambda}) d(\overline{\lambda} c) = S_{\overline{\lambda}_0} c. \tag{4.6}$$

In the following discussion, the line shape function is also described as a function of optical frequency ν, i.e., $g(\nu - \nu_0)$. Correspondingly, the absorption cross-section is given as $\sigma(\nu) = S_{\nu_0} g(\nu - \nu_0)$.

[5] Traditionally, the wavenumber $\overline{\lambda} = 1/\lambda = \nu/c$ instead of ν is often used for the line intensity and the absorption cross-section. The unit of the line intensity is $(\mathrm{cm}^2\mathrm{molecule}^{-1})\mathrm{cm}^{-1}$.

4.3.1 Line profiles

The line shape function $g(\nu - \nu_0)$ is determined by three different broadening mechanisms: natural broadening, Doppler broadening, and pressure broadening. Natural broadening is normally much smaller than the other two effects. The pressure broadening is usually dominant over the Doppler broadening in the visible region, and especially important for infrared wavelengths and high pressure conditions.

Natural broadening

Natural broadening is due to the energy uncertainty (ΔE) and determined by the lifetime (τ) of upper state. According to the Heisenberg uncertainty principle

$$\Delta E \cdot \Delta t \geq \hbar, \tag{4.7}$$

The frequency uncertainty is then given as

$$2\Delta\nu = \frac{1}{2\pi\tau}. \tag{4.8}$$

Here $\Delta\nu$ is the half width at half maximum (HWHM) of natural broadening. In the following discussion, "linewidth" is always referred to the HWHM. Since all atoms or molecules radiate with equal possibility, the natural broadening is a homogeneous broadening and follows a Lorentzian line shape which has a linewidth of around 0.1-100 MHz. For instance, a mercury atom at the excited $6s6p\ ^3P_1$ state has a lifetime of 125 ns, and its natural broadening linewidth is 0.6 MHz.

Doppler broadening

Doppler broadening originates from the thermal motion of atoms or molecules, which results in Doppler shifts on the optical frequency. The Doppler broadening is an inhomogeneous broadening, and follows a Gaussian lineshape function:

$$g_{\mathrm{D}}(\nu - \nu_0) = \frac{\sqrt{\ln 2}}{\sqrt{\pi}\alpha_{\mathrm{D}}} \exp\left[-\ln 2 \left(\frac{\Delta\nu}{\alpha_{\mathrm{D}}}\right)^2\right], \tag{4.9a}$$

$$\alpha_{\mathrm{D}} = \frac{\nu_0}{c}\sqrt{\frac{2\ln 2kT}{M}}. \tag{4.9b}$$

Here α_{D} is the Doppler broadening linewidth, and M is the mass of the atom/molecules. For oxygen molecules in atmospheric conditions, a typical Doppler broadening linewidth of oxygen is around 400 MHz at 760 nm, which is much larger than the natural broadening linewidth.

Pressure broadening and line shift

The pressure broadening is due to intermolecular collisions, which shorten the lifetime and thus induce even larger energy uncertainty and a broadening. Aside from that, the intermolecular collision will also shift the energy levels, resulting in a change of center wavelengths. The pressure broadening is also often referred to as collision broadening, the line shape of which is described by the Lorentzian function [256]

$$g_{\mathrm{L}}(\nu - \nu_0) = \frac{\alpha_{\mathrm{L}}/\pi}{(\nu - \nu_0 - \delta_{\mathrm{shift}})^2 + \alpha_{\mathrm{L}}^2}. \tag{4.10}$$

Here α_{L} is the pressure broadening linewidth, and δ_{shift} is the collision-induced optical frequency shift. The intermolecular collision broadening is a very complicated time-dependent many-body problem [257–259], which has been extensively experimentally studied for gases such as H_2O and CO_2. [260–263]. In summary, different molecules will have different collision broadening and line shift coefficients, and the total effect depends upon the gas compositions, which can be approximated by a linear function

$$\alpha_{\mathrm{L}} = \sum_i q_i \gamma_i, \tag{4.11a}$$

$$\delta_{\mathrm{shift}} = \sum_i q_i \delta_i. \tag{4.11b}$$

Here q_i and γ_i are the concentration and broadening coefficient for each composition, respectively, and δ_i is the corresponding line shift coefficient. For atmospheric conditions, Equation (4.11a) can be simplified as

$$\alpha_L = q\gamma_{\mathrm{self}} + (1-q)\gamma_{\mathrm{air}}. \tag{4.12}$$

Here q is the gas concentration, γ_{self} is the self-broadening coefficient, γ_{air} is the broadening coefficient due to air which is mainly O_2 and N_2. A typical pressure broadening linewidth for oxygen absorption lines at 760 nm in atmospheric condition is around 1.5 GHz. Figure 4.3 gives typical Gaussian and Lorentzian line shape functions for a linewidth of 1.5 GHz.

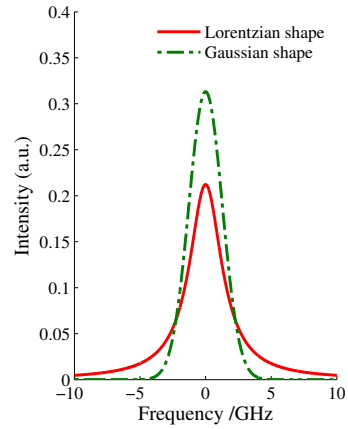

Figure 4.3. Gaussian and Lorentzian line shape functions both with a linewidth of 1.5 GHz. The Lorentzian line shape has broader wings.

Voigt profile

In practice, all these broadening mechanisms occur at the same time but independently. The Doppler and pressure broadenings are much dominant compared with the natural broadening, which is thus not considered for most of the cases. The total effect would be the convolution of the Doppler and pressure broadening line shape, resulting in a Voigt profile, which is given by

$$g_{\mathrm{V}}(\nu-\nu_0) = \sqrt{\frac{\ln 2}{\pi}}\frac{V(u,a)}{\alpha_{\mathrm{D}}}, \tag{4.13a}$$

$$a = \sqrt{\ln 2}\alpha_{\mathrm{L}}/\alpha_{\mathrm{D}}, \tag{4.13b}$$

$$u = \frac{\nu-\nu_0}{\alpha_{\mathrm{D}}/\sqrt{\ln 2}}, \tag{4.13c}$$

$$V(u,a) = \frac{a}{\pi}\int_{-\infty}^{+\infty}\frac{\exp(-t^2)}{(u-t)^2+a^2}dt. \tag{4.13d}$$

For rough estimations, one can directly use the Lorentzian lineshape function to approximate the gas absorption profile, which is valid for the cases in this thesis.

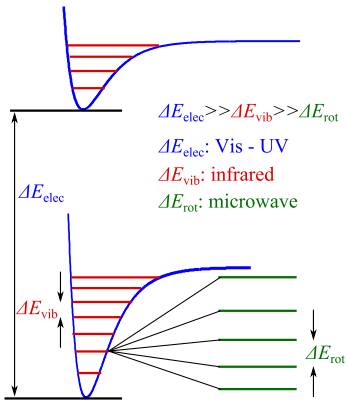

Figure 4.4. Schematic of molecular energy level. The electronic energy could be described by the Morse potential.

4.3.2 Molecular absorption spectra

In this section, we will only give a very simple basis which helps us to understand the molecular absorption spectra. For a detailed description regarding atomic and molecular spectroscopy, the reader is referred to several books, e.g., [258, 264, 265].

Molecular energy level

An atomic energy level can generally be described by a set of quantum numbers (n, l, m_l, m_s) based on quantum mechanics.[6] The energy of atoms is mainly determined by n and l. However, because of the coupling with electron spin, the energy level is split into different fine-structure energy levels, which are further split into hyperfine structure when considering the spin of the nucleus. Molecules, consisting of two or more atoms have much more complicated energy structures. The electrons from all atoms contribute to the electronic energy levels of the molecules. The electronic energy state can be approximated by the Morse potential. Apart from that, the vibration and rotation of the atoms introduce further energy splitting. The corresponding energy levels are referred to as vibrational and rotational energy levels, with much smaller separation than the electronic energy levels, as shown in Fig. 4.4. In summary, the energy levels of molecules can be described by the sum of electronic energy, vibrational energy, and rotational energy:

$$E_{\text{tot}} = E_{\text{elec}} + E_{\text{vib}} + E_{\text{rot}}. \tag{4.14}$$

Different angular moments and the term symbols for electronic states are shown in Fig. 4.5. The vibrational and rotational energy for diatomic molecules can be described by

$$E_{\text{vib}} = h\nu(v + 1/2) - (v + 1/2)^2 x_{\text{e}} h\nu, \tag{4.15a}$$

$$E_{\text{rot}} = BJ_{\text{rot}}(J_{\text{rot}} + 1) - D^+ J_{\text{rot}}^2 (J_{\text{rot}} + 1)^2, \tag{4.15b}$$

$$B = \hbar^2/(\mu_{\text{mass}} r^2). \tag{4.15c}$$

Here v ($v = 0, 1, 2, ...$) and J_{rot} ($J_{\text{rot}} = 0, 1, 2, ...$) are the vibrational and rotational quantum number, respectively, x_{e} is the anharmonicity constant, B is the rotational constant, D^+ is the centrifugal distortion constant, μ_{mass} is the reduced mass, and r is the distance of the atom.

Transition nomenclature

When the molecules transit between different vibrational-rotational energy levels, J''_{rot} (lower energy level) $\longleftrightarrow$ J'_{rot} (upper energy level), if $J'_{\text{rot}} = J''_{\text{rot}} + 1$ the transition is referred to as the

[6] n is the principal quantum number, l is the orbital angular momentum, m_l is the z-component of l, m_s is z-component of the electron spin s.

R-branch spectrum, while $J'_{\rm rot} = J''_{\rm rot} - 1$ corresponds to the P-branch spectrum. If $J'_{\rm rot} = J''_{\rm rot}$, the transitions are the Q-branch spectrum. Considering the effect of the electron motion on the rotational energy level, the total rotational angular momentum is the sum of the pure rotation angular momentum and the electron angular momentum, as shown in Fig. 4.5. The new total rotational angular momentum (J) is given by

$$J = J_{\rm rot} + \Omega. \tag{4.16}$$

The transition for different vibrational-rotational energy levels is then denoted as $\Delta J''_{\rm rot} J'_{\rm rot} \Delta J'' J'$. For example, for the oxygen R9Q10 line, R9 means the transition between $J''_{\rm rot} = 9 \rightarrow J'_{\rm rot} = 10$, whilst Q10 indicates $J'' = J' = 10$, which means that the transition is from $\Omega'' = 1$ to $\Omega' = 0$. This also indicates that the transition occurs between different electronic states. In practice, for the homonuclear diatomic molecules, there is no pure vibrational and rotational transitions.

For the polyatomics, such as H_2O, O_3 and NO_2. which are nonlinear triatomic and asymmetric rotators, their vibrations and rotations can be in any direction. Vibrational energy levels are then described by three different quantum numbers, i.e., (v_1, v_2, v_3) corresponding to three different vibrations. The rotational energy level can also be described by the projection of the rotational quantum number on different symmetry axis. The three vibrational quantum numbers are often used to describe different transition bands, e.g., (301)→(000).

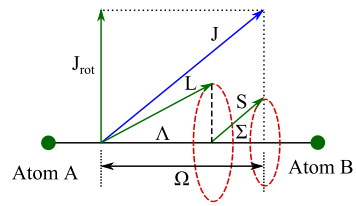

Figure 4.5. Angular moments of a two-atom molecule. Λ and Σ are the projections of the electron orbital angular momentum (L) and spin angular momentum (S) along the direction of the bond, $\Omega = |\Lambda + \Sigma|$. The symbols for different values of Λ are 0-Σ, 1-Π, 2-Δ and 3-Φ. The value of Σ can be $-S, ...S-1, S$. The electronic energy state of molecules is denoted by $^{2S+1}\Lambda_\Omega$. When considering the contribution of the electron angular momentum, the pure rotational quantum number ($J_{\rm rot}$) is also often denoted as N. For details, see Chapter 9 in the book written by Demtröder [256].

Oxygen and water vapor spectra

Figure 4.6 shows oxygen and water vapor absorption spectra around 760 nm and 935 nm as obtained from the high-resolution transmission molecular absorption (HITRAN) database. These absorption lines have been extensively used in Papers **I**, **V**, **VI**, **VII**, and **VIII**. The oxygen absorption lines are due to the transition from the ground state $X^3\Sigma_{\rm g}^-$ ($\nu'' = 0$) to the excited state $b^1\Sigma_{\rm g}^+$ ($\nu' = 0$),[7] i.e., the so-called oxygen A band. The water vapor absorption lines are the transitions of the (301)→(000) band. As can be seen, the absorption cross-section of water vapor is around 30 times larger. However, we should note that, the water vapor generally has much lower concentration than that of oxygen.

[7] "+/-" denotes symmetry, and "g/u" denotes parity. Symmetry describes the reflection at a plane through the nucleus, even↔+, odd↔-. Parity: the symmetry of the wavefunction with regard to a reflection of all coordinates at the origin, the parity could be even (gerade, g) and odd (ungerade, g), and only present for diatomics with equal nuclear charge. In diatomics, the ground state is labelled by X, excited states with the same spin number are labelled with ascending energy with A, B, C,... Excited states with different spin number are labelled with a, b, c,...

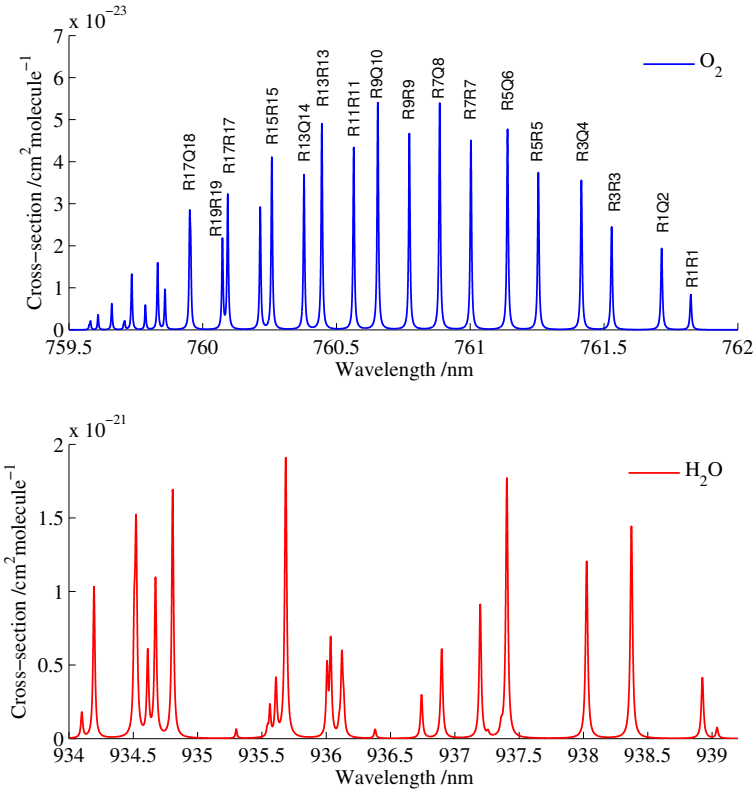

Figure 4.6. Oxygen and water vapor absorption cross-sections at 296 K and 1 atm pressure, around 760 nm and 935 nm, respectively.

4.4 Tunable diode lasers

In the above discussions, we know that a typical absorption linewidth for molecules at atmospheric conditions is in the order of GHz. In order to perform high resolution absorption spectroscopy, especially when studying the effect of different broadening mechanisms, a very narrow-band light source is extremely important for performing accurate and sensitive absorption measurements. In this section, we will first briefly review the development history of tunable diode lasers, and then discuss the details of wavelength tuning mechanisms and how to reduce the bandwidth of diode lasers. Finally, we discuss a bit about the diode lasers used in this thesis work.

4.4.1 Brief history

The first diode laser based on a GaAs homojunction diode was invented in 1962 [266–270]. The principle of the diode laser is that photons are generated when the electrons and holes are recombined in the p-n junction of a semiconductor diode.[8] The first homojunction diode laser, emitting laser radiation at 842 nm, was rather broadband (1.5 nm), and could only work in pulsed mode since the current threshold was high. In 1970, the double-heterojunction diode laser was invented [271, 272], which confines both the photons and carriers in the active layer by using cladding materials with larger band gap and lower refractive index. With such a configuration, the diode laser is able to work at room temperature and the threshold current is substantially reduced. A typical structure of a FP diode laser is given in Fig. 4.7.

However, the spectral characteristics are still quite poor for the conventional FP diode laser due to low finesse of the FP cavity and multiple longitudinal modes oscillation. The main reason for the multimode output of the FP diode lasers is that all cavity modes have the same loss, and the gain profile of the semiconductor materials is much broader than the FP cavity mode spacing,[9] which results in a very poor mode discrimination [274]. In the ideal case, single mode output can be obtained even for a small amount of gain margin as a result of the mode competition, as long as the gain profile is homogeneously broadened. However, this cannot be fulfilled in practice due to, e.g, large spontaneous emission [275, 276]. One commonly used method to reduce the broad bandwidth and achieve single-mode output is to introduce frequency selective optical feedback (increase mode discrimination) e.g., distributed feedback (DFB) or distributed Bragg-reflector (DBR) diode lasers [277] and external cavity diode laser (ECDL) [278–280]. Before discussing the details of these techniques, we would first introduce the basic mechanisms of wavelength tuning.

Material	Wavelength /nm
InGaN	390-420
AlGaInP	630-680
GaAlAs	620-895
GaAs	760-1083
InGaAsP	1100-1650
InGaAsSb	1700-4400
PbEuSeTe	3300-5800
PbSSe	4200-4800
PbSnTe	6300-29 000
PbSnSe	8000-29 000

Table 4.1. Composition and nominal wavelengths for a few commercial diode lasers [281, 282]. The wavelength for each material can vary by changing the ratio of the constituents.

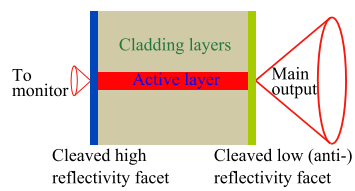

Figure 4.7. Simple sketch of an FP diode laser with high-low reflective facets. Typical dimensions for FP lasers: height 0.1-0.2 μm, cavity length L=250-500 μm, and width 5-15 μm. Considering a refractive index of $n = 3.6$, the typical free spectral range ($c/2nL$) is around 100 GHz.

4.4.2 Wavelength tuning mechanisms

The emitted wavelength is mainly determined by the band gap of the semiconductor materials. The wavelength of the diode laser can easily be tuned up to 20 nm by changing the operation temperature. The temperature variation induces changes of refractive index followed by the variation of optical pathlength, and change of band gap due to the thermal expansion of the lattice constants [285, 286]. The change of band gap results in a shift of gain peak.

[8] The main differences between a diode laser and the broadband light-emitting-diodes (LEDs) are the presence of optical feedback from the high reflectivity facets with the simplest case of a Fabry-Pérot (FP) cavity, and population inversion induced by a large injection current.

[9] Correspondingly, one way to attain single-mode output is to shorten the cavity length to 50 -100 μm [273].

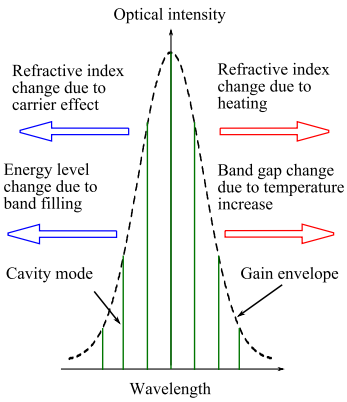

Figure 4.8. Tuning mechanisms of the lasing wavelength for diode lasers [283]. Band filling: the lower energy states in the conduction and valence bands are occupied first. As the increasing of the carrier concentration, the concentration of the high-energy carriers increases [284]. The band filling effect results in a blue shift.

Different mechanisms of wavelength tuning are shown in Fig. 4.8 [283]. The change of the optical pathlength results in a wavelength shift for a longitudinal mode, much smaller than the variation of the temperature-dependent band gap.[10] The two effects result in changes of wavelength as a staircase with sloping steps in practice. Mod-hops occur due to the shift of gain profile when tuning the wavelength through temperature [287].

Wavelength tuning can also be fulfilled by changing the driving current, which results in also a temperature variation due to Joule heating and carrier density variation. This in turn contributes to the change of refractive index [288, 289]. However, such a current-induced temperature variation gradually decreases as the modulation frequency increases [290, 291]. As a result, the carrier density variation will dominate for high modulation frequency, e.g., above 1 MHz.[11] On the other hand, since the carrier concentration increases, the output power would also be enhanced as the current increases. Thus, when the laser wavelength is modulated through current, an accompanied modulation to the output power occurs. This is normally referred to as residual amplitude modulation (RAM) in TDLAS, and will be further discussed in Sect. 4.6.

4.4.3 Reducing bandwidth

As has been discussed above, the main problems of the FP diode laser are mod-hops, multimode output and broad bandwidth, which limit the application of high resolution TDLAS. In order to reduce the bandwidth, one way is to use diffraction gratings to select the oscillation mode, such as in the DFB diode laser and DBR diode laser. Another commonly used method is to introduce feedback using an external cavity, e.g., ECDL. We will now briefly introduce the basic principles of these diode lasers, which have very narrow-band single mode output. For a comprehensive introduction to DFB diode lasers as well as vertical cavity surface emitting diode lasers (VCSEL), quantum cascade laser (QCL), etc. the reader is referred to [292, 293].

DBR diode laser replaces the high reflectivity facets in the FP diode laser with Bragg gratings which can introduce high optical feedback with selective optical frequency determined by the Bragg grating. Thus, only cavity modes around the Bragg wavelength can get significant feedback, and single mode output is generated as a result of mode competition. This type of diode laser is often

[10] For example, in AlGaAs devices, 0.06 nm/K for optical pathlength variation, and 0.25 nm/K for band gap change [285].

[11] This could occur in, e.g., the frequency domain photon migration technique, where the modulation frequency varies from 10 MHz up to 1 GHz. However, the purpose is to modulate the light intensity instead of the wavelength.

referred to as two-section (Bragg grating section and gain section) DBR diode laser. The wavelength of the DBR diode laser can be tuned by changing the refractive index of the Bragg grating through injection current. The continuous tuning range is limited by the frequency spacing between the longitudinal modes (typically 1 nm or smaller) for two-section DBR diode lasers. However, a long discrete tuning range up to 10 nm can still be obtained, accompanied with mod-hopping [294–296]. By synchronously changing the current of the phase and Bragg sections of the three-section DBR diode laser, as shown in Fig. 4.9(a), continuous mod-hop free tuning range (up to 3-4 nm) can also be achieved [297]. The typical bandwidth of the DBR diode lasers is around 1-10 MHz. Wavelength tuning can also be fulfilled by changing the heat sink temperature, which changes both the cavity modes because of thermal expansion and the refractive index of the DBR.

DFB diode lasers incorporate a grating on the active layer along the cavity length to provide a very narrow band optical feedback. In the DFB diode laser, one of the facets is normally anti-reflection coated to avoid the cavity modes of a conventional FP cavity, and the grating then serves as one of the mirrors of the laser cavity. Thus, the oscillation wavelength is mainly determined by the grating. By tuning the temperature and current of the Bragg grating, the wavelength can be tuned. The DFB diode laser can provide a mod-hop free tuning range up to 1000 GHz through temperature, and around 40-100 GHz through current. Wide mod-hop free tunability through current injection can also be achieved by, e.g., phase tunable DFB diode lasers, multisection DFB diode lasers and sampled-grating DBR diode lasers [297–299].

ECDL introduces the optical feedback by employing an external cavity, which can either be a mirror or a grating. Thus, the longitudinal mode lasing in the diode laser must satisfy the phase requirements for both the internal and external cavities. For the ECDL with gratings, by synchronously rotating the grating and changing the length of external cavity, a long tuning range up to 15 nm can be achieved [300]. The ECDLs can provide an extremely narrow bandwidth with a long external cavity, e.g., hundreds of kHz [301] or even 10 kHz [302], much narrower than the typical bandwidth (1-10 MHz) of DFB/DBR diode lasers. However, the mechanical tuning of the gratings introduces system instabilities and might not be suitable for harsh environments or field measurements, while DFB/DBR diode lasers are mechanically and thermally robust, and insensitive to external vibration.

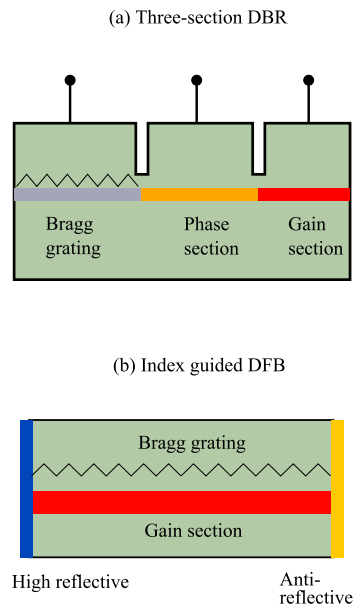

Figure 4.9. Typical structures of (a) three-section DBR diode laser and (b) index-coupled DFB diode laser. The three sections are: Bragg grating section, phase section, and gain section. The phase section is employed to achieve phase matching (or mod-hop free tuning) when changing the Bragg wavelength. The two-section DBR diode lasers do not have the phase control section. A supplier for two-section DBR diode lasers is, e.g, Photodigm. Most commercial suppliers only provide three-section DBR diode lasers.

Supplier	λ nm	$d\lambda/dT$ nm/K	$d\lambda/dI$ nm/mA	dP/dI mW/mA	Related work
Sacher-Laser	760	0.04	0.02	0.5	-
Eagleyard	760	0.06	0.003	0.8	-
Nanoplus	760	0.04	0.02	0.5	Paper **VIII**
Toptica	760	0.06	0.002	1.0	Paper **V**
					Paper **VI**
					Paper **VII**
					Paper **III**
Eagleyard	852	0.06	0.003	0.8	Paper **IV**
Nanoplus	935	0.08	0.02	0.4	Paper **VIII**
Eagleyard	937	0.06	0.003	0.8	Paper **I**
					Paper **II**

Table 4.2. Temperature tuning coefficients ($d\lambda/dT$), current tuning coefficients ($d\lambda/dI$) and slope efficiencies (dP/dI) for 760 nm distributed feedback (DFB) diode lasers from different suppliers.

4.4.4 DFB diode lasers used in this work

The DFB diode laser is one of the most popular diode lasers used in TDLAS applications [303]. In the present thesis work, quite a few DFB diode lasers from different suppliers are used for both gas absorption spectroscopy and light propagation studies. Typical characteristics for several diode lasers from different suppliers with different wavelengths are shown in Table 4.2. As can be seen, the temperature tuning coefficient is generally much larger than the current tuning coefficients. The current tuning coefficient is directly related to the refractive index of the grating, which increases as the temperature increases. The current-induced temperature variation is determined by the thermal resistance of the laser chip, depending upon the laser geometry, heat sink, and the way the laser chip is bonded onto the heat sink [304–307]. Larger thermal resistance gives a larger current tuning coefficient, but with a reduced speed of temperature and current tuning.

4.5 Detection sensitivity

The topic of this section is to discuss the detection sensitivity of the TDLAS technique, which is one of the most important parameters to characterize the system performance. Generally, there are two different definitions for detection sensitivity. One simple definition is the minimum detectable gas concentration with the unit of, e.g., ppmv and ppbv. However, it is sometimes not comparable because of different absorption cross-section for difference wavelengths and different species. Another common definition is the minimum detectable absorption coefficient $\alpha_{\min}$ [$\mathrm{cm}^{-1}/\sqrt{\mathrm{Hz}}$], or in absorbance unit – the minimum detectable absorption fraction $\kappa_{\min} = L\alpha_{\min}$ [$\mathrm{Hz}^{-1/2}$]. Here the absorbance is defined by using natural logarithm instead of using the common logarithm given

by Eq. (1.1), and $\sqrt{\text{Hz}}$ denotes the measurement bandwidth.[12] Such a definition is independent of gas species, and thus comparable between different measurement systems. The value of $\kappa_{\min}$ is obtained when SNR is equal to 1, which is also referred to as noise-equivalent detection sensitivity. We now give a brief discussion on the definition of the SNR in an optical system and the methods to increase the SNR.

According to the Beer-Lambert law, the detected intensity for weak absorption can be described by κI, where κ is the absorption fraction. The noise contribution can be categorized into three terms. The first type of noise comes from the intensity fluctuations of the non-ideal light source, which is proportional to the light intensity ($N_{\text{s}} I$). The detector electronics have noise which is independent of the light intensity (N_{e}). The last one is the shot-noise at the detector side, which originates from the statistic distribution of the detected photons and is proportional to the square root of the intensity ($\beta\sqrt{I}$). The SNR in an optical system is then given by [308]

$$\text{SNR} = \frac{\kappa I}{[N_{\text{e}}^2 + (\beta\sqrt{I})^2 + (N_{\text{s}} I)^2]^{1/2}}. \tag{4.17}$$

According to the above equation, one can simply increase the light intensity to gain the SNR, until the intensity fluctuation of the light source dominates the noise level. On the other hand, to achieve a shot-noise (quantum) limited detection, the other two sources of noise must be greatly suppressed. Fortunately, the noise originating from the light source and detector electronics are frequency dependent, and thus can both be suppressed by moving to a high-frequency detection band. This can be achieved through WMS and FMS discussed in Sect. 4.6. The detection sensitivity can reach up to $10^{-5} - 10^{-6}$ Hz$^{-1/2}$ through WMS and up to $10^{-6} - 10^{-8}$ Hz$^{-1/2}$ through FMS [244].

Another way to obtain a high SNR is to increase the absorption fraction κ, which can be achieved by employing multipass gas cells to increase the gas absorption pathlength. However, we should note that the noise-equivalent detection sensitivity $\kappa_{\min}$ determined by Eq. (4.17) does not change, although the minimum detectable absorption coefficient $\alpha_{\min}$ can be greatly improved. This approach actually has been widely used during recent decades. The most widely used commercial gas cells are the White [309] and Herriott [310] cells, where the pathlength can reach up to tens of meters [1]. Multipass gas cells employing integrating spheres, with

[12] The reason for the detection sensitivity with unit of per $\sqrt{\text{Hz}}$ instead of per Hz is because the noise spectrum is often defined as power (proportional to the square of the voltage) distribution among different frequencies, whilst the light intensity is converted into photocurrent or voltage. 1 Hz bandwidth is equivalent to half a second of integration time according to the Nyquist-Shannon sampling theorem.

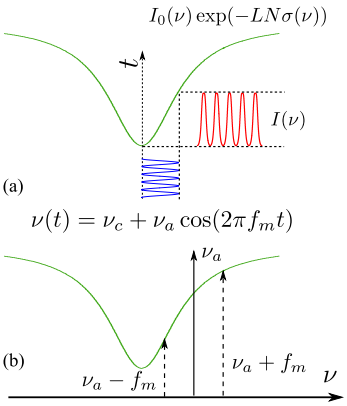

Figure 4.10. The principles of (a) WMS and (b) FMS. The transmission signal gets distorted because of nonlinear response; thus harmonics are generated.

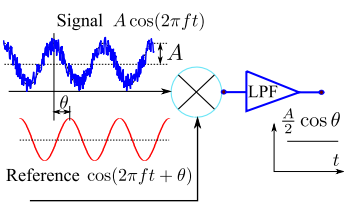

Figure 4.11. The principle of the analog lock-in amplifier, LPF corresponds to a low-pass filter or integration electronics. The maximum output is obtained when the two signals are in-phase, i.e., $\theta = 0$, and the noise level is greatly suppressed.

good misalignment tolerance but only a few-meter pathlength, have also been reported [311]. The most sensitive pathlength enhancement technique is CRDS or CEAS, where the pathlength is in the kilometer range. However, CRDS/CEAS requires high reflectivity mirrors and precision optical alignment.[13] Recently, by injecting the light beam off-axis of the cavity, a sensitivity of up to $10^{-11}\text{cm}^{-1}\text{Hz}^{-1/2}$ can be achieved in the near infrared region [236]. One should mention that with the NICE-OHMS technique based on the combination of FMS and on-axis CRDS, an astonishing detection sensitivity up to $10^{-14}\text{cm}^{-1}\text{Hz}^{-1/2}$ could be achieved at 1.064 μm [250].

4.6 Wavelength modulation spectroscopy

Wavelength modulation spectroscopy (WMS) [312] has been extensively used and has become a standard method in the TDLAS field. By employing optical wavelength modulation (a few kHz up to MHz) and scanning the laser center wavelength across the absorption line, high harmonics are generated due to the nonlinear response of the absorption line shape, as shown in Fig. 4.10(a). The $1/f$ noise can then be greatly suppressed, by moving the detection band to high frequency. The high harmonics can be detected through a lock-in amplifier by multiplying a reference sinusoidal wave or square wave with carefully controlled phase. Since the output of the product highly depends upon the phase difference between the harmonic and the reference signals, as shown in Fig. 4.11, this approach is also referred to as phase-sensitive detection (PSD).

When the modulation frequency is comparable with or larger than the linewidth of the gas absorption line, e.g., hundreds of MHz or several GHz, sidebands with the modulation frequency are generated, as shown in Fig. 4.10(b). The harmonics are then produced because of unequal attenuation on the sideband of the laser center frequency, again, resulting from the nonlinear response. The modulation method is then referred to as frequency modulation spectroscopy (FMS) [313]. The performance of FMS, in principle, should be better than that for WMS [314]. However, due to the system complexity of the radio frequency modulation/demodulation scheme and the electronic noise introduced by extremely high frequency modulation, the practical performance is generally lower than what is theoretically expected [315]. On the

[13] Although pulsed light sources are more frequently used in CRDS, one interesting observation is that CRDS was actually for the first time demonstrated by using intensity-modulated light source based on the phase-shift method (referred to as phase-shift CRDS) which was used to characterize the reflectivity/loss of the laser cavity and to measure the fluorescence lifetime in an even earlier time. To be noted, the phase shift method is referred to as frequency domain photon migration method in the biophotonic field.

other hand, by employing higher modulation frequency in WMS, e.g., up to 10 MHz, the detection sensitivity could be comparable with that obtained in FMS [316, 317].

The theory of the WMS technique has been thoroughly studied by many researchers [226, 318, 319]. In this thesis work, the WMS technique was performed in a digital way based on coherent data sampling and Fourier analysis. This approach was first demonstrated by Fernholz *et al.* in 2002 [320] by studying the Fourier spectrum of the detected signal. The phase term, which is a very critical parameter for the lock-in detection, is visualized or retrieved through a "sophisticated" phase-amplitude plot.

In this section, we will first introduce the harmonics of the WMS technique based on Fourier analysis, and then mathematically figure out the phase term, which hopefully can make the digital WMS method understandable.

4.6.1 Principles

According to the Beer-Larmbert law, in the case of weak absorption, the transmission light intensity is given by

$$I'(\nu') = I'_0(\nu') - LNI'_0(\nu')\sigma(\nu'). \tag{4.18}$$

In WMS, the wavelength is sinusoidally modulated through a corresponding modulation of the injection current. In practice, the change of wavelength has a phase shift (ϕ_1) compared with the current modulation [321], i.e.,

$$\nu'(t) = \nu_c + \nu_a \cos(2\pi f_m t - \phi_1 + \pi). \tag{4.19}$$

ν_c: laser center frequency
ν_a: modulation amplitude
f_m: modulation frequency

Here the phase term π is added because the optical frequency decreases as the injection current increases. As we will see later, the phase term π does not have any influence on the analysis. For tunable diode lasers, the optical wavelength modulation is accompanied with a modulation of intensity, which is often referred to as residual amplitude modulation (RAM). The output power is normally well in-phase with the modulation current. In case of any instrument-induced phase shift, we could still add a phase term to the power modulation for generality, which is given by[14]

$$I'_0(t) = I_0(\nu_c) + \kappa_1\nu_a \cos(2\pi f_m t + \phi_2). \tag{4.20}$$

[14] $I_0(\nu_c)$: laser intensity at center frequency, $\kappa_1 = (dI/di)/(d\nu/di)$ is the linear intensity-optical frequency modulation coefficient, i is the injection current. Here the nonlinear modulation is neglected.

Equation (4.18) can then be rewritten as

$$\begin{aligned} I'(t) = &[I_0(\nu_c) + \kappa_1\nu_a \cos(2\pi f_m t + \phi_2)] - \\ &LN\,[I_0(\nu_c) + \kappa_1\nu_a \cos(2\pi f_m t + \phi_2] \\ &\sigma\left(\nu_c + \nu_a \cos(2\pi f_m t - \phi_1 + \pi)\right). \end{aligned} \tag{4.21}$$

In order to facilitate the mathematical derivations, we hereby shift the phase term of the wavelength modulation to zero. From

another point of view, the time is translated by a factor of $(\phi_1 - \pi)/(2\pi f_m)$. The new transmission intensity is given by

$$S(t) = I'(t + (\phi_1 - \pi)/(2\pi f_{\mathrm{m}})) = I_0(t) - LNI_0(t)\sigma(\nu), \quad (4.22a)$$
$$\nu(t) = \nu_{\mathrm{c}} + \nu_{\mathrm{a}} \cos(2\pi f_{\mathrm{m}} t), \quad (4.22b)$$
$$I_0(t) = I_0(\nu_{\mathrm{c}}) + \kappa_1 \nu_{\mathrm{a}} \cos(2\pi f_{\mathrm{m}} t + \varphi), \quad (4.22c)$$

where

$$\varphi = \phi_1 + \phi_2 - \pi. \quad (4.23)$$

Equation (4.22a) can be rewritten as a background term and an absorption term

$$S_{\mathrm{abs}}(t) = -LNI_0(t)\sigma(\nu), \quad (4.24a)$$
$$S_{\mathrm{bg}}(t) = I_0(t). \quad (4.24b)$$

The Fourier series of $I_0(t)$ and $\sigma(\nu)$ can be expressed as:[15]

$$I_0(t) = \sum_{n=0}^{\infty} [I_n^{\mathrm{e}} \cos(2\pi n f_{\mathrm{m}} t)] + \sum_{n=1}^{\infty} [I_n^{\mathrm{o}} \sin(2\pi n f_{\mathrm{m}} t)], \quad (4.25)$$

$I_0^{\mathrm{e}} = I_0(\nu_{\mathrm{c}})$
$I_1^{\mathrm{e}} = \kappa_1 \nu_{\mathrm{a}} \cos(\varphi)$
$I_1^{\mathrm{o}} = -\kappa_1 \nu_{\mathrm{a}} \sin(\varphi)$

$$\sigma(\nu) = \sum_{m=0}^{\infty} [\sigma_m^{\mathrm{e}} \cos(2\pi m f_{\mathrm{m}} t)]. \quad (4.26)$$

Substituting Eqs. (4.25) and (4.26) into Eq. (4.24a), the even and odd terms of the absorption signal can be given by [226]:

$$S_{\mathrm{abs},k}^{\mathrm{e}} = -\frac{1}{2}LN \left[\sum_{n=0}^{k} \sigma_{k-n}^{\mathrm{e}} I_n^{\mathrm{e}} + (1 - \frac{1}{2}\delta_{k0}) \sum_{n=0}^{\infty} \sigma_n^{\mathrm{e}} I_{n+k}^{\mathrm{e}} + (1 - \frac{1}{2}\delta_{k0}) \sum_{n=0}^{\infty} \sigma_{n+k}^{e} I_n^{\mathrm{e}} \right], \quad (4.27)$$

$\delta_{k0} = \begin{cases} 1, & \text{if } k = 0 \\ 0, & \text{if } k \neq 0 \end{cases}$

$$S_{\mathrm{abs},k}^{\mathrm{o}} = -\frac{1}{2}LN(1 - \delta_{k0}) \left[\sum_{n=1}^{k} \sigma_{k-n}^{\mathrm{e}} I_n^{\mathrm{o}} - \sum_{n=0}^{\infty} \sigma_{n+k}^{\mathrm{e}} I_n^{\mathrm{o}} + \sum_{n=0}^{\infty} \sigma_n^{\mathrm{e}} I_{n+k}^{\mathrm{o}} \right]. \quad (4.28)$$

[15] According to a Taylor expansion, the value of $\sigma(\nu(t))$ for the optical frequency nearby the center frequency ν_{c} can be approximated by

$$\sigma(\nu(t)) = \sum_{m=0}^{\infty} \frac{\sigma^{(m)}(\nu_{\mathrm{c}})}{m!} \nu_{\mathrm{a}}^m \cos^m(2\pi f_{\mathrm{m}} t).$$

As can be seen, the Fourier series of the absorption cross-section only has even terms. According to Fermat's theorem, at the local maximum/minimum of $\sigma^{(m)}(\nu)$, the deviation, i.e., $\sigma^{(m+1)}(\nu)$ is equal to zero.

The transmission signal is then given by

$$S(t) = \sum_{k=0}^{\infty} S_k^{\mathrm{e}} \cos(2\pi k f_{\mathrm{m}} t) + \sum_{k=1}^{\infty} S_k^{\mathrm{o}} \sin(2\pi k f_{\mathrm{m}} t). \tag{4.29}$$

$$S_k^e = S_{\mathrm{abs},k}^{\mathrm{e}} + I_k^{\mathrm{e}}$$
$$S_k^{\mathrm{o}} = S_{\mathrm{abs},k}^{\mathrm{o}} + I_k^{\mathrm{o}}$$

Due to the presence of RAM, the k^{th} order harmonic also includes the effects from other harmonics. For instance, the first order harmonic ($1f$ absorption signal) is given by

$$S_1^{\mathrm{e}} = -LN\left[\sigma_1^{\mathrm{e}} I_0(\nu_{\mathrm{c}}) + \frac{2\sigma_0^{\mathrm{e}} + \sigma_2^{\mathrm{e}}}{2} I_1^{\mathrm{e}}\right] + I_1^{\mathrm{e}}, \tag{4.30a}$$

$$S_1^{\mathrm{o}} = -LN\left[\frac{2\sigma_0^{\mathrm{e}} + \sigma_2^{\mathrm{e}}}{2} I_1^{\mathrm{o}}\right] + I_1^{\mathrm{o}}. \tag{4.30b}$$

Because of the symmetry of the line shape function, the even order harmonics have the maximum at the center wavelength of the absorption line, while the odd order harmonics have a zero crossing. Consequently, the mean value of σ_k^{e} ($k \geq 1$) is equal to zero as long as the wavelength fully covers the absorption profile and the optical frequency is linearly scanned [320]. Although the mean value of σ_0^{e} is not equal to zero, $LN\sigma_0^{\mathrm{e}} << 1$. Thus, the RAM induces an offset (the mean value) on the first harmonic.

The k^{th} order harmonics ($k \geq 2$) are given by

$$S_k^{\mathrm{e}} = -LN\left[\sigma_k^{\mathrm{e}} I_0(\nu_{\mathrm{c}}) + \frac{\sigma_{k-1}^{\mathrm{e}} + \sigma_{k+1}^{\mathrm{e}}}{2} I_1^{\mathrm{e}}\right], \tag{4.31a}$$

$$S_k^{\mathrm{o}} = -LN\left[\frac{\sigma_{k-1}^{\mathrm{e}} - \sigma_{k+1}^{\mathrm{e}}}{2} I_1^{\mathrm{o}}\right]. \tag{4.31b}$$

The background signal does not have any influence on the second or higher harmonics. Since $I_0(\nu_{\mathrm{c}})$ and I_1^{e} experience the same transmission, one can use the average value of the $1f$ signal to calibrate the intensity $I_0(\nu_{\mathrm{c}})$ for the frequently used $2f$ signal. Thus, an intensity-corrected $2f$ signal can be obtained without measuring the light intensity with a reference measurement. However, due to distortion, the average value of the $1f$ signal does not always reflect the true value of I_1^{e}. The $2f$ signal instead is more frequently used, because of background immunity and relatively larger intensity compared with even higher harmonics.

4.6.2 Analogue lock-in detection

Conventionally, the $2f$ absorption signal is detected by the analogue lock-in amplifier, which has been used in many different applications for weak signal detection. The detected light signal is multiplied by a reference signal with frequency $k \times f_{\mathrm{m}}$ (k^{th} harmonic) and with an adjustable phase, to obtain the k^{th} order harmonic. We should note here, that the time of the absorption signal

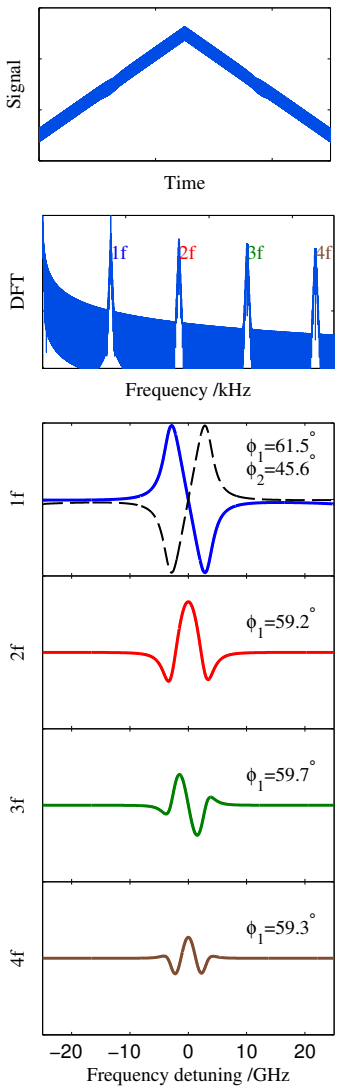

Figure 4.12. Simulation results for the WMS technique, the harmonic signals are obtained by performing Fourier analysis on the transmitted light signal. The value of ϕ_1 and ϕ_2 are set to $\pi/3$ and $\pi/4$, respectively. The discrepancies between the setting values and calculated values are mainly due to the computational errors. The dash-line for the $1f$ signal is plotted with time as x-axis (with the direction of increased wavelength).

has been linearly translated. Thus, the reference signal must also be translated by the same value. The k^{th} harmonic signal is given by

$$S_{\text{Analog},k} = \int_0^{1/f_{\text{m}}} [S_k^{\text{e}} \cos(2\pi k f_{\text{m}} t) + S_k^{\text{o}} \sin(2\pi k f_{\text{m}} t)] \cos(2\pi k f_{\text{m}} t + k\phi_1 - k\pi - \theta) dt. \tag{4.32}$$

Because of orthogonality, only the k^{th} order harmonic contributes to the output of the analog lock-in amplifier for the integration time $1/f_{\text{m}}$. When $\theta = k\phi_1$ (in-phase), only the even harmonics exist. On the contrary, if $\theta = k\phi_1 + \pi/2$ (out-of-phase), only the odd harmonics exist. An analog lock-in amplifier normally has both the in-phase and out-of-phase outputs. If θ is equal to $k\phi_1 + \arctan(S_k^{\text{o}}/S_k^{\text{e}})$, the r-component can be obtained, which is given by $\sqrt{(S_k^{\text{e}})^2 + (S_k^{\text{o}})^2}$; here we neglect the coefficient term.

4.6.3 Digital lock-in detection

In this thesis work, the harmonic signals are obtained by performing direct Fourier analysis on the detected signal, which is digitized by coherent sampling. Here, coherent sampling means that the sampling frequency is an integral-number times of the signal frequency. To be noted, the lock-in detection scheme can also be fulfilled digitally by using a digital phase-locked loop (PLL), similar to the procedure in analogue lock-in amplifiers [322]. The advantage of using Fourier analysis is to automatically find out the phase for lock-in detection. The Fourier transform of the original signal I' is given by

$$\begin{aligned}\mathcal{F}[I'(t)] =& \mathcal{F}[S(t - (\phi_1 - \pi)/(2\pi f_{\text{m}}))] \\ =& \mathcal{F}[S(t)] \exp[-i2\pi f(\phi_1 - \pi)/(2\pi f_{\text{m}})].\end{aligned} \tag{4.33}$$

Substituting the Fourier transform of $S(t)$, which can be easily obtained from the Fourier series, into the above equation, we have

$$\mathcal{F}[I'(t)] = \left\{ \sum_{k=0}^{\infty} (S_k^{\text{e}} - iS_k^{\text{o}})\, \delta(f - kf_{\text{m}}) + \sum_{k=1}^{\infty} (S_k^{\text{e}} + iS_k^{\text{o}})\, \delta(f + kf_{\text{m}}) \right\} \exp[-if(\phi_1 - \pi)/f_{\text{m}}]. \tag{4.34}$$

Applying a window function $w(f - kf_{\text{m}})$ (e.g., a Gaussian window) to the Fourier transform of $I'(t)$, the spectrum of the corresponding harmonic can be selected. The width of the window function is typically tenth of the modulation frequency, since sidebands are generated when linearly scanning the laser frequency. The Fourier

spectrum for each individual harmonic is given by

$$\begin{aligned} H_k^+(f) =& \mathcal{F}[I'(t)]w(f - kf_\mathrm{m}) \\ =& (S_k^\mathrm{e} - iS_k^\mathrm{o})\,\delta(f - kf_\mathrm{m})\exp[-if(\phi_1 - \pi)/f_\mathrm{m}]. \end{aligned} \tag{4.35}$$

Circulating/moving the center of the above spectrum to zero frequency, and performing an inverse Fourier transform, we get

$$\begin{aligned} h_k^+(t) =& 2\mathcal{F}^{-1}[H_k^+(f + kf_\mathrm{m})] \\ =& \frac{2\mathcal{F}^{-1}[H_k^+(f)]}{\exp(ik2\pi f_\mathrm{m}t)} \\ =& (S_k^\mathrm{e} - iS_k^\mathrm{o})\exp[-ik(\phi_1 - \pi)]. \end{aligned} \tag{4.36}$$

The task for now is to get the even harmonic (the in-phase term in the analogue lock-in amplifier) from Eq. (4.36). The challenge is to figure out the phase term $-k\phi_1$, as in the case of the analogue lock-in amplifier, which is normally found out by manually trying different phases. Let us consider the first harmonic separately, since the RAM contributes to the background signal of the harmonic signal. The first harmonic is given by

$$h_1^+(t) = \left[(S_{\mathrm{abs},1}^\mathrm{e} + I_1^\mathrm{e}) - i(S_{\mathrm{abs},1}^\mathrm{o} + I_1^\mathrm{o})\right]\exp(-i\phi_1 + i\pi). \tag{4.37}$$

As has been discussed above, the integration or average values of $S_{\mathrm{abs},k}^\mathrm{e}$ and $S_{\mathrm{abs},k}^\mathrm{o}$ are zero. Substituting the value of I_1^e and I_1^o , the mean value of $h_1^+(t)$ is calculated as

$$\langle h_1^+(t)\rangle = \kappa_1\nu_\mathrm{a}(\cos\varphi + i\sin\varphi)\exp(-i\phi_1 + i\pi). \tag{4.38}$$

The angle of the mean value is then given by $\varphi - \phi_1 + \pi = \phi_2$, which is the phase term of the power modulation. Subtracting the mean value from Eq. (4.37), one can get

$$h_1^+(t) - \langle[h_1^+(t)]\rangle = (S_{\mathrm{abs},1}^\mathrm{e} - iS_{\mathrm{abs},1}^\mathrm{o})\exp(-i\phi_1 + i\pi). \tag{4.39}$$

Since the frequency modulation amplitude ν_a is typically less than 10% of the scanning range, the value of I_1^e or I_1^o is typically much smaller than the value of $I_0(\nu_\mathrm{c})$.[16] Thus, at the maximum value of Eq. (4.39) which is generally the peak of the corresponding harmonic, the contribution from the odd term to the phase of the complex value is negligible, and the phase term $-\phi_1$ is approximately equal to the angle of the maximum value. By multiplying Eq. (4.39) with $\exp(i\phi_1)$, the real value of the product would be the even harmonic $S_{\mathrm{abs},1}^\mathrm{e}$. With the same protocol, the high harmonics can also be determined. However, the high harmonics are not affected by the background signal. Thus, the mean value term, in principle, is equal to zero. The phase term $-k\phi_1$ can then be directly obtained from the angle of the maximum value of the

[16] This does not hold for some extreme cases, e.g., one dramatically increases the value of ν_a, in spite of the optimal modulation amplitude, which is typically 2.2 times of the absorption linewidth [319].

$h_k^+(t)$. However, one should note, for the even order harmonics ($k = 2, 4, 6, ...$),

$$h_k^+(t) = \left(S^{\mathrm{e}}_{\mathrm{abs},k} - iS^{\mathrm{o}}_{\mathrm{abs},k}\right) \exp(-ik\phi_1 + i\pi), \tag{4.40}$$

at the maximum value of $h_k^+(t)$, the value of $\sigma^{\mathrm{e}}_{k\pm1}$ is zero, i.e., $S^{\mathrm{o}}_{\mathrm{abs},k}$ is equal to zero. The phase ϕ_1 can be then obtained from the maximum value without any approximation. Thus, for some extreme cases, the phase obtained from the even order harmonics can always be used to retrieve the odd harmonic signals. Figure 4.12 shows the simulation results with a Lorentzian line shape absorption profile, where the HWHM is set to be 1.5 GHz.

Chapter 5

Gas in Scattering Media Absorption Spectroscopy

5.1 Introduction

Gas in scattering media absorption spectroscopy (GASMAS) was introduced in 2001 to study gases enclosed in porous scattering media [39]. The mechanism of the GASMAS technique is based on the fact that the absorption imprint of a gas is approximately 10 000[1] times narrower than that for the surrounded solid/liquid-phase material.[2] By scanning the laser wavelength across the narrowband absorption lines of gases and examining the small absorption imprint superimposed on the highly reduced scattered light signal, one is able to retrieve the gas absorption signal and find out the concentrations of the enclosed gases in porous media. The main difference between the GASMAS technique and the traditional TDLAS technique is that the involved samples are turbid media where light has become completely diffused before arriving at the detector. Thus, there is no well-defined gas absorption pathlength in GASMAS applications. This has been a great challenge for the GASMAS technique, but also brought up possibilities for new applications, e.g., porosimetry studies [324], and random multipass gas cell applications [325, 326], as will be discussed in the following sections.

Since 2001, the GASMAS technique has been explored to various applications mainly for oxygen and water vapor detection. The corresponding absorption wavelengths are around 760 nm and 935 nm, respectively. The applications until now include wood material studies [15, 327, 328], fruits [329, 330] and food packaging monitoring [331, 332], pharmaceutical tablet characterization [324, 333], as well as human sinus [322, 334–336], mastoid [337] and lung function [338, 339] monitoring. By using different methodolo-

[1] The typical absorption linewidth for, e.g., oxygen in atmospheric condition is around 1.5 GHz@760 nm, while the linewidth of the absorption peak of mammalian fat at 760 nm is around 20 nm (10 000 GHz) [323].

[2] Gas bubbles in liquid media might also be possible to measure, although it has not been performed until now.

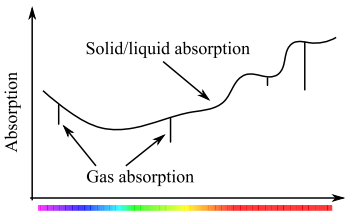

Figure 5.1. Principles of the GASMAS technique, the absorption spectrum of gas is substantially narrower than that of the solid/liquid-phase materials.

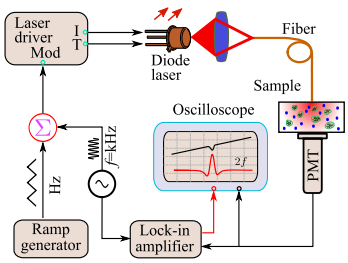

Figure 5.2. A typical schematic of the GASMAS technique, from Paper **IX**. The optical frequency of the diode laser is modulated by a high-frequency sinusoidal signal superimposed on a triangular signal. The absorption imprint is picked up by using a lock-in amplifier.

gies, either the gas concentration or the gas diffusion dynamics can be studied. Fundamental spectroscopic studies on wall collision broadening for gases enclosed in nano-porous ceramics were also investigated [340–342], which has been found to be very useful for non-intrusive pore size studies [343]. Reviews of the applications of GASMAS technique can be found in [344, 345]. The publications related to GASMAS in recent years have also been summarized in [346]. The efforts of the present thesis work on GASMAS are mainly aiming at finding out the unknown gas absorption pathlength based on different techniques (Papers **I** and **V**) and measuring the gas concentration without knowing the pathlength (Paper **VIII**). In the meanwhile, applications based on the combined method of pathlength measurement techniques and GASMAS are also explored to study the porosity of the medium (Papers **VI** and **VII**).

5.2 Methods and materials

5.2.1 Measurement principles

A typical GASMAS setup using a tunable narrow-band diode laser is shown in Fig. 5.2. The center wavelength of the diode laser is well controlled and stabilized through a thermoelectric cooler (TEC) controller. The WMS technique is utilized to pick up the weak absorption imprint from the strong and noisy background signal. The second harmonic absorption signal is recorded by an analogue lock-in amplifier [39] or digital lock-in amplifier based on Fourier analysis [320, 335], as discussed in Sect. 4.6. Since the absorption pathlength is unknown due to scattering, the absolute gas concentration is difficult to retrieve. In order to quantitatively give the measurement results, a mean equivalent pathlength (L_{eq}) is introduced, which is defined as the pathlength in a reference gas (typically ambient air) to experience an equivalent absorption as that in the porous medium. By fitting the absorption signal for the porous medium (S_{abs}, normally the $2f$ absorption signal) with the one for the reference gas cell ($S_{\mathrm{abs}}^{\mathrm{ref}}$), the value of L_{eq} is given by

$$L_{\mathrm{eq}} = \frac{S_{\mathrm{abs}}}{S_{\mathrm{abs}}^{\mathrm{ref}}} L_{\mathrm{gas}}, \tag{5.1a}$$

$$L_{\mathrm{eq}} = \frac{L_{\mathrm{gas}} C_{\mathrm{gas}}}{C_{\mathrm{ref}}}. \tag{5.1b}$$

Here L_{gas} and C_{gas} are the pathlength and concentration of the gas in the porous medium, respectively; C_{ref} is the gas concentration in the reference gas cell. Although the value of L_{eq} depends upon both the pathlength and the concentration of the enclosed gas, it is still used as key results for many applications [328, 331, 336], and especially useful for gas diffusion monitoring [328–330].

Since the applications of GASMAS for now involve mainly oxygen and water vapor, we will use these two gases as sample gases in the following sections. However, most of the techniques discussed below can be easily used for other gases with quite different absorption wavelengths, e.g., 2.05 μm for CO_2.

5.2.2 Porous materials

There are generally two main categories of porous media which are widely involved in GASMAS applications, as shown in Fig. 5.3.[3] One is the macroscopically homogeneous porous medium, e.g., wood, pharmaceutical tablets, polystyrene foams, and ceramics. The other one is an inhomogeneous porous medium with one or several cavities/porous surrounded by scattering materials, e.g., food packages, and human sinus cavities. We will now briefly introduce the porous media involved in this thesis.

[3] Ref. [347] summarizes another type of porous material – small scatterers surrounded by gases, e.g., cloud, and snow, where lidar techniques have been employed for gas concentration measurement [348].

Polystyrene foams (PS foams) are generally used as a reference porous scattering medium to develop various techniques for gas absorption pathlength evaluations. Actually, they have always been used as measurement samples since the first publication of GASMAS. One important feature of PS foams is the high porosity – as high as 98% [73]. The effective refractive index is approximately 1.01, as retrieved from the volume average of the refractive indices of polystyrene[4] and free air. The reduced scattering coefficient is around 34 cm^{-1}, whilst the absorption is negligible; see Paper **II**.

[4] The refractive indices for many materials can be found at: http://refractiveindex.info

Porous ceramics are one of the most widely used materials in our daily life. As pointed out by Richerson, "*most solid materials that aren't metal, plastic, or derived from plants or animals are ceramics*" [349]. Apart from traditional uses such as decorative ceramics, whiteware, and refractories, the advanced or technical ceramics are also widely used in, e.g., gas burner nozzles, biomedical implants, bearings [350]. In general, pores are everywhere in ceramics, and mostly created during fabrication. The porous ceramics are normally prepared by sintering - transforming the powder into a solid body by heating to high temperature. The porosity (fraction of void volume) and pore size are key characteristics of ceramic materials. In GASMAS applications, porous ceramics with different pore sizes and porosities, mainly made of, e.g., TiO_2, ZrO_2 and Al_2O_3, are frequently used as sample materials. In this work, the optical porosity of the ceramics is investigated by the GASMAS technique. In other scenarios, they can also be considered as a perfect macroscopically homogeneous model for studying light propagation in porous scattering media.

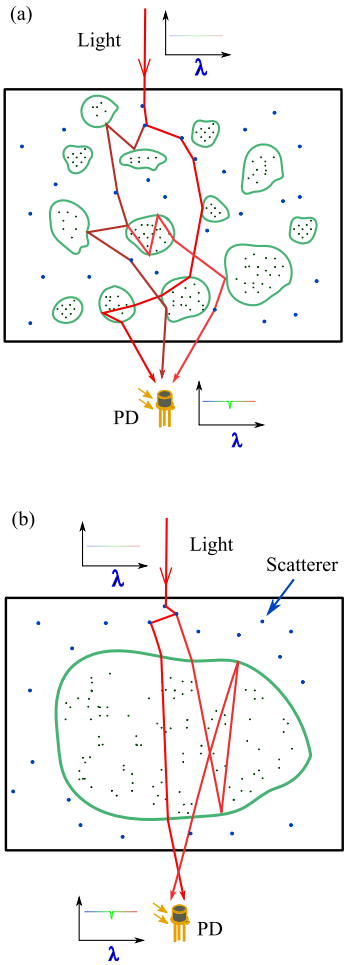

Figure 5.3. Light propagation in porous scattering media, from Paper **IX**: (a) Macroscopic homogeneous medium; (b) One or few large cavities surrounded by a scattering medium.

Food packaging – The aim of studying food packaging is to monitor the enclosed oxygen concentration which is a very critical parameter to control the quality, e.g., of milk in packages, since O_2 is a highly biologically active gas. The gas composition inside food packages is normally manipulated by lowering the concentration of O_2 and flushing with N_2 and CO_2, through well-developed modified atmospheric packaging (MAP) techniques [351–354]. Many traditional methods used for gas analysis in the food packaging industry, e.g., gas chromography and IR sensors, are based on gas extraction and are thus intrusive, and will destroy the samples being measured. Thus, non-intrusive gas detection techniques are highly demanded.

5.3 GASMAS challenge – unknown pathlength

As has been pointed out above, the pathlength through the enclosed gas is unknown due to heavy light scattering (see Fig. 5.3), which is governed by the RTE for macroscopically homogeneous porous media, as discussed in Chap. 2. In contrast, ray tracing optics can be used to study the porous media presented in Fig. 5.3(b) [355]. Substantial efforts have been devoted on finding out the unknown gas absorption pathlength in various GASMAS applications [73, 334], including Papers **I**, **V**, **VI**, **VII**, and **VIII**. In this section, we would only briefly introduce different methods to solve the challenge of unknown pathlength. For details, the reader is referred to Paper **IX**.

5.3.1 Pathlength calibration method

The first method is to simultaneously monitor another gas with known concentration, e.g., water vapor, the saturated concentration of which depends upon the temperature according to the Arden-Buck equation [356]. In this case, the pathlength for a water vapor absorption line (935 nm) can be obtained and is assumed to be the same as the pathlength for the gas of interest, e.g., oxygen (760 nm). Thus, the oxygen concentration can be retrieved. However, the assumption that the pathlength for these two wavelengths are the same is actually only approximately correct and for certain geometries large differences can occur. Another limitation for this method is that sometimes the saturation condition for water vapor is actually not fully satisfied, resulting in an underestimated pathlength of water vapor. However, for those cases with saturated water vapor concentration, the present method is a very powerful tool to evaluate the oxygen concentration, especially considering the use of a closer lying H_2O absorption line (e.g., 819.151 nm) to reduce the discrepancy of the pathlengths between H_2O and O_2.

5.3.2 Pathlength determination in porous media

Another method one can imagine is to measure the pathlength through the porous medium using other techniques. As has been discussed in Chaps 2 and 3, the TOFS, FDPM and FMLSI techniques are all able to measure the value of MOPL through the porous medium. By using MOPL as the pathlength of the gas, one can easily retrieve the gas concentration:

$$C_{\text{gas}} \approx \frac{L_{\text{eq}} C_{\text{ref}}}{L_{\text{m}}}. \tag{5.2}$$

However, since light passes through both the gas and the matrix material, the MOPL includes both the pathlength through gas (L_{gas}) and the pathlength through the matrix material (L_{s}):

$$L_{\text{m}} = L_{\text{gas}} + n_{\text{s}} L_{\text{s}}. \tag{5.3}$$

Here n_s is the refractive index of the matrix material. Thus, only an average gas concentration can be given. However, for media with extremely high porosity, e.g., polystyrene foams and the media shown in Fig. 5.3(b) where the scattering of the surrounded material is weak or even single scattering is dominant, the value of MOPL could give good approximation for the gas absorption pathlength.

We will now first briefly introduce the system and measurement principles of the combined method of the FDPM and the GASMAS techniques which is more frequently used, and then discuss the *pros* and *cons* of different pathlength determination methods.

Combination of the FDPM and the GASMAS techniques

The great advantage of employing the FDPM method is that the same diode laser used in the GASMAS system can also be used for the FDPM system as shown in Fig. 5.4, and demonstrated in Papers **V**, **VI** and **VII**. Apart from the basic equipment used in the GASMAS technique, only few additional RF components are used for the FDPM subsystem. The use of fibers for light illumination and collection enables many possibilities for different applications, but with reduced SNR.

Because of the amplitude-phase crosstalk discussed in Sect. 2.6, careful calibration must be performed during the FDPM measurements. The measurement procedure can be summarized as below:

(i) Measure the oxygen absorption signal in the porous medium and evaluate the pore pathlength based on a reference measurement in free air, as demonstrated in Eq. (5.1).

(ii) Measure the phase shift due to the scattering in the sample and the instrument response at different modulation frequencies.

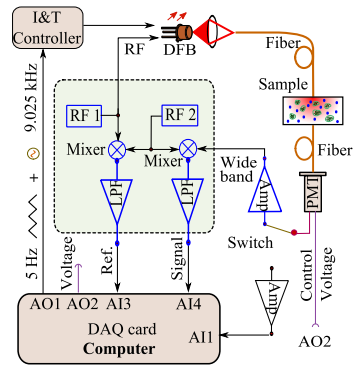

Figure 5.4. Schematic of the combined system of the GASMAS and the FDPM techniques, from Paper **VII**. The two subsystems cannot work simultaneously, but rather be switched through the electronic switch. The phase shift is detected by a heterodyne detection scheme with a frequency offset of 20 kHz. The fiber used on the illumination side is a multimode step index fiber with a core diameter of 1 mm, and the fiber for light collection is a fiber bundle with 2.5 mm diameter.

(iii) Measure the phase shift due to the instrument response by replacing the sample with an appropriate neutral density filter (i.e., causing similar light attenuation). The phase shift due only to the scattering in the turbid sample is then deduced. The optical properties can be retrieved by fitting the phase shift - frequency response based on diffusion approximation theory; whilst the MOPL value can be directly obtained based on the linear phase shift - frequency relationship for low modulation frequencies.

Comparison between different approaches

In spite of the scientific problem of using the total pathlength as the gas absorption pathlength, there are also several technical considerations when combining the pathlength measurement methods with the GASMAS technique. The difficulties of combining the TOFS and GASMAS techniques are obvious, i.e., the two techniques employ totally different light sources and detection schemes, as have been discussed in Papers **I** and **V**. Alternatively, the FDPM technique can be naturally incorporated into the GASMAS system, with a few additional RF components, as shown in Fig. 5.4. The limitation of the combination method between the FDPM and the GASMAS techniques for *in situ* measurements is the phase calibration procedure, which is hard to avoid and requires extra work. On the other hand, the FMLSI techniques, which can also be seamlessly incorporated into the GASMAS system, does not need any real time calibration; thus it would be a more attractive option if the SNR is good enough. However, the FMLSI technique generally has much lower SNR compared with the FDPM technique, since it distributes the total energy into beat signals with different beat frequencies, and more importantly only part of the scattered light can interfere. On the contrary, the TOFS technique in general has the highest SNR since it detects single photons. For practical applications, one should carefully consider the advantages and disadvantages of different methods.

5.3.3 Pathlength independent gas absorption spectroscopy

In Sect. 4.3, we have discussed that the line shape of the gas absorption cross section is dependent upon the intermolecular collisions with the same kind of molecules and with buffer molecules [259]. Clearly, from Eq. (4.11), the absorption line shape of, e.g., H_2O, depends upon the concentration of buffer gases, e.g., N_2, CO_2, and O_2. Typical collision broadening and line shift coefficients for water vapor are given in Table 5.1. We note that the broadening and line shift coefficients are quite small, and thus the line shape is not very sensitive to the variation of gas concentrations. This would be

Wavelength	Line broadening $cm^{-1}atm^{-1}$		Line shift $cm^{-1}atm^{-1}$	
	O_2	N_2	O_2	N_2
727.9389 [262]	0.0662	0.1038	-0.0277	-0.0133
730.6206 [262]	0.0547	0.0912	-0.0394	-0.0194
822.9218 [263]	—	0.082*	—	—
950.1690 [357]	—	0.1171	—	-0.012*
1383.8869 [358]	0.70	0.117	1.12	0.76

Table 5.1. Line shift and line broadening coefficients resulted from O_2 and N_2 for water vapor at different absorption lines, *Pressure broadening and shift in ambient air.

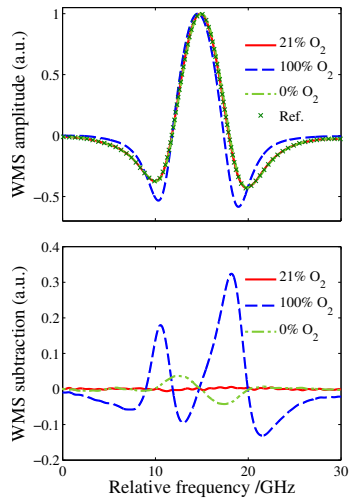

Figure 5.5. O_2 and N_2 concentration dependent water vapor absorption line profiles, from Paper **VIII**.

an ideal method to measure gas concentrations in GASMAS applications where the pathlength is unknown, although the sensitivity might be low. We refer to this method as pathlength independent GASMAS, which only means that we do not need to know the gas pathlength in order to get the concentration. However, measurement conditions must allow for obtaining a good SNR. For instance, the pathlength cannot be too small, or alternatively one can choose a stronger absorption line. In Paper **VIII**, we have demonstrated the application of the pathlength independent GASMAS technique on the O_2 and N_2 measurements on free gas mixture, by using a water vapor absorption line at around 935 nm and a scattering medium as a reference gas cell. This technique is also applicable for scattering media such as food packages. The water vapor absorption profiles for different concentrations of O_2 and N_2 are given in Fig. 5.5, the O_2 and N_2 concentration were retrieved by performing principal component analysis (PCA) based on the absorption spectra. An extra bonus of the pathlength independent GASMAS technique is that the concentrations of gases without any readily available absorption lines can also be measured. In practice, unpublished data reveals that the concentrations of four different gases can be measured by studying the line shape of a single absorption line. However, as pointed out above, this method is not very sensitive – typically 1% oxygen concentration can be resolved in food packaging. In spite of these drawbacks, this method is definitely an attractive method to evaluate the gas concentration in porous media, especially when high precision is not necessary.

5.4 Porosimetry studies

In the above discussion, we mainly focus on measuring the concentration of enclosed gas in porous media. Actually, many porous media, e.g., pharmaceutical tablets, aerogels, zeolites and ceramics, are in good ventilation condition with ambient air. Thus, the

enclosed water vapor or oxygen concentrations are generally the same as the ones for ambient air. For these porous media, people are more interested in their porous structures, e.g., porosity and pore size distribution [359], which determine the physical properties [360, 361], such as toughness, insulation, and permeability [362].

The two main methods which can measure the porosity and pore size of porous media, are the mercury intrusion porosimetry [363–366] and the gas adsorption porosimetry [367–370]. Other techniques such as thermal porosimetry [371], scanning electronic microscopy [372], light scattering methods [27], and X-ray tomography [373], are also used in some applications. The gas adsorption porosimetry can only measure the surface area with pore size from sub-nanometer up to 100 nm, while the mercury intrusion porosimetry can measure pore sizes up to 500 μm. A disadvantage of mercury intrusion porosimetry is that the sample may be destroyed due to high pressure [366]. As pointed out by Rouqueroll, there is generally no method which can measure the absolute porosity and pore size; each method has its own limitations [359]. In this thesis work, we have investigated the possibility to use optical methods to perform porosimetry studies on, e.g., ceramic samples, based on the combined methods of the GASMAS technique and the pathlength determination methods.

5.4.1 Optical porosity

In Sect. 5.3.2, we have pointed out that the pathlength measurement techniques can only measure the MOPL. Actually, GASMAS is the only method which can give the mean pathlength through the embedded gas in the porous media, if the gas concentration in the sample is known. For instance, gas concentration in the sample is the same as the one of ambient air, which is frequently used as the reference. In this case, the pathlength through the matrix material can be retrieved if the refractive index is known, as shown in Eq. (5.3). We then could define an optical porosity as the ratio between the pathlength through gas and the physical mean pathlength (L_{pm}) [324]:

$$L_{\mathrm{pm}} = L_{\mathrm{gas}} + L_{\mathrm{s}}, \tag{5.4a}$$

$$\phi_{\mathrm{OP}} = L_{\mathrm{gas}}/L_{\mathrm{pm}}. \tag{5.4b}$$

Based on the optical porosity, we could also simply give the effective refractive index, which is also *a priori* parameter to retrieve the optical properties, as below:

$$n_{\mathrm{eff}} = \frac{\mathrm{c}}{L_{\mathrm{pm}}/(L_{\mathrm{m}}/c)} = \frac{L_{\mathrm{m}}}{L_{\mathrm{pm}}} = (1-\phi_{\mathrm{OP}})n_{\mathrm{s}} + \phi_{\mathrm{OP}} n_{\mathrm{air}}. \tag{5.5}$$

Here n_{air} is the refractive index of air. Clearly, the value of optical porosity highly depends upon the physical porosity, the structures

and refractive index of the matrix (skeletal) material. The value of the optical porosity can give significant information on the structure of the porous medium. However, to find out the connections between optical and physical porosity is still a challenging task, which has not been fully understood. We now try to deduce an empirical formula based on the effective refractive index of the porous medium.

There are several models describing the relationship between the effective refractive index and the physical porosity, based on the effective medium model [374], e.g., the Bruggeman approximation [375], the Maxwell–Garnett mixing rule [376] and the Looyenga formula [377]. The Looyenga model (LM) is formulated as

$$n_{\text{eff-LM}}^{2/3} = (1-\phi_V)n_{\text{s}}^{2/3} + \phi_{\text{V}} n_{\text{air}}^{2/3}. \tag{5.6}$$

Here ϕ_{V} is the physical porosity or volume porosity. Generally, all these models do not consider multiple scattering, and are thus not suitable for turbid media. In order to connect the optical and physical porosities, we propose a modified Looyenga model (MLM) as given below

$$n_{\text{eff-MLM}}^{2/3} = (1-\phi_{\text{V}})^{\gamma} n_{\text{s}}^{2/3} + \phi_{\text{V}} n_{\text{air}}^{2/3}. \tag{5.7}$$

Here γ is a factor taking into account the scattering effect. Clearly, the optical and physical porosities are now connected through Eqs. (5.5) and (5.7). The empirical factor γ can be retrieved experimentally for individual material.

Actually, apart from the effective refractive index models mentioned above, another frequently used approximated model is the two-state model:

$$n_{\text{eff-2-state}} = (1-\phi_{\text{V}})n_{\text{s}} + \phi_{\text{V}} n_{\text{air}}. \tag{5.8}$$

It is a very interesting observation that the effective refractive index of scattering media also follows the two-state model but with optical porosity instead of physical porosity.

5.4.2 Ceramic studies

In the present thesis work, the optical porosities of ceramics were studied by the combined method of the FDPM and the GAS-MAS techniques, and the connections between optical and physical porosities are studied, as demonstrated in Paper **VII**. The ceramic samples studied are Al_2O_3 porous ceramics with pore size of around 200 μm,[5] and with physical porosities in the range between 25% and 80%.

Figure 5.6 shows the effective refractive index given by different approaches. As can be seen, a nonlinear relationship between the physical porosities and the effective refractive indices is observed.

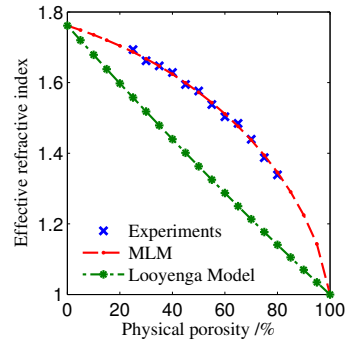

Figure 5.6. Effective refractive indices for alumina oxide porous ceramic samples obtained from the measured results, the Looyenga model and the modified Looyenga model (MLM), from Paper **VII**. The studied porous ceramics are made of alumina oxide by sintering the powder (0.5 μm and 2.0 μm) for 48 hours at 1700°C. The porous ceramics with porosity smaller than 70% are made of 0.5 μm Al_2O_3 powder, while the others are made of 2 μm powders.

[5] Microporous: <2 nm, Mesoporous: 2-50 nm, Macroporous: >50 nm.

In other words, the optical and physical porosities have nonlinear relationship since the effective refractive index is a linear function of optical porosity. As can be seen from Fig. 5.6, the MLM successfully connects the optical and physical porosities. The agreement between the optical porosities obtained for ceramics with different pore sizes (see Ref. [324] and Paper **VII**) indicates that the relationship between optical and physical porosities could be independent of the pore size, as long as the pore size is not significantly smaller than the wavelength.

The reduced scattering coefficients for the ceramic samples with porosity smaller than 70% are substantially lower than others; see Paper **VII**. However, the effective refractive indices of all these samples fit very well with the same γ factor. This indicates that the γ factor does not really depend on the scattering coefficient in the case of highly diffusive media. However, if the scattering is too weak or even absent, the value of γ would approach 1, and Eq. (5.7) transfers into Eq. (5.6). From the experimental results, we can conclude that the γ factor is mainly dependent upon the refractive index of the matrix material for the highly scattering media. Further studies regarding optical and physical porosities with different materials would definitely increase the understanding of such a relationship.

5.5 Discussion

In the previous sections, three different approaches are presented to retrieve the absolute gas concentration in turbid media. Each of the methods has its own specific advantages, but also with shortcomings. Depending upon applications, the appropriate approach should be selected.

The pathlength calibration method is very efficient for food packaging measurements if the saturated water vapor concentration is satisfied. However, this method may be restricted to measure oxygen, which has very close absorption lines to the strong water absorption lines. In industrial applications, one is also interested in measuring the concentration of CO_2, the strong absorption lines of which are around 2.05 μm. Thus, it would be difficult to measure the CO_2 concentration using the pathlength calibration method since the pathlength discrepancy for the absorption lines is now quite large.[6] However, in this case, the scattering for 2.05 μm is generally much weaker, which means that the MOPL value may give an even better approximation for the gas absorption pathlength compared with the wavelength of 760 nm. This indicates a good possibility to use the second approach, e.g., the FDPM method, to measure the MOPL value with promising results expected. Currently, such a project is ongoing in our group.

The pathlength independent GASMAS method can be applied

[6] The water vapor absorption wavelengths are much shorter, e.g., 820 nm, 935 nm, and 1.4 μm.

in many applications, but the SNR must be high even for the strong attenuating scattering media. The simplest way of obtaining a higher SNR is to increase the output power of the laser or select a strong absorption line. In practice, it is of great importance to use strong absorption lines in GASMAS applications, since the pathlength is not significantly long to obtain high sensitivity. However, one should also carefully consider the line broadening and shift coefficients. For instance, the absorption line of water vapor in the 1.4-μm band, which has much stronger absorption cross-section compared with the one at other wavelengths, could be a good option for the pathlength independent GASMAS application. As shown in Table 5.1, it also gives much larger pressure broadening and shift coefficients.

The combined method of the pathlength measurement techniques and the GASMAS techniques also shows a great potential for porosimetry studies and light propagation studies in porous media. From the technique point of view, the best approach is to combine the FDPM and the GASMAS techniques, since the FDPM technique can be more easily integrated compared with TOFS, and it has a higher SNR than that of the FMLSI technique.

Chapter 6

Conclusion and Outlook

This thesis has demonstrated several approaches in solving the problem of unknown pathlength for absorption spectroscopy in turbid media.

The unknown gas absorption pathlength in turbid media is a very critical issue for the GASMAS technique, preventing successful measurement of absolute gas concentration. In this thesis work, mainly two different types of approaches are proposed, i.e., pathlength determination using the FDPM and the FMLSI techniques, and pathlength independent gas absorption spectroscopy. The first approach, seamlessly combining the pathlength measurement methods and the GASMAS technique, provides the possibility to obtain an average gas concentration, and enables non-intrusive porosimetry studies for porous media. In future work, the combination method could be developed to on-line gas monitoring in the application of, e.g., food packaging, where the total pathlength through the turbid media could give a good approximation on the gas absorption pathlength. The applications towards porosimetry studies are of great interest for characterizing structure of porous media, such as ceramics and aerogels. On the other hand, the combination method also shows great potential for studying light propagation in porous scattering media. This has not been thoroughly developed in the present thesis work; however, further studies on uniform porous samples with different characteristics should be performed to hopefully increase the knowledge on light propagation in porous media.

The pathlength independent gas absorption spectroscopy seems to be the only method so far which can measure the absolute gas concentration in porous media without any approximation. This method should definitely be developed in future work, especially when the SNR is not a limitation. The great advantages of monitoring gases without any readily available absorption lines should be fully utilized, e.g., Ar and N_2 concentration measurements. On

the other hand, this feature can always be used to retrieve concentrations of additional gases apart from the gases of interest. Notably, high sensitivity cannot be expected.

The FMLSI technique, utilizing a coherent tunable light source and examining the intensity fluctuation through scattering samples, provides a new possibility of light propagation studies in turbid media. The highlights of the FMLSI technique, compared with the traditional methods, are the system simplicity and the possibility of simultaneously retrieving dynamics and structure of turbid media. In this work, we mainly focus on the assessment of the optical properties – reduced scattering coefficient and absorption coefficient. Future work could be the applications of the FMLSI technique in various turbid media, e.g., dairy products, human tissues, and colloidal suspensions in general. On the other hand, the FMLSI technique should also be further developed to study the dynamics and structure of turbid media for, e.g., food safety applications.

Appendix A

Interference

The interference signal between the signal waves with TOF τ_i and the reference wave is given as

$$I^i(t) = I^i_{\mathrm{DC}} + A_{\mathrm{ref}} \underbrace{\sum A^{i,j}_{\mathrm{sig}} \cos\left[2\pi\beta\tau_i t + \theta^{i,j}_{\mathrm{diff}}\right]}_{B^i_{\mathrm{sig}}(t)}. \tag{A.1}$$

The beat signals included in the summation function can be expanded as

$$\begin{aligned} B^i_{\mathrm{sig}}(t) =& \sum A^{i,j}_{\mathrm{sig}} \cos\left(2\pi\beta\tau_i t\right) \cos\left(\theta^{i,j}_{\mathrm{diff}}\right) \\ & - \sum A^{i,j}_{\mathrm{sig}} \sin\left(2\pi\beta\tau_i t\right) \sin\left(\theta^{i,j}_{\mathrm{diff}}\right) \\ =& \cos\left(2\pi\beta\tau_i t\right) \underbrace{\sum A^{i,j}_{\mathrm{sig}} \cos\left(\theta^{i,j}_{\mathrm{diff}}\right)}_{X} \\ & - \sin\left(2\pi\beta\tau_i t\right) \underbrace{\sum A^{i,j}_{\mathrm{sig}} \sin\left(\theta^{i,j}_{\mathrm{diff}}\right)}_{Y}. \end{aligned} \tag{A.2}$$

Define C^i_{sig} as

$$\begin{aligned} {C^i_{\mathrm{sig}}}^2 =& X^2 + Y^2 \\ =& \left[\sum A^{i,j}_{\mathrm{sig}} \cos\left(\theta^{i,j}_{\mathrm{diff}}\right)\right]^2 + \left[\sum A^{i,j}_{\mathrm{sig}} \sin\left(\theta^{i,j}_{\mathrm{diff}}\right)\right]^2 \\ =& \sum {A^{i,j}_{\mathrm{sig}}}^2 \cos^2(\theta^{i,j}_{\mathrm{diff}}) + \sum_{j\neq k} A^{i,j}_{\mathrm{sig}} A^{i,k}_{\mathrm{sig}} \cos\left(\theta^{i,j}_{\mathrm{diff}}\right) \cos\left(\theta^{i,k}_{\mathrm{diff}}\right) \\ & + \sum {A^{i,j}_{\mathrm{sig}}}^2 \sin^2(\theta^{i,j}_{\mathrm{diff}}) + \sum_{j\neq k} A^{i,j}_{\mathrm{sig}} A^{i,k}_{\mathrm{sig}} \sin\left(\theta^{i,j}_{\mathrm{diff}}\right) \sin\left(\theta^{i,k}_{\mathrm{diff}}\right) \\ =& \sum {A^{i,j}_{\mathrm{sig}}}^2 + \sum_{j\neq k} A^{i,j}_{\mathrm{sig}} A^{i,k}_{\mathrm{sig}} \cos\left(\theta^{i,j}_{\mathrm{diff}} - \theta^{i,k}_{\mathrm{diff}}\right). \end{aligned} \tag{A.3}$$

Equation (A.2) can ben rewritten as

$$\begin{aligned} B^i_{\text{sig}}(t) =& C^i_{\text{sig}} \left(\frac{X}{C^i_{\text{sig}}} \cos\left(2\pi\beta\tau_i t\right) - \frac{Y}{C^i_{\text{sig}}} \sin\left(2\pi\beta\tau_i t\right) \right) \\ =& C^i_{\text{sig}} \cos\left(2\pi\beta\tau_i t + \theta^i_{\text{diff}}\right). \end{aligned} \tag{A.4}$$

Here θ^i_{diff} is given by

$$\tan(\theta^i_{\text{diff}}) = \frac{Y}{X} = \frac{\sum A^{i,j}_{\text{sig}} \sin\left(\theta^{i,j}_{\text{diff}}\right)}{\sum A^{i,j}_{\text{sig}} \cos\left(\theta^{i,j}_{\text{diff}}\right)}. \tag{A.5}$$

If the phase term $\theta^{i,j}_{\text{diff}}$ varies randomly with time, the ensemble average of ${C^i_{\text{sig}}}^2$ can be given as

$$\begin{aligned} \left\langle {C^i_{\text{sig}}}^2 \right\rangle =& \int \left\{ \sum {A^{i,j}_{\text{sig}}}^2 + \sum_{j \neq k} A^{i,j}_{\text{sig}} A^{i,k}_{\text{sig}} \cos\left(\theta^{i,j}_{\text{diff}} - \theta^{i,k}_{\text{diff}}\right) \right\} dt \\ =& \sum {A^{i,j}_{\text{sig}}}^2. \end{aligned} \tag{A.6}$$

Appendix B

Dynamic Light Scattering

Here we will give a theoretical description of the dynamic light scattering (DLS) technique when examining particles undergoing Brownian motion. For even more detailed description, the reader is referred to the book written by Berne and Pecora [26]. Based on the first Born approximation, that the light field inside the scattering volume is constant and is equal to the incident light field, the amplitude of the incident light field for all particles can be written as [378]

$$E_{\text{in}}(\mathbf{r}_n(t), t) = E_0 \exp\left[i\left(\mathbf{k}_\text{i}\mathbf{r}_n(t) - \omega_0 t\right)\right]. \tag{B.1}$$

Here $\mathbf{r}_n(t)$ gives the position of the particles. According to the Rayleigh scattering theory, a spherical light wave with the same frequency would be produced by the induced dipole. The scattered light originating from N independent particles in a given volume V detected at $\mathbf{R}$, can be given as (see Fig. B.1)

$$E_\text{s}(t) \propto E_0 \sum_{n=1}^{N} \exp\left[i\mathbf{k}_\text{i}\mathbf{r}_n(t)\right] \frac{\exp\left(i\left|\mathbf{k}_\text{i}\right|\left|\mathbf{R} - \mathbf{r}_n(t)\right|\right)}{\left|\mathbf{R} - \mathbf{r}_n(t)\right|}. \tag{B.2}$$

With the far-field approximation, i.e., $|\mathbf{R}| >> |\mathbf{r}_n(t)|$, we then have

$$\left|\mathbf{R} - \mathbf{r}_n(t)\right| \approx R - \mathbf{r}_n(t)\frac{\mathbf{k}_\text{s}}{\left|\mathbf{k}_\text{s}\right|}, \tag{B.3}$$

$$\begin{aligned}
\frac{1}{\left|\mathbf{R} - \mathbf{r}_n(t)\right|} =& \frac{1}{R}\frac{1}{\sqrt{1 + r_n^2(t)/R^2 - 2\mathbf{R}\mathbf{r}_n(t)/R^2}} \\
\approx& \frac{1}{R}\frac{1}{\sqrt{1 - 2\mathbf{R}\mathbf{r}_n(t)/R^2}} \\
\approx& \frac{1}{R}\left[1 + 2\mathbf{R}\mathbf{r}_n(t)/R^2\right]. \\
\approx& \frac{1}{R}
\end{aligned} \tag{B.4}$$

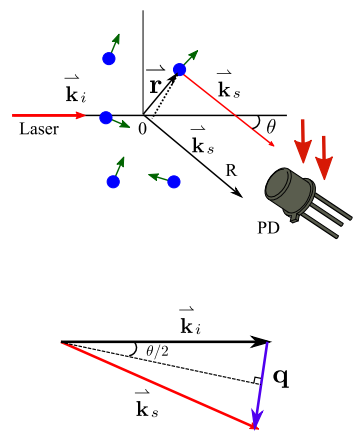

Figure B.1. Schematic of the DLS technique.

Since $|\mathbf{k}_\mathrm{i}| \approx |\mathbf{k}_\mathrm{s}|$, Eq. (B.2) can then be rewritten as

$$E_\mathrm{s}(t) \propto E_0 \frac{\exp(i\mathbf{k}_\mathrm{i}\mathbf{R})}{R} \sum_{n=1}^{N} \exp\left[i\mathbf{q}\mathbf{r}_n(t)\right]. \tag{B.5}$$

Here $\mathbf{q}$ is the scattering vector, given by

$$\mathbf{q} = \mathbf{k}_\mathrm{s} - \mathbf{k}_\mathrm{i}. \tag{B.6}$$

Thus,

$$q = 2k_\mathrm{i} \sin(\theta/2). \tag{B.7}$$

The normalized electric field amplitude autocorrelation function, which is often referred to as the first order autocorrelation function, is written as

$$\begin{aligned} g^{(1)}(\tau) =& \frac{\langle E_\mathrm{s}^*(t) E_\mathrm{s}(t+\tau)\rangle}{\langle E_\mathrm{s}^*(t) E_\mathrm{s}(t)\rangle} \\ =& \frac{1}{N} \left\langle \sum_{m,n} \exp\left[i\mathbf{q}(\mathbf{r}_m(t+\tau) - \mathbf{r}_n(t))\right] \right\rangle. \end{aligned} \tag{B.8}$$

Since the particles move independently, correlations between the displacements of different particles vanish. Considering that all particles are governed by the same statistics, and letting $\mathbf{r}(0) = 0$ ($t = 0$), Eq. (B.8) can be written as

$$g^{(1)}(\tau) = \langle \exp[i\mathbf{q}\mathbf{r}(\tau)]\rangle = F(\mathbf{q}, t). \tag{B.9}$$

The value of $\langle \exp[i\mathbf{q}\mathbf{r}(\tau)]\rangle$ depends upon the probability density ($\psi(\mathbf{r}, t)$) of the particles. $F(\mathbf{q}, t)$ can be calculated as the ensemble average in a volume V:

$$F(\mathbf{q}, t) = \int_V \psi(\mathbf{r}, t) \exp[i\mathbf{q}\mathbf{r}(t)] d^3r. \tag{B.10}$$

Equation (B.10) indicates that the average value is actually the Fourier transform of the probability density function. Considering particles undergoing Brownian motion, the probability density function satisfies the following diffusion equation:

$$D_\mathrm{B} \nabla^2 \psi(\mathbf{r}, t) = \frac{\partial}{\partial t} \psi(\mathbf{r}, t). \tag{B.11}$$

The diffusion constant D_B can be given by the Stokes-Einstein relationship. Applying the Fourier transform on the partial differential equation, Eq. (B.11) gives

$$D_\mathrm{B} q^2 F(\mathbf{q}, t) = \frac{\partial}{\partial t} F(\mathbf{q}, t). \tag{B.12}$$

The solution of the above equation can be simply given by

$$F(\mathbf{q}, t) = \exp(-D_\mathrm{B} q^2 t). \tag{B.13}$$

Thus, the first order autocorrelation function can be rewritten as

$$g^{(1)}(\tau) = \exp(-D_{\mathrm{B}} q^2 \tau). \tag{B.14}$$

The power spectrum of the detected light intensity is then the Fourier transform of the autocorrelation function, which gives

$$\begin{aligned} S^{(1)}(f) =& \mathrm{Re}\left[\int g^{(1)}(\tau)\exp(-i2\pi f\tau)d\tau\right] \\ \propto& \frac{1}{\pi f_0}\frac{1}{1+(f/f_0)^2}. \end{aligned} \tag{B.15}$$

Here $f_0 = D_{\mathrm{B}} q^2/2\pi$ is the linewidth of the Lorentzian line shape. In the above discussion, the electric field amplitude is examined, which can be experimentally obtained by employing a heterodyne detection scheme. For the frequently used homodyne detection, only the intensity autocorrelation, which is often referred to as the second-order autocorrelation, is available. However, similar results can still be obtained:

$$g^{(2)}(\tau) = 1 + \left|g^{(1)}(\tau)\right|^2. \tag{B.16}$$

The power spectrum is given by

$$S^{(2)}(f) \propto \frac{1}{\pi 2 f_0}\frac{1}{1+(f/2f_0)^2}. \tag{B.17}$$

Comments on the Papers

I **Gas spectroscopy and optical path-length assessment in scattering media using a frequency-modulated continuous-wave diode laser**
L. Mei, H. Jayaweera, P. Lundin, S. Svanberg, and G. Somesfalean

A frequency-modulated continuous-wave diode laser is utilized as the light source of a Mach-Zehnder interferometer to measure the optical pathlength through scattering media. The water vapor absorption inside the porous polystyrene foams is also studied by using the same diode laser. The combination method provides the possibility to study the gas concentration of porous media using a compact and cheap setup.

Hiran Jayaweera and I initiated the project. I was later in charge of the experimental work, and finished the measurements. I programmed the control software, did the data analysis, and wrote the manuscript draft.

II **Characterization and validation of the frequency-modulated continuous-wave technique for assessment of photon migration in solid scattering media**
L. Mei, P. Lundin, S. Andersson-Engels, S. Svanberg, and G. Somesfalean

This work was aimed at characterizing and validating the frequency-modulated continuous-wave technique, and comparing with the results obtained by time-of-flight spectroscopy. The theoretical aspects of the technique were also carefully studied, and the origin of the spikes superimposed on the power spectrum was also investigated.

I was in charge of the experimental work. I programmed the control software, did the data analysis, and wrote the manuscript draft.

III **Frequency-modulated light scattering in colloidal suspensions**
L. Mei, S. Svanberg, and G. Somesfalean

This work was the first time to test the frequency-modulated continuous-wave technique in liquid media, where both light scattering and Doppler shifts resulting from the scattering particles undergoing Brownian motion were studied. The technique is referred to as frequency-modulated light scattering interferometry (FMLSI). The optical properties and Brownian motion of the liquid phantom samples made from Intralipid and India ink were studied. The FMLSI technique showed good linearity and reproducibility.

I pursued the experimental work, programmed the data acquisition software, did the complicated data analysis and wrote the manuscript draft.

IV **Frequency-modulated light scattering interferometry employed for optical properties and dynamics studies of turbid media**
L. Mei, G. Somesfalean, and S. Svanberg

This work was aiming at developing a fiber based frequency modulated light scattering interferometry system for light propagation studies in general. With the fiber configuration, the optical properties and Brownian motion could be studied with different measurement geometries. In this paper, both liquid phantom samples made of Intralipid and static turbid media (polystyrene foam) were studied. The promising results demonstrated a great potential to use the present method for various applications.

I designed the system, did the measurements and data analysis. I wrote the manuscript draft.

V **Combined optical porosimetry and gas absorption spectroscopy in gas-filled porous media using diode-laser-based frequency domain photon migration**
L. Mei, S. Svanberg, and G. Somesfalean

This work combined the frequency domain photon migration (FDPM) method which was widely used in the biomedical field, and the gas in scattering media absorption spectroscopy (GASMAS) technique into a single setup. The total pathlength through the porous medium was measured by the FDPM method, while the absorption signal was obtained through the GASMAS technique. Such a combination system could not only provide the possibility to retrieve gas concentration in porous media, but also enable porosimetry studies for porous media in general.

I designed the measurement system and software program, performed the measurement and data analysis, and wrote the manuscript draft.

VI **Optical porosimetry in wood using oxygen absorption spectroscopy and frequency domain photon migration**
L. Mei, J. Larsson, S. Svanberg, and G. Somesfalean

This work utilized the frequency domain photon migration (FDPM) method and gas in scattering media absorption spectroscopy (GASMAS) technique to study the porosity of wood material, specifically pine and balsa wood samples.

I took part in the measurements, performed the data analysis and wrote the manuscript draft.

VII **Light propagation in porous ceramics: optical properties and porosity studies using tunable diode laser spectroscopy**
L. Mei, G. Somesfalean, and S. Svanberg

This paper was to utilize the combination method of frequency domain photon migration (FDPM) method and gas in scattering media absorption spectroscopy (GASMAS) technique to study the porosities of ceramics made of aluminum oxide powder. The optical porosities, defined as the ratio of the gas absorption pathlength and total pathlength, were investigated for porous ceramics with different physical or volume porosities. The relationship between optical and physical properties was investigated and connected through a modified effective refractive index model.

I was in charge of the project, I did the measurements and data analysis, and made the program. I wrote the manuscript draft.

VIII **Laser spectroscopic gas concentration measurements in situations with unknown optical path length enabled by absorption line shape analysis**
P. Lundin, L. Mei, S. Andersson-Engels, and S. Svanberg

This paper demonstrated for the first time how to retrieve the gas concentration, potentially in scattering porous media, without knowing the gas absorption pathlength, based on the gas absorption line shape analysis. Gas mixtures with different concentrations of oxygen and nitrogen were investigated by studying the water absorption line shape around 935 nm.

I participated in the experimental work and data analy-sis, and I also contributed to the manuscript.

IX **Pathlength determination for gas in scattering media absorption spectroscopy**
L. Mei, G. Somesfalean, and S. Svanberg

This paper was to review the efforts during the recent ten years to solve the problem of unknown gas absorption pathlength in gas in scattering media absorption spectroscopy (GASMAS) applications. Three different approaches were summarized, i.e., calibrating the pathlength with another gas, measuring the total pathlength through the porous media using another techniques, and retrieving the gas concentration based on absorption line shape analysis. The perspectives for the different approaches were discussed.

I wrote the manuscript draft and prepared most of the figures.

Acknowledgements

It is almost six years, since I started my graduate study at Zhejiang University, Hangzhou, where I did embark on a lidar research program together with Sune Svanberg and Gabriel Somesfalean. I was really impressed by the enthusiasm of Sune which has been emphasized by each of his PhD student, and from that moment I knew what a real scientist should be. Partly because of the collaboration work, I came to Europe and to Sweden for the first time after the project was finished in 2010. With the support from a 1.5-year Erasmus Mundus scholarship, I got the opportunity to study at the Atomic Physics Division, Lund University. Very luckily, the scholarship was later extended to 34 months in total. During this period, I was also part of the collaboration work between Zhejiang University, South China Normal University and Lund University, with quite a few projects. Last summer, I finished my PhD at Zhejiang University, China, with the topics of lidar techniques and applications. After that, I came back to Sweden and continued my work in Lund to finish my PhD studies at the Atomic Physics Division. I would never reach this moment without the help from many people. It was and will always be a fantastic memory whenever I look back on the time I spent with friends and colleagues during my PhD career. I would now like to thank many people here.

First, I would like to thank my supervisors Sune Svanberg, Gabriel Somesfalean and Stefan Andersson-Engels. Sune, who I own my deepest respect, is not only the main supervisor for the present thesis, but also the *de facto* supervisor for my Chinese thesis. I am so lucky to have you as my supervisor during my whole PhD career. Sune, thank you for always encouraging me and providing help whenever I had problems. I would always remember your enthusiasm whenever I would have doubts on my future work. Gabriel, thank you so much for your great help both in research and daily life. Without your help, it was not possible for me to come to Sweden and finish my PhD here in Lund. I also learnt a lot from the infinite number of conversations in Chinese between us on many topics. I wish you a great success for your future career. Stefan, thank you for unselfish help which smoothened my PhD

study in Lund. Thank you also for the many discussions we had. I always got some "fresh air" when I walked out from your office.

Warmest thanks also go to Katarina Svanberg for taking care of me in your house and providing great support in research. Patrik Lundin, I greatly appreciate the wonderful discussion we had and the enjoyable time we spent together in the lab. Mikkel Brydegaard, thank you for funny and interesting discussions. Jim, thanks for joining in our group. You helped us speed up the research project a lot. Prof. Jiandong Hu, thanks for bringing pleasure in the office and much help in research projects. Thanks to Anders Persson for being of great help in many optics and lasers problems. Special thanks to Haiyan Xie for helping me in many research projects, and her family for taking care of me. Thanks to Haichun Liu, Ying Yan, Chen Guo, Zhiyuan Xie, Qian Li, and Can Xu for the enjoyable time we spent together during lunches, dinners, chats and games. Thanks to Stefanos Carlström for always sharing funny things, and Chinese greetings when we met in the corridor. I would also like to thank Camilla Nilsson for helping me figure out an infinite number of administrative problems, especially for the PhD registration troubles. Thanks to Henrik Steen and Anne Petersson-Jungbeck for all help in administrative issues. Warm thanks also to Sofia Shen, who helped me a lot with the Erasmus Mundus scholarship, and special help for the support of extending my scholarship period. I would also like to thank all former and current colleagues in Atomic Physics Division for creating a warm research environments. I very much enjoyed the time I spent in our division.

I am also grateful for the support from Prof. Sailing He, who provides an international research platform at Zhejiang University where I started my graduate study. Thanks also go to my colleagues at Zhejiang University and South China Normal University. They are Chunsheng Yan, Zuguang Guan, Guangyu Zhao, Binhao Wang, Yongjiang Dong, Hongze Lin, Weijia Zhong, Xuan Liu, Yuan Fu, Chao Feng, Ying Shen, and Haojiang Zhou. Thanks for all the happy time we spent together in the office and lab. Special thanks to Guangyu Zhao for taking care of me when I was in Guangzhou for collaboration projects.

I am extremely fortunate to have a warm and harmonic family. Any words fail to express my deepest grateful to my parents, who supported my study all these years and gave me infinite love. The support from my loved sister - Ying Mei is also extremely important. I am also grateful to my parents in law; their trust and encouragement provide me confidence for my PhD work. Finally, I would like to thank my beloved wife - Hui Li, who has always been by my side to trust me, encourage me, and make life wonderful. With her infinite love, I can always proceed forwards without any fear of failure.

References

1. J. Hodgkinson and R. Tatam, "Optical gas sensing: A review," *Meas. Sci. Technol.* **24**, 012004 (2013).

2. B. V. L'vov, "Fifty years of atomic absorption spectrometry," *J. Anal. Chem.* **60**, 382–382 (2005).

3. G. D. Christian and F. J. Feldman, *Atomic Absorption Spectroscopy: Applications in Agriculture, Biology, and Medicine* (R. E. Krieger Pub. Co., Huntington, New York, 1979).

4. B. Stuart and D. J. Ando, *Biological Applications of Infrared Spectroscopy*, Analytical Chemistry by Open Learning (Published on behalf of ACOL (University of Greenwich) by John Wiley, Chichester, New York, 1997).

5. J. B. Hearnshaw, *The Analysis of Starlight: One Hundred and Fifty Years of Astronomical Spectroscopy* (Cambridge University Press, Cambridge, New York, 1990), 1st pbk. ed.

6. S. Svanberg, *Atomic and Molecular Spectroscopy: Basic Aspects and Practical Applications* (Springer, Berlin, New York, 2004), 4th, rev. ed.

7. P. Bouguer, "Essai d'optique, sur la gradation de la lumière," *France: Claude Jombert* pp. 16–22 (1729).

8. J. H. Lambert, "Photometry, or, on the measure and gradations of light, colors, and shade," *Germany: Eberhardt Klett* p. 391 (1760).

9. A. Beer, "Determination of the absorption of red light in colored liquids," *Annalen der Physik und Chemie* **86**, 78–88 (1852).

10. R. Richards Kortum and E. Sevick Muraca, "Quantitative optical spectroscopy for tissue diagnosis," *Annu. Rev. Phys. Chem.* **47**, 555–606 (1996).

11. F. Bevilacqua, A. J. Berger, A. E. Cerussi, D. Jakubowski, and B. J. Tromberg, "Broadband absorption spectroscopy in turbid media by combined frequency-domain and steady-state methods," *Appl. Opt.* **39**, 6498–6507 (2000).

12. G. Zonios, A. Dimou, I. Bassukas, D. Galaris, A. Tsolakidis, and E. Kaxiras, "Melanin absorption spectroscopy: New method for noninvasive skin investigation and melanoma detection," *J. Biomed. Opt.* **13**, 014017 (2008).

13. J. M. Murkin and M. Arango, "Near-infrared spectroscopy as an index of brain and tissue oxygenation," *British Journal of Anaesthesia* **103**, i3–i13 (2009).

14. S. Tsuchikawa and S. Tsutsumi, "Application of time-of-flight near-infrared spectroscopy to wood with anisotropic cellular structure," *Appl. Spectrosc.* **56**, 869–876 (2002).

15. I. Bargigia, A. Nevin, A. Farina, A. Pifferi, C. D'Andrea, M. Karlsson, P. Lundin, G. Somesfalean, and S. Svanberg, "Diffuse optical techniques applied to wood characterisation," *Journal of Near Infrared Spectroscopy* **21**, 259–268 (2013).

16. F. Pandozzi and D. H. Burns, "Power law analysis estimates of analyte concentration and particle size in highly scattering granular samples from photon time-of-flight measurements," *Anal. Chem.* **79**, 6792–6798 (2007).

17. Z. Q. Shi and C. A. Anderson, "Pharmaceutical applications of separation of absorption and scattering in near-infrared spectroscopy (NIRS)," *J. Pharm. Sci.-US* **99**, 4766–4783 (2010).

18. D. Khoptyar, A. A. Subash, S. Johansson, M. Saleem, A. Sparén, J. Johansson, and S. Andersson-Engels, "Broadband photon time-of-flight spectroscopy of pharmaceuticals and highly scattering plastics in the VIS and close NIR spectral ranges," *Opt. Exp.* **21**, 20941–20953 (2013).

19. O. H. A. Nielsen, A. A. Subash, F. D. Nielsen, A. B. Dahl, J. L. Skytte, S. Andersson-Engels, and D. Khoptyar, "Spectral characterisation of dairy products using photon time-of-flight spectroscopy," *Journal of Near Infrared Spectroscopy* **21**, 375–383 (2013).

20. A. Wax and V. Backman, *Biomedical Applications of Light Scattering*, Biophotonics series (McGraw-Hill, New York, 2010).

21. T. Durduran, R. Choe, W. B. Baker, and A. G. Yodh, "Diffuse optics for tissue monitoring and tomography," *Rep. Prog. Phys.* **73**, 076701 (2010).

22. S. L. Jacques, "Optical properties of biological tissues: A review," *Phys. Med. Biol.* **58**, R37–R61 (2013).

23. M. J. Rakovic, G. W. Kattawar, M. Mehrubeoglu, B. D. Cameron, L. V. Wang, S. Rastegar, and G. L. Cote, "Light backscattering polarization patterns from turbid media: Theory and experiment," *Appl. Opt.* **38**, 3399–3408 (1999).

24. M. Canpolat and J. R. Mourant, "Particle size analysis of turbid media with a single optical fiber in contact with the medium to deliver and detect white light," *Appl. Opt.* **40**, 3792–3799 (2001).

25. A. Wax, C. H. Yang, V. Backman, M. Kalashnikov, R. R. Dasari, and M. S. Feld, "Determination of particle size by using the angular distribution of backscattered light as measured with low-coherence interferometry," *J. Opt. Soc. Am. A* **19**, 737–744 (2002).

26. B. J. Berne and R. Pecora, *Dynamic Light Scattering: with Applications to Chemistry, Biology, and Physics* (Dover Publications, Mineola, New York, 2000), Dover ed.

27. W. W. Chen and B. Dunn, "Characterization of pore-size distribution by infrared scattering in highly dense ZnS," *J. Am. Ceram. Soc.* **76**, 2086–2092 (1993).

28. J. Manara, R. Caps, F. Raether, and J. Fricke, "Characterization of the pore structure of alumina ceramics by diffuse radiation propagation in the near infrared," *Opt. Commun.* **168**, 237–250 (1999).

29. J. Manara, R. Caps, and J. Fricke, "Characterization of the pore structure of ceramics via propagation of light and infrared radiation," *Int. J. Thermophys.* **26**, 531–542 (2005).

30. Z. G. Guan, P. Lundin, L. Mei, G. Somesfalean, and S. Svanberg, "Vertical lidar sounding of atomic mercury and nitric oxide in a major Chinese city," *Appl. Phys. B* **101**, 465–470 (2010).

31. L. Mei, G. Y. Zhao, and S. Svanberg, "Differential absorption lidar system employed for background atomic mercury vertical profiling in South China," *Opt. Laser Eng.* **55**, 128–135 (2014).

32. U. Platt and J. Stutz, *Differential Optical Absorption Spectroscopy: Principles and Applications*, Physics of Earth and Space Environments, (Springer, Berlin, 2008).

33. Y. Deguchi, *Tunable Diode Laser Absorption Spectroscopy*, pp. 176–208 (CRC Press Taylor Francis Group, 2012).

34. M. N. Fiddler, I. Begashaw, M. A. Mickens, M. S. Collingwood, Z. Assefa, and S. Bililign, "Laser spectroscopy for atmospheric and environmental sensing," *Sensors-Basel* **9**, 10447–10512 (2009).

35. L. Mei, P. Lundin, G. Somesfalean, J. D. Hu, G. Y. Zhao, S. Svanberg, J. Bood, M. Vrekoussis, and A. Papayannis, "First attempt to monitor atmospheric glyoxal using differential absorption lidar," in Proceedings of SPIE Remote Sensing, vol. 8534, p. 853412 (2012).

36. R. Merrill and J. Colby, *Handbook Optical Remote Sensing for Measurement and Monitoring of Emissions Flux* (U.S. Environmental Protection Agency, 2011).

37. Y. Deguchi, *Industrial Applications of Laser Diagnostics* (CRC Press, Boca Raton, FL, 2012).

38. J. A. C. Broekaert, *Analytical Atomic Spectrometry with Flames and Plasmas* (Wiley-VCH, Weinheim Chichester, 2005), 2nd completely rev. and extended ed.

39. M. Sjöholm, G. Somesfalean, J. Alnis, S. Andersson-Engels, and S. Svanberg, "Analysis of gas dispersed in scattering media," *Opt. Lett.* **26**, 16–18 (2001).

40. L. V. Wang and H.-i. Wu, *Biomedical Optics: Principles and Imaging* (Wiley, 2007).

41. A. J. Welch and M. J. C. van Gemert, *Optical-Thermal Response of Laser-Irradiated Tissue*, Lasers, Photonics, and Electro-Optics (Springer Science+Business Media, New York, 2011).

42. J. R. Lorenzo, *Principles of Diffuse Light Propagation: Light Propagation in Tissues with Applications in Biology and Medicine* (World Scientific, Singapore, 2012).

43. L. G. Henyey and J. L. Greenstein, "Diffuse radiation in the galaxy," *Astrophys. J.* **93**, 70–83 (1941).

44. G. M. Hale and M. R. Querry, "Optical-constants of water in 200-nm to 200-μm wavelength region," *Appl. Opt.* **12**, 555–563 (1973).

45. "Tabulated molar extinction coefficient for hemoglobin in water," (2010). URL http://omlc.ogi.edu/spectra/hemoglobin/summary.html.

46. W. M. Star, J. P. A. Marijnissen, and M. J. C. van Gemert, "Light dosimetry in optical phantoms and in tissues.1. Multiple flux and transport-theory," *Phys. Med. Biol.* **33**, 437–454 (1988).

47. S. T. Flock, M. S. Patterson, B. C. Wilson, and D. R. Wyman, "Monte carlo modeling of light propagation in highly scattering tissue – I: Model predictions and comparison with diffusion theory," *IEEE Trans. Biomed. Eng.* **36**, 1162–1168 (1989).

48. L. Wang, S. L. Jacques, and L. Zheng, "MCML–Monte Carlo modeling of light transport in multi-layered tissues," *Comput. Meth. Prog. Bio.* **47**, 131–146 (1995).

49. E. Alerstam, T. Svensson, and S. Andersson-Engels, "Parallel computing with graphics processing units for high-speed Monte Carlo simulation of photon migration," *J. Biomed. Opt.* **13**, 060504 (2008).

50. W. C. Y. Lo, K. Redmond, J. Luu, P. Chow, J. Rose, and L. Lilge, "Hardware acceleration of a Monte Carlo simulation for photodynamic therapy treatment planning," *J. Biomed. Opt.* **14**, 014019 (2009).

51. L. H. Wang and S. L. Jacques, "Hybrid model of Monte Carlo simulation and diffusion-theory for light reflectance by turbid media," *J. Opt. Soc. Am. A* **10**, 1746–1752 (1993).

52. T. Hayashi, Y. Kashio, and E. Okada, "Hybrid Monte Carlo-diffusion method for light propagation in tissue with a low-scattering region," *Appl. Opt.* **42**, 2888–2896 (2003).

53. H. O. Di Rocco, D. I. Iriarte, J. A. Pomarico, and H. F. Ranea-Sandoval, "Acceleration of Monte Carlo modeling of light transport in turbid media: An approach based on hybrid, theoretical and numerical calculations," *J. Quant. Spectrosc. Rad. Transf.* **110**, 307–314 (2009).

54. C. G. Zhu and Q. Liu, "Review of Monte Carlo modeling of light transport in tissues," *J. Biomed. Opt.* **18**, 50902 (2013).

55. F. Martin, A. Klar, E. W. Larse, and S. Yasuda, "Approximate models of radiative transfer," *Bull. Inst. Math. Acad. Sin.* **2**, 409–432 (2007).

56. Y. Bayazitoglu and J. Higenyi, "Higher-order differential-equations of radiative-transfer – P3 approximation," *AIAA J.* **17**, 424–431 (1979).

57. D. Contini, F. Martelli, and G. Zaccanti, "Photon migration through a turbid slab described by a model based on diffusion approximation. 1. Theory," *Appl. Opt.* **36**, 4587–4599 (1997).

58. D. Dickey, O. Barajas, K. Brown, J. Tulip, and R. B. Moore, "Radiance modelling using the P3 approximation," *Phys. Med. Biol.* **43**, 3559–3570 (1998).

59. M. Frank, A. Klar, E. W. Larsen, and S. Yasuda, "Time-dependent simplified P_N approximation to the equations of radiative transfer," *J. Comput. Phys.* **226**, 2289–2305 (2007).

60. L. M. Zhang, J. Li, X. Yi, H. J. Zhao, and F. Gao, "Analytical solutions to the simplified spherical harmonics equations using eigen decompositions," *Opt. Lett.* **38**, 5462–5465 (2013).

61. K. M. Yoo, F. Liu, and R. R. Alfano, "When does the diffusion-approximation fail to describe photon transport in random-media," *Phys. Rev. Lett.* **64**, 2647–2650 (1990).

62. S. Fantini, M. A. Franceschini, and E. Gratton, "Semi-infinite-geometry boundary-problem for light migration in highly scattering media - A frequency-domain study in the diffusion-approximation," *J. Opt. Soc. Am. B* **11**, 2128–2138 (1994).

63. K. Furutsu and Y. Yamada, "Diffusion-approximation for a dissipative random medium and the applications," *Phys. Rev. E.* **50**, 3634–3640 (1994).

64. T. Durduran, A. G. Yodh, B. Chance, and D. A. Boas, "Does the photon-diffusion coefficient depend on absorption?" *J. Opt. Soc. Am. A* **14**, 3358–3365 (1997).

65. E. Alerstam, S. Andersson-Engels, and T. Svensson, "Improved accuracy in time-resolved diffuse reflectance spectroscopy," *Opt. Exp.* **16**, 10440–10454 (2008).

66. T. Travainen, *Computational Methods for Light Transport in Optical Tomography*, Ph.D. thesis, University of Kuopio (2006).

67. S. Arridge, M. Cope, and D. Delpy, "The theoretical basis for the determination of optical pathlengths in tissue: Temporal and frequency analysis," *Phys. Med. Biol.* **37**, 1531–1560 (1992).

68. S. R. Arridge, "Optical tomography in medical imaging," *Inverse Probl.* **15**, R41–R93 (1999).

69. A. Pifferi, A. Torricelli, A. Bassi, P. Taroni, R. Cubeddu, H. Wabnitz, D. Grosenick, M. Moller, R. Macdonald, J. Swartling, T. Svensson, S. Andersson-Engels, R. L. P. van Veen, H. J. C. M. Sterenborg, J. M. Tualle, H. L. Nghiem, S. Avrillier, M. Whelan, and H. Stamm, "Performance assessment of photon migration instruments: the MEDPHOT protocol," *Appl. Opt.* **44**, 2104–2114 (2005).

70. A. Pifferi, A. Torricelli, P. Taroni, D. Comelli, A. Bassi, and R. Cubeddu, "Fully automated time domain spectrometer for the absorption and scattering characterization of diffusive media," *Rev. Sci. Instrum.* **78**, 053103 (2007).

71. P. Di Ninni, F. Martelli, and G. Zaccanti, "Effect of dependent scattering on the optical properties of intralipid tissue phantoms," *Biomed. Opt. Express* **2**, 2265–2278 (2011).

72. A. Duncan, J. H. Meek, M. Clemence, C. E. Elwell, L. Tyszczuk, M. Cope, and D. T. Delpy, "Optical pathlength measurements on adult head, calf and forearm and the head of the newborn-infant using phase-resolved optical spectroscopy," *Phys. Med. Biol.* **40**, 295–304 (1995).

73. G. Somesfalean, M. Sjöholm, J. Alnis, C. af Klinteberg, S. Andersson-Engels, and S. Svanberg, "Concentration measurement of gas embedded in scattering media by employing absorption and time-resolved laser spectroscopy," *Appl. Opt.* **41**, 3538–3544 (2002).

74. R. C. Haskell, L. O. Svaasand, T. T. Tsay, T. C. Feng, and M. S. Mcadams, "Boundary-conditions for the diffusion equation in radiative-transfer," *J. Opt. Soc. Am. A* **11**, 2727–2741 (1994).

75. M. S. Patterson, B. Chance, and B. C. Wilson, "Time resolved reflectance and transmittance for the noninvasive measurement of tissue optical-properties," *Appl. Opt.* **28**, 2331–2336 (1989).

76. J. B. Fishkin, S. Fantini, M. J. VandeVen, and E. Gratton, "Gigahertz photon density waves in a turbid medium: Theory and experiments," *Phys. Rev. E.* **53**, 2307–2319 (1996).

77. K. Shimizu, A. Ishimaru, L. Reynolds, and A. P. Bruckner, "Backscattering of a picosecond pulse from densely distributed scatterers," *Appl. Opt.* **18**, 3484–3488 (1979).

78. A. Ishimaru, "Diffusion of a pulse in densely distributed scatterers," *J. Opt. Soc. Am.* **68**, 1045–1050 (1978).

79. Y. Kuga, A. Ishimaru, and A. P. Bruckner, "Experiments on picosecond pulse-propagation in a diffuse medium," *J. Opt. Soc. Am.* **73**, 1812–1815 (1983).

80. S. Ito, "Comparison of diffusion theories for optical pulse waves propagated in discrete random-media," *J. Opt. Soc. Am. A* **1**, 502–505 (1984).

81. D. T. Delpy, M. Cope, P. Vanderzee, S. Arridge, S. Wray, and J. Wyatt, "Estimation of optical pathlength through tissue from direct time of flight measurement," *Phys. Med. Biol.* **33**, 1433–1442 (1988).

82. S. L. Jacques, "Time-resolved reflectance spectroscopy in turbid tissues," *IEEE T. Bio.-Med. Eng.* **36**, 1155–1161 (1989).

83. S. L. Jacques, "Time resolved propagation of ultrashort laser-pulses within turbid tissues," *Appl. Opt.* **28**, 2223–2229 (1989).

84. B. Chance, S. Nioka, J. Kent, K. Mccully, M. Fountain, R. Greenfeld, and G. Holtom, "Time-resolved spectroscopy of hemoglobin and myoglobin in resting and ischemic muscle," *Anal. Biochem.* **174**, 698–707 (1988).

85. B. Chance, J. S. Leigh, H. Miyake, D. S. Smith, S. Nioka, R. Greenfeld, M. Finander, K. Kaufmann, W. Levy, M. Young, P. Cohen, H. Yoshioka, and R. Boretsky, "Comparison of time-resolved and time-unresolved measurements of deoxyhemoglobin in brain," *P. Natl. Acad. Sci. USA* **85**, 4971–4975 (1988).

86. S. Andersson-Engels, R. Berg, S. Svanberg, and O. Jarlman, "Time-resolved transillumination for medical diagnostics," *Opt. Lett.* **15**, 1179–1181 (1990).

87. E. M. Sevick, B. Chance, J. Leigh, S. Nioka, and M. Maris, "Quantitation of time-resolved and frequency-resolved optical-spectra for the determination of tissue oxygenation," *Anal. Biochem.* **195**, 330–351 (1991).

88. B. C. Wilson, E. M. Sevick, M. S. Patterson, and B. Chance, "Time-dependent optical spectroscopy and imaging for biomedical applications," *P. IEEE* **80**, 918–930 (1992).

89. D. T. Delpy and M. Cope, "Quantification in tissue near-infrared spectroscopy," *Philos. T. R. Soc. B* **352**, 649–659 (1997).

90. J. C. Hebden, S. R. Arridge, and D. T. Delpy, "Optical imaging in medicine. 1. Experimental techniques," *Phys. Med. Biol.* **42**, 825–840 (1997).

91. M. Essenpreis, C. E. Elwell, M. Cope, P. Vanderzee, S. R. Arridge, and D. T. Delpy, "Spectral dependence of temporal point spread functions in human tissues," *Appl. Opt.* **32**, 418–425 (1993).

92. S. J. Matcher, M. Cope, and D. T. Delpy, "In vivo measurements of the wavelength dependence of tissue-scattering coefficients between 760 and 900 nm measured with time-resolved spectroscopy," *Appl. Opt.* **36**, 386–396 (1997).

93. J. M. Dudley, G. Genty, and S. Coen, "Supercontinuum generation in photonic crystal fiber," *Rev. Mod. Phys.* **78**, 1135–1184 (2006).

94. C. Abrahamsson, T. Svensson, S. Svanberg, S. Andersson-Engels, J. Johansson, and S. Folestad, "Time and wavelength resolved spectroscopy of turbid media using light continuum generated in a crystal fiber," *Opt. Exp.* **12**, 4103–4112 (2004).

95. T. Svensson, E. Alerstam, D. Khoptyar, J. Johansson, S. Folestad, and S. Andersson-Engels, "Near-infrared photon time-of-flight spectroscopy of turbid materials up to 1400 nm," *Rev. Sci. Instrum.* **80**, 063105 (2009).

96. D. V. O'Connor and D. Phillips, *Time-Correlated Single Photon Counting* (Academic Press, London, Orlando, 1984).

97. W. Becker, *Advanced Time-Correlated Single Photon Counting Techniques*, Chemical Physics (Springer, Verlag, Berlin, Heidelberg, 2005).

98. C. V. Zint, W. Uhring, M. Torregrossa, B. Cunin, and P. Poulet, "Streak camera: A multidetector for diffuse optical tomography," *Appl. Opt.* **42**, 3313–3320 (2003).

99. J. Link, "Measurement of radiative lifetimes of first excited states of Na, K, Rb, and Cs by means of phase-shift method," *J. Opt. Soc. Am.* **56**, 1195–1199 (1966).

100. G. Jönsson, C. Levinson, and S. Svanberg, "Natural radiative lifetimes and Stark-shift parameters in the $4p^2$ configuration in Ca I," *Phys. Scripta* **30**, 65–69 (1984).

101. J. R. Lakowicz and B. P. Maliwal, "Construction and performance of a variable-frequency phase-modulation fluorometer," *Biophys. Chem.* **21**, 61–78 (1985).

102. J. R. Lakowicz and K. Berndt, "Frequency-domain measurements of photon migration in tissues," *Chem. Phys. Lett.* **166**, 246–252 (1990).

103. B. Chance, M. Maris, J. Sorge, and M. Z. Zhang, "Phase modulation system for dual wavelength difference spectroscopy of hemoglobin deoxygenation in tissues," in Proceedings of SPIE Time-Resolved Laser Spectroscopy in Biochemistry II, vol. 1204, pp. 481–491 (1990).

104. M. S. Patterson, J. D. Moulton, B. C. Wilson, K. W. Berndt, and J. R. Lakowicz, "Frequency-domain reflectance for the determination of the scattering and absorption properties of tissue," *Appl. Opt.* **30**, 4474–4476 (1991).

105. T. Durduran, R. Choe, J. P. Culver, L. Zubkov, M. J. Holboke, J. Giammarco, B. Chance, and A. G. Yodh, "Bulk optical properties of healthy female breast tissue," *Phys. Med. Biol.* **47**, 2847–2861 (2002).

106. J. Zhao, H. S. Ding, X. L. Hou, C. Le Zhou, and B. Chance, "In vivo determination of the optical properties of infant brain using frequency-domain near-infrared spectroscopy," *J. Biomed. Opt.* **10**, 024028 (2005).

107. T. Durduran, G. Q. Yu, M. G. Burnett, J. A. Detre, J. H. Greenberg, J. J. Wang, C. Zhou, and A. G. Yodh, "Diffuse optical measurement of blood flow, blood oxygenation, and metabolism in a human brain during sensorimotor cortex activation," *Opt. Lett.* **29**, 1766–1768 (2004).

108. B. J. Tromberg, N. Shah, R. Lanning, A. Cerussi, J. Espinoza, T. Pham, L. Svaasand, and J. Butler, "Non-invasive in vivo characterization of breast tumors using photon migration spectroscopy," *Neoplasia* **2**, 26–40 (2000).

109. N. Shah, A. Cerussi, C. Eker, J. Espinoza, J. Butler, J. Fishkin, R. Hornung, and B. Tromberg, "Noninvasive functional optical spectroscopy of human breast tissue," *P. Natl. Acad. Sci. USA* **98**, 4420–4425 (2001).

110. A. Cerussi, N. Shah, D. Hsiang, A. Durkin, J. Butler, and B. J. Tromberg, "In vivo absorption, scattering, and physiologic properties of 58 malignant breast tumors determined by broadband diffuse optical spectroscopy," *J. Biomed. Opt.* **11**, 044005 (2006).

111. B. J. Tromberg, B. W. Pogue, K. D. Paulsen, A. G. Yodh, D. A. Boas, and A. E. Cerussi, "Assessing the future of diffuse optical imaging technologies for breast cancer management," *Med. Phys.* **35**, 2443–2451 (2008).

112. H. B. Jiang, K. D. Paulsen, U. L. Osterberg, and M. S. Patterson, "Frequency-domain optical image reconstruction in turbid media: An experimental study of single-target detectability," *Appl. Opt.* **36**, 2995–2996 (1997).

113. M. A. Franceschini, K. T. Moesta, S. Fantini, G. Gaida, E. Gratton, H. Jess, W. W. Mantulin, M. Seeber, P. M. Schlag, and M. Kaschke, "Frequency-domain techniques enhance optical mammography: Initial clinical results," *P. Natl. Acad. Sci. USA* **94**, 6468–6473 (1997).

114. S. A. Walker, S. Fantini, and E. Gratton, "Image reconstruction by backprojection from frequency-domain optical measurements in highly scattering media," *Appl. Opt.* **36**, 170–179 (1997).

115. D. M. Hueber, M. A. Franceschini, H. Y. Ma, Q. Zhang, J. R. Ballesteros, S. Fantini, D. Wallace, V. Ntziachristos, and B. Chance, "Non-invasive and quantitative near-infrared haemoglobin spectrometry in the piglet brain during hypoxic stress, using a frequency-domain multidistance instrument," *Phys. Med. Biol.* **46**, 41–62 (2001).

116. J. P. Culver, R. Choe, M. J. Holboke, L. Zubkov, T. Durduran, A. Slemp, V. Ntziachristos, B. Chance, and A. G. Yodh, "Three-dimensional diffuse optical tomography in the parallel plane transmission geometry: Evaluation of a hybrid frequency domain/continuous wave clinical system for breast imaging," *Med. Phys.* **30**, 235–247 (2003).

117. H. Dehghani, B. W. Pogue, S. P. Poplack, and K. D. Paulsen, "Multiwavelength three-dimensional near-infrared tomography of the breast: Initial simulation, phantom, and clinical results," *Appl. Opt.* **42**, 135–145 (2003).

118. A. H. Hielscher, "Optical tomographic imaging of small animals," *Curr. Opin. Biotech.* **16**, 79–88 (2005).

119. D. Contini, L. Zucchelli, L. Spinelli, M. Caffini, R. Re, A. Pifferi, R. Cubeddu, and A. Torricelli, "Brain and muscle near infrared spectroscopy/imaging techniques," *Journal of Near Infrared Spectroscopy* **20**, 15–27 (2012).

120. S. J. Erickson and A. Godavarty, "Hand-held based near-infrared optical imaging devices: A review," *Med. Eng. Phys.* **31**, 495–509 (2009).

121. S. J. Erickson, A. Godavarty, S. L. Martinez, J. Gonzalez, A. Romero, M. Roman, A. Nunez, J. J. Ge, S. Regalado, R. Kiszonas, and C. Lopez-Penalver, "Hand-held optical devices for breast cancer: Spectroscopy and 3-d tomographic imaging," *IEEE J. Sel. Top. Quant.* **18**, 1298–1312 (2012).

122. B. Chance, M. Cope, E. Gratton, N. Ramanujam, and B. Tromberg, "Phase measurement of light absorption and scatter in human tissue," *Rev. Sci. Instrum.* **69**, 3457–3481 (1998).

123. Y. S. Yang, H. L. Liu, X. D. Li, and B. Chance, "Low-cost frequency-domain photon migration instrument for tissue spectroscopy, oximetry, and imaging," *Opt. Eng.* **36**, 1562–1569 (1997).

124. G. Q. Yu, T. Durduran, D. Furuya, J. H. Greenberg, and A. G. Yodh, "Frequency-domain multiplexing system for in vivo diffuse light measurements of rapid cerebral hemodynamics," *Appl. Opt.* **42**, 2931–2939 (2003).

125. D. Roblyer, T. D. O'Sullivan, R. V. Warren, and B. J. Tromberg, "Feasibility of direct digital sampling for diffuse optical frequency domain spectroscopy in tissue," *Meas. Sci. Technol.* **24** (2013).

126. K. S. No and P. H. Chou, "Mini-FDPM and heterodyne mini-FDPM: Handheld non-invasive breast cancer detectors based on frequency-domain photon migration," *IEEE T. Circuits-I* **52**, 2672–2685 (2005).

127. B. Chance, E. Anday, S. Nioka, S. Zhou, L. Hong, K. Worden, C. Li, T. Murray, Y. Ovetsky, D. Pidikiti, and R. Thomas, "A novel method for fast imaging of brain function, non-invasively, with light," *Opt. Exp.* **2**, 411–423 (1998).

128. N. Ramanujam, C. Du, H. Y. Ma, and B. Chance, "Sources of phase noise in homodyne and heterodyne phase modulation devices used for tissue oximetry studies," *Rev. Sci. Instrum.* **69**, 3042–3054 (1998).

129. A. Muller, R. Lumry, and H. Kokubun, "High performance phase fluorometer constructed from commercial subunits," *Rev. Sci. Instrum.* **36**, 1214–1226 (1965).

130. K. Alford and Y. Wickramasinghe, "Phase-amplitude crosstalk in intensity modulated near infrared spectroscopy," *Rev. Sci. Instrum.* **71**, 2191–2195 (2000).

131. S. P. Morgan and K. Y. Yong, "Elimination of amplitude-phase crosstalk in frequency domain near-infrared spectroscopy," *Rev. Sci. Instrum.* **72**, 1984–1987 (2001).

132. *Photomultiplier Tubes: Basics and Applications* (Hamamastu Photonics K. K., 2006), 3rd ed.

133. E. V. Appleton and M. A. F. Barnett, "On some direct evidence for downward atmospheric reflection of electric rays." *P. R. Soc. Lond. A-Conta.* **109**, 621–641 (1925).

134. D. Keep, "Frequency-modulation radar for use in the mercantile marine," in Radio and Telecommunication Section 7th, vol. 103B, pp. 519–523 (1955).

135. A. Hymans and J. Lait, "Analysis of a frequency-modulated continuous-wave ranging system," in Proceedings of the IEEE - Part B: Electronic and Communication Engineering, vol. 107, pp. 365–372 (1960).

136. P. E. Pace, *FMCW Radar*, p. 857 (Artech House, Boston, 2009), 2nd ed.

137. N. Metje, P. R. Atkins, M. J. Brennan, D. N. Chapman, H. M. Lim, J. Machell, J. M. Muggleton, S. Pennock, J. Ratcliffe, M. Redfern, C. D. F. Rogers, A. J. Saul, Q. Shan, S. Swingler, and A. M. Thomas, "Mapping the underworld - State-of-the-art review," *Tunn. Undergr. Sp. Tech.* **22**, 568–586 (2007).

138. E. Widzyk-Capehart, G. Brooker, S. Scheding, R. Hennessy, A. Maclean, and C. Lobsey, "Application of millimetre wave radar sensor to environment mapping in surface mining," in Proceedings of 9th International Conference on Control, Automation, Robotics and Vision, vol. 1-5, pp. 1894–1899 (2006).

139. K. B. Cooper, R. J. Dengler, G. Chattopadhyay, E. Schlecht, J. Gill, A. Skalare, I. Mehdi, and P. H. Siegel, "A high-resolution imaging radar at 580 GHz," *IEEE Microw. Wirel. Co.* **18**, 64–66 (2008).

140. H. P. Marshall and G. Koh, "FMCW radars for snow research," *Cold Reg. Sci. Technol.* **52**, 118–131 (2008).

141. A. Lundberg, N. Granlund, and D. Gustafsson, "Towards automated 'ground truth' snow measurements – A review of operational and new measurement methods for Sweden, Norway, and Finland," *Hydrol. Process.* **24**, 1955–1970 (2010).

142. M. Vossiek, L. Wiebking, P. Gulden, J. Wieghardt, C. Hoffmann, and P. Heide, "Wireless local positioning," *IEEE Microwave Magazine* **4**, 77–86 (2003).

143. F. Ellinger, R. Eickhoff, R. Gierlich, J. Huttner, A. Ziroff, S. Wehrli, T. Ussmuller, J. Carls, V. Subramanian, M. Kremar, R. Mosshammer, S. Spiegel, D. Doumenis, A. Kounoudes, K. Kurek, Y. Yashchyshyn, C. B. Papadias, P. Tragas, A. Kalis, and E. Avatagelou, "Local positioning for wireless sensor networks," in Proceedings of IEEE Globecom Workshops, pp. 388–393 (2007).

144. R. Sorrentino, E. Sbarra, L. Urbani, S. Montori, R. V. Gatti, and L. Marcaccioli, "Accurate FMCW radar-based indoor localization system," in 2012 IEEE International Conference on RFID-Technologies and Applications (RFID-TA), pp. 362–368 (2012).

145. D. A. Jackson, A. D. Kersey, M. Corke, and J. D. C. Jones, "Pseudo-heterodyne detection scheme for optical interferometers," *Electron. Lett.* **18**, 1081–1083 (1982).

146. I. P. Giles, D. Uttam, B. Culshaw, and D. E. N. Davies, "Coherent optical-fibre sensors with modulated laser sources," *Electron. Lett.* **19**, 14–15 (1983).

147. L. Rovati, U. Minoni, and F. Docchio, "Dispersive white light combined with a frequency-modulated continuous-wave interferometer for high-resolution absolute measurements of distance," *Opt. Lett.* **22**, 850–852 (1997).

148. B. Journet and G. Bazin, "A low-cost laser range finder based on an FMCW-like method," *IEEE T. Instrum. Meas.* **49**, 840–843 (2000).

149. R. Schneider, P. Thurmel, and M. Stockmann, "Distance measurement of moving objects by frequency modulated laser radar," *Opt. Eng.* **40**, 33–37 (2001).

150. Z. W. Barber, W. R. Babbitt, B. Kaylor, R. R. Reibel, and P. A. Roos, "Accuracy of active chirp linearization for broadband frequency modulated continuous wave ladar," *Appl. Opt.* **49**, 213–219 (2010).

151. B. I. Erkmen, Z. W. Barber, and J. Dahl, "Maximum-likelihood estimation for frequency-modulated continuous-wave laser ranging using photon-counting detectors," *Appl. Opt.* **52**, 2008–2018 (2013).

152. P. Nerin, P. Besesty, P. Labeye, P. Puget, and G. Chartier, "Absolute distance and velocity measurements by the FMCW technique and self-mixing interference effect inside a single-mode Nd: YAG-$LiTaO_3$ microchip laser," *J. Opt.* **29**, 162–167 (1998).

153. S. Gao, M. O'Sullivan, and R. Q. Hui, "Complex-optical-field lidar system for range and vector velocity measurement," *Opt. Exp.* **20**, 25867–25875 (2012).

154. A. J. Rogers, "Distributed optical-fibre sensors for the measurement of pressure, strain and temperature," *Phys. Rep.* **169**, 99–143 (1988).

155. G. Zheng, M. Campbell, and P. Wallace, "Reflectometric frequency-modulation continuous-wave distributed fiber-optic stress sensor with forward coupled beams," *Appl. Opt.* **35**, 5722–5726 (1996).

156. M. Campbell, G. Zheng, P. A. Wallace, and A. S. HolmesSmith, "A distributed frequency modulation continuous wave fiber stress sensor based on a birefringent Sagnac ring configuration," *Opt. Rev.* **4**, 114–116 (1997).

157. M. Zavrsnik and G. Stewart, "Coherence addressing of quasi-distributed absorption sensors by the FMCW method," *J. Lightwave Technol.* **18**, 57–65 (2000).

158. H. B. Yu, W. Jin, H. L. Ho, K. C. Chan, C. C. Chan, M. S. Demokan, G. Stewart, B. Culshaw, and Y. B. Liao, "Multiplexing of optical fiber gas sensors with a frequency-modulated continuous-wave technique," *Appl. Opt.* **40**, 1011–1020 (2001).

159. F. Ye, L. Qian, and B. Qi, "Multipoint chemical gas sensing using frequency-shifted interferometry," *J. Lightwave Technol.* **27**, 5356–5364 (2009).

160. J. H. Geng, C. Spiegelberg, and S. B. Jiang, "Narrow linewidth fiber laser for 100-km optical frequency domain reflectometry," *Photon. Technol. Lett.* **17**, 1827–1829 (2005).

161. Y. Koshikiya, X. Y. Fan, and F. Ito, "Long range and cm-level spatial resolution measurement using coherent optical frequency domain reflectometry with SSB-SC modulator and narrow linewidth fiber laser," *J. Lightwave Technol.* **26**, 3287–3294 (2008).

162. R. I. Macdonald, "Frequency-domain optical reflectometer," *Appl. Opt.* **20**, 1840–1844 (1981).

163. J. Zheng, *Optical Frequency-Modulated Continuous-Wave (FMCW) Interferometry*, Optical Science (Springer, New York, 2005).

164. Z. Guan, P. Lundin, and S. Svanberg, "Assessment of photon migration in scattering media using heterodyning techniques with a frequency modulated diode laser," *Opt. Exp.* **17**, 16291–16299 (2009).

165. J. Tualle, E. Tinet, and S. Avrillier, "A new and easy way to perform time-resolved measurements of the light scattered by a turbid medium," *Opt. Commun.* **189**, 211–220 (2001).

166. J. M. Tualle, H. L. Nghiem, C. Schafauer, P. Berthaud, E. Tinet, D. Ettori, and S. Avrillier, "Time-resolved measurements from speckle interferometry," *Opt. Lett.* **30**, 50–52 (2005).

167. M. Cheikh, H. L. Nghiem, D. Ettori, E. Tinet, S. Avrillier, and J. M. Tualle, "Time-resolved diffusing wave spectroscopy applied to dynamic heterogeneity imaging," *Opt. Lett.* **31**, 2311–2313 (2006).

168. J. M. Tualle, H. L. Nghiem, M. Cheikh, D. Ettori, E. Tinet, and S. Avrillier, "Time-resolved diffusing wave spectroscopy beyond 300 transport mean free paths," *J. Opt. Soc. Am. A* **23**, 1452–1457 (2006).

169. K. Zarychta, E. Tinet, L. Azizi, S. Avrillier, D. Ettori, and J. M. Tualle, "Time-resolved diffusing wave spectroscopy with a CCD camera," *Opt. Exp.* **18**, 16289–16301 (2010).

170. J. Zheng, "Coherence analysis of optical frequency-modulated continuous-wave interference," *Appl. Opt.* **45**, 3681–3687 (2006).

171. K. Dorschel and G. Müller, "Velocity resolved laser Doppler blood flow measurements in skin," *Flow Meas. Instrum.* **7**, 257–264 (1996).

172. I. Fredriksson, *Quantitative Laser Doppler Flowmetry*, Ph.D. thesis, Linkping University (2009).

173. S. G. Anema and Y. M. Li, "Association of denatured whey proteins with casein micelles in heated reconstituted skim milk and its effect on casein micelle size," *J. Dairy Res.* **70**, 73–83 (2003).

174. R. C. Murdock, L. Braydich-Stolle, A. M. Schrand, J. J. Schlager, and S. M. Hussain, "Characterization of nanomaterial dispersion in solution prior to in vitro exposure using dynamic light scattering technique," *Toxicol. Sci.* **101**, 239–253 (2008).

175. M. Berka and J. A. Rice, "Absolute aggregation rate constants in aggregation of kaolinite measured by simultaneous static and dynamic light scattering," *Langmuir* **20**, 6152–6157 (2004).

176. T. Matsunaga and M. Shibayama, "Gel point determination of gelatin hydrogels by dynamic light scattering and rheological measurements," *Phys. Rev. E.* **76**, 030401 (2007).

177. G. Maret and P. E. Wolf, "Multiple light-scattering from disordered media – The effect of Brownian-motion of scatterers," *Z. Phys. B Con. Mat.* **65**, 409–413 (1987).

178. D. J. Pine, D. A. Weitz, P. M. Chaikin, and E. Herbolzheimer, "Diffusing-wave spectroscopy," *Phys. Rev. Lett.* **60**, 1134–1137 (1988).

179. G. Maret, "Diffusing-wave spectroscopy," *Curr. Opin. Colloid In.* **2**, 251–257 (1997).

180. R. Carminati, R. Elaloufi, and J. J. Greffet, "Beyond the diffusing-wave spectroscopy model for the temporal fluctuations of scattered light," *Phys. Rev. Lett.* **92**, 213903 (2004).

181. T. Durduran and A. G. Yodh, "Diffuse correlation spectroscopy for non-invasive, micro-vascular cerebral blood flow measurement," *Neuroimage* **85**, 51–63 (2014).

182. D. J. Pine, D. A. Weitz, J. X. Zhu, and E. Herbolzheimer, "Diffusing-wave spectroscopy – Dynamic light-scattering in the multiple-scattering limit," *J. Phys.-Paris* **51**, 2101–2127 (1990).

183. F. Jaillon, J. Li, G. Dietsche, T. Elbert, and T. Gisler, "Activity of the human visual cortex measured non-invasively by diffusing-wave spectroscopy," *Opt. Exp.* **15**, 6643–6650 (2007).

184. J. Galvan-Miyoshi, J. Delgado, and R. Castillo, "Diffusing wave spectroscopy in Maxwellian fluids," *Eur. Phys. J. E* **26**, 369–377 (2008).

185. Z. Gaygadzhiev, M. Alexander, and M. Corredig, "Sodium caseinate-stabilized fat globules inhibition of the rennet-induced gelation of casein micelles studied by diffusing wave spectroscopy," *Food Hydrocolloid.* **23**, 1134–1138 (2009).

186. A. M. Zysk, F. T. Nguyen, A. L. Oldenburg, D. L. Marks, and S. A. Boppart, "Optical coherence tomography: A review of clinical development from bench to bedside," *J. Biomed. Opt.* **12**, 051403 (2007).

187. D. D. Nolte, *Optical Interferometry for Biology and Medicine*, Bioanalysis (Springer, New York, 2011).

188. K. K. Bizheva, A. M. Siegel, and D. A. Boas, "Path-length-resolved dynamic light scattering in highly scattering random media: The transition to diffusing wave spectroscopy," *Phys. Rev. E* **58**, 7664–7667 (1998).

189. A. Wax, C. H. Yang, R. R. Dasari, and M. S. Feld, "Path-length-resolved dynamic light scattering: Modeling the transition from single to diffusive scattering," *Appl. Opt.* **40**, 4222–4227 (2001).

190. B. Varghese, V. Rajan, T. van Leeuwen, and W. Steenbergen, "Quantification of optical Doppler broadening and optical path lengths of multiply scattered light by phase modulated low coherence interferometry," *Opt. Exp.* **15**, 9157–9165 (2007).

191. J. G. Fujimoto, "Optical coherence tomography for ultrahigh resolution in vivo imaging," *Nat. Biotechnol.* **21**, 1361–1367 (2003).

192. M. C. Amann, T. Bosch, M. Lescure, R. Myllyla, and M. Rioux, "Laser ranging: A critical review of usual techniques for distance measurement," *Opt. Eng.* **40**, 10–19 (2001).

193. C. Dyroff, *Tunable Diode-Laser Absorption Spectroscopy for Trace-Gas Measurements with High Sensitivity and Low Drift* (KIT Scientific Publishing, 2010).

194. J. F. Butler, R. H. Rediker, A. R. Calawa, T. C. Harman, R. J. Phelan, and A. J. Strauss, "PbTe diode laser," *Appl. Phys. Lett.* **5**, 75–77 (1964).

195. E. D. Hinkley, "High-resolution infrared spectroscopy with a tunable diode laser," *Appl. Phys. Lett.* **16**, 351–354 (1970).

196. F. K. Tittel, D. Richter, and A. Fried, *Mid-infrared laser applications in spectroscopy*, vol. 89, pp. 445–510 (2003).

197. E. D. Hinkley, "Laser spectroscopic instrumentation and techniques - long-path monitoring by resonance-absorption," *Opt. Quant. Electron.* **8**, 155–167 (1976).

198. R. S. Eng, J. F. Butler, and K. J. Linden, "Tunable diode-laser spectroscopy - An invited review," *Opt. Eng.* **19**, 945–960 (1980).

199. E. D. Hinkley and P. L. Kelley, "Detection of air pollutants with tunable diode lasers," *Science* **171**, 635–639 (1971).

200. L. B. Kreuzer, "Ultralow gas concentration infrared absorption spectroscopy," *J. Appl. Phys.* **42**, 2934–2943 (1971).

201. K. W. Nill, F. A. Blum, A. R. Calawa, and T. C. Harman, "Infrared spectroscopy of CO using a tunable PbSSe diode laser," *Appl. Phys. Lett.* **19**, 79–81 (1971).

202. R. T. Ku, E. D. Hinkley, and J. O. Sample, "Long-path monitoring of atmospheric carbon-monoxide with a tunable diode laser system," *Appl. Opt.* **14**, 854–861 (1975).

203. E. Hinkley, A. Calawa, P. Kelley, and S. Clough, "Tunable laser spectroscopy of the v_1 band of SO_2," *J. Appl. Phys.* **43**, 3222 (1972).

204. K. W. Nill, A. J. Strauss, and F. A. Blum, "Tunable CW $Pb_{0.98}Cd_{0.02}S$ diode lasers emitting at 3.5 μm - Applications to ultrahigh-resolution spectroscopy," *Appl. Phys. Lett.* **22**, 677–679 (1973).

205. R. S. Eng, P. L. Kelley, A. R. Calawa, T. C. Harman, and K. W. Nill, "Tunable diode laser measurements of water-vapor absorption-line parameters," *Mol. Phys.* **28**, 653–664 (1974).

206. R. F. Curl and F. K. Tittel, "Tunable infrared laser spectroscopy," *Annu. Rep. Prog. Chem., Sect. C* **98**, 219–272 (2002).

207. P. Werle, F. Slemr, K. Maurer, R. Kormann, R. Mucke, and B. Janker, "Near- and mid-infrared laser-optical sensors for gas analysis," *Opt. Laser Eng.* **37**, 101–114 (2002).

208. H. Preier, "Recent advances in lead-chalcogenide diode-lasers," *Appl. Phys.* **20**, 189–206 (1979).

209. J. A. Silver and A. C. Stanton, "Airborne measurements of humidity using a single-mode Pb salt diode-laser," *Appl. Opt.* **26**, 2558–2566 (1987).

210. D. E. Cooper and C. B. Carlisle, "High-sensitivity FM spectroscopy with a lead-salt diode-laser," *Opt. Lett.* **13**, 719–721 (1988).

211. M. Tacke, "New developments and application of tunable IR lead salt lasers," *Infrared Phys. Techn.* **36**, 447–463 (1995).

212. Z. Feit, P. Mak, R. Woods, and M. McDonald, "MBE grown buried heterostructure separate confinement multiple quantum well $Pb_{0.9854}Eu_{0.014}Se_xTe_{1-x}/Pb_{0.981}Sn_{0.019}Te$ tunable diode lasers for high resolution spectroscopy," *Spectrochim. Acta A* **52**, 851–855 (1996).

213. M. Hodges and U. P. Schiessl, "Lead salt tunable diode lasers: Key devices for high sensitivity gas analysis," in In-Plane Semiconductor Lasers III, vol. 3628, pp. 113–121 (1999).

214. J. Faist, F. Capasso, C. Sirtori, D. L. Sivco, J. N. Baillargeon, A. L. Hutchinson, S. N. G. Chu, and A. Y. Cho, "High power mid-infrared (λ greater than or similar to-5 μm) quantum cascade lasers operating above room temperature," *Appl. Phys. Lett.* **68**, 3680–3682 (1996).

215. Y. Yao, A. J. Hoffman, and C. F. Gmachl, "Mid-infrared quantum cascade lasers," *Nat. Photonics* **6**, 432–439 (2012).

216. J. Faist, F. Capasso, D. L. Sivco, C. Sirtori, A. L. Hutchinson, and A. Y. Cho, "Quantum cascade laser," *Science* **264**, 553–556 (1994).

217. C. Gmachl, F. Capasso, D. L. Sivco, and A. Y. Cho, "Recent progress in quantum cascade lasers and applications," *Rep. Prog. Phys.* **64**, 1533–1601 (2001).

218. F. K. Tittel, Y. Bakhirkin, A. Kosterev, R. Lewicki, S. So, G. Wysocki, and R. F. Curl, "Recent advances and applications of mid-infrared based trace gas sensor technology," in Quantum Sensing and Nanophotonic Devices V, vol. 6900, pp. Z9000–Z9000 (2008).

219. M. Ohtsu, H. Kotani, and H. Tagawa, "Spectral measurements of NH_3 and H_2O for pollutant gas monitoring by 1.5-μm InGaAsP/InP lasers," *Jpn. J. Appl. Phys. 1* **22**, 1553–1557 (1983).

220. K. Fukuoka, M. Ohtsu, and T. Tako, "Accurate wavelength measurements of the absorption-lines in H_2O vapor by a 0.8 μm AlGaAs laser," *Jpn. J. Appl. Phys. 2* **23**, L117–L120 (1984).

221. H. Sasada, "Stark-modulation spectroscopy of NH_3 with a 1.23-μm semiconductor-laser," *Opt. Lett.* **9**, 448–450 (1984).

222. T. Gustavsson and H. Martin, "Low-cost high-resolution laser spectrometer system in the near-infrared region using a GaAlAs diode-laser," *Rev. Sci. Instrum.* **57**, 1132–1134 (1986).

223. D. T. Cassidy and L. J. Bonnell, "Trace gas-detection with short-external-cavity ingaasp diode-laser transmitter modules operating at 1.58 μm," *Appl. Opt.* **27**, 2688–2693 (1988).

224. P. A. Martin, "Near-infrared diode laser spectroscopy in chemical process and environmental air monitoring," *Chem. Soc. Rev.* **31**, 201–210 (2002).

225. M. Lackner, "Tunable diode laser absorption spectroscopy (TDLAS) in the process industries – A review," *Reviews in Chemical Engineering* **23**, 65–147 (2007).

226. S. Schilt, L. Thevenaz, and P. Robert, "Wavelength modulation spectroscopy: Combined frequency and intensity laser modulation," *Appl. Opt.* **42**, 6728–6738 (2003).

227. J. M. Supplee, E. A. Whittaker, and W. Lenth, "Theoretical description of frequency-modulation and wavelength modulation spectroscopy," *Appl. Opt.* **33**, 6294–6302 (1994).

228. G. Litfin, C. R. Pollock, R. F. Curl, and F. K. Tittel, "Sensitivity enhancement of laser-absorption spectroscopy by magnetic rotation effect," *J. Chem. Phys.* **72**, 6602–6605 (1980).

229. G. Berden, R. Peeters, and G. Meijer, "Cavity ring-down spectroscopy: Experimental schemes and applications," *Int. Rev. Phys. Chem.* **19**, 565–607 (2000).

230. R. Engeln, G. Berden, R. Peeters, and G. Meijer, "Cavity enhanced absorption and cavity enhanced magnetic rotation spectroscopy," *Rev. Sci. Instrum.* **69**, 3763–3769 (1998).

231. A. O'Keefe, "Integrated cavity output analysis of ultra-weak absorption," *Chem. Phys. Lett.* **293**, 331–336 (1998).

232. M. W. Sigrist, "Laser generation of acoustic-waves in liquids and gases," *J. Appl. Phys.* **60**, R83–R121 (1986).

233. M. W. Sigrist, S. Bernegger, and P. L. Meyer, "Infrared-laser photoacoustic-spectroscopy," *Infrared Phys* **29**, 805–814 (1989).

234. M. W. Sigrist, *Air monitoring by spectroscopic techniques*, Chemical Analysis (Wiley, New York, 1994).

235. P. Werle, "A review of recent advances in semiconductor laser based gas monitors," *Spectrochim. Acta A* **54**, 197–236 (1998).

236. D. S. Baer, J. B. Paul, J. B. Gupta, and A. O'Keefe, "Sensitive absorption measurements in the near-infrared region using off-axis integrated-cavity-output spectroscopy," *Appl. Phys. B* **75**, 261–265 (2002).

237. J. S. Li, X. M. Gao, W. Z. Li, Z. S. Cao, L. H. Deng, W. X. Zhao, M. Q. Huang, and W. J. Zhang, "Near-infrared diode laser wavelength modulation-based photoacoustic spectrometer," *Spectrochim. Acta A* **64**, 338–342 (2006).

238. W. Zhao, X. Gao, W. Chen, W. Zhang, T. Huang, T. Wu, and H. Cha, "Wavelength modulated off-axis integrated cavity output spectroscopy in the near infrared," *Appl. Phys. B* **86**, 353–359 (2007).

239. K. Liu, J. Li, L. Wang, T. Tan, W. Zhang, X. Gao, W. Chen, and F. K. Tittel, "Trace gas sensor based on quartz tuning fork enhanced laser photoacoustic spectroscopy," *Appl. Phys. B* **94**, 527–533 (2009).

240. Y. A. Bakhirkin, A. A. Kosterev, C. Roller, R. F. Curl, and F. K. Tittel, "Mid-infrared quantum cascade laser based off-axis integrated cavity output spectroscopy for biogenic nitric oxide detection," *Appl. Opt.* **43**, 2257–2266 (2004).

241. R. Lewicki, A. A. Kosterev, D. M. Thomazy, T. H. Risby, S. Solga, T. B. Schwartz, and F. K. Tittel, "Real time ammonia detection in exhaled human breath using a distributed feedback quantum cascade laser based sensor," in Proceedings of SPIE Quantum Sensing and Nanophotonic Devices VIII, vol. 7945, p. 79450K (2011).

242. G. N. Rao and A. Karpf, "External cavity tunable quantum cascade lasers and their applications to trace gas monitoring," *Appl. Opt.* **50**, A100–A115 (2011).

243. F. K. Tittel and R. Lewicki, *Tunable Mid-Infrared Laser Absorption Spectroscopy* (Woodhead Publishing Limited, 2013).

244. K. S. Song and E. C. Jung, "Recent developments in modulation spectroscopy for trace gas detection using tunable diode lasers," *Appl. Spectrosc. Rev.* **38**, 395–432 (2003).

245. M. W. Sigrist, "Trace gas monitoring by laser photoacoustic spectroscopy and related techniques," *Rev. Sci. Instrum.* **74**, 486–490 (2003).

246. J. M. Rey and M. W. Sigrist, "New differential mode excitation photoacoustic scheme for near-infrared water vapour sensing," *Sensor. Actuat. B-Chem.* **135**, 161–165 (2008).

247. A. Elia, P. M. Lugara, C. Di Franco, and V. Spagnolo, "Photoacoustic techniques for trace gas sensing based on semiconductor laser sources," *Sensors-Basel* **9**, 9616–9628 (2009).

248. B. Zoltan, P. Andrea, and S. Gabor, "Photoacoustic instruments for practical applications: Present, potentials, and future challenges," *Appl. Spectrosc. Rev.* **46**, 1–37 (2011).

249. B. A. Paldus and A. A. Kachanov, "An historical overview of cavity-enhanced methods," *Can. J. Phys.* **83**, 975–999 (2005).

250. J. Ye, L. S. Ma, and J. L. Hall, "Ultrasensitive detections in atomic and molecular physics: Demonstration in molecular overtone spectroscopy," *J. Opt. Soc. Am. B* **15**, 6–15 (1998).

251. A. Foltynowicz, F. M. Schmidt, W. Ma, and O. Axner, "Noise-immune cavity-enhanced optical heterodyne molecular spectroscopy: Current status and future potential," *Appl. Phys. B* **92**, 313–326 (2008).

252. X. J. Cui, C. Lengignon, T. Wu, W. X. Zhao, G. Wysocki, E. Fertein, C. Coeur, A. Cassez, L. Croize, W. D. Chen, Y. J. Wang, W. J. Zhang, X. M. Gao, W. Q. Liu, Y. J. Zhang, and F. Z. Dong, "Photonic sensing of the atmosphere by absorption spectroscopy," *J. Quant. Spectrosc. Rad. Transf.* **113**, 1300–1316 (2012).

253. J. Ropcke, G. Lombardi, A. Rousseau, and P. B. Davies, "Application of mid-infrared tuneable diode laser absorption spectroscopy to plasma diagnostics: a review," *Plasma Sources Sci. T.* **15**, S148–S168 (2006).

254. C. J. Wang and P. Sahay, "Breath analysis using laser spectroscopic techniques: Breath biomarkers, spectral fingerprints, and detection limits," *Sensors-Basel* **9**, 8230–8262 (2009).

255. L. S. Rothman, C. P. Rinsland, A. Goldman, S. T. Massie, D. P. Edwards, J. M. Flaud, A. Perrin, C. Camy-Peyret, V. Dana, J. Y. Mandin, J. Schroeder, A. McCann, R. R. Gamache, R. B. Wattson, K. Yoshino, K. V. Chance, K. W. Jucks, L. R. Brown, V. Nemtchinov, and P. Varanasi, "The HITRAN molecular spectroscopic database and HAWKS (HITRAN Atmospheric Workstation): 1996 edition," *J. Quant. Spectrosc. Rad. Transf.* **60**, 665–710 (1998).

256. W. Demtröder, *Laser Spectroscopy Vol. 1: Basic Principles* (Springer-Verlag, Berlin, Heidelberg, 2007).

257. J. H. van Vleck and V. F. Weisskopf, "On the shape of collision-broadened lines," *Rev. Mod. Phys.* **17**, 227–236 (1945).

258. G. W. F. Drake, *Handbooks of Atomic, Molecular, and Optical Physics* (Springer, 2006).

259. J. M. Hartmann, C. Boulet, and D. Robert, *Collisional Effects on Molecular Spectra: Laboratory Experiments and Models, Consequences for Applications* (Elsevier, Oxford, 2008).

260. D. E. Burch, E. B. Singleton, and D. Williams, "Absorption line broadening in the infrared," *Appl. Opt.* **1**, 359–363 (1962).

261. D. E. Burch, D. A. Gryvnak, R. R. Patty, and C. E. Bartky, "Absorption of infrared radiant energy by CO_2 and H_2O. 4. shapes of collision-broadened CO_2 lines," *J. Opt. Soc. Am.* **59**, 267–278 (1969).

262. B. E. Grossmann and E. V. Browell, "Water-vapor line broadening and shifting by air, nitrogen, oxygen, and argon in the 720-nm wavelength region," *J. Mol. Spectrosc.* **138**, 562–595 (1989).

263. A. Ray, A. Bandyopadhyay, B. Ray, D. Biswas, and P. N. Ghosh, "Line-shape study of water vapour by tunable diode laser spectrometer in the 822-832 nm wavelength region," *Appl. Phys. B* **79**, 915–921 (2004).

264. G. Herzberg, *Molecular Spectra and Molecular Structure : Spectra of Diatomic Molecules* (Van Nostrand Reinhold Company, New York, 1950).

265. W. Demtröder, *Atoms,Molecules and Photons: An Introduction to Atomic-, Molecular- and Quantum- Physics* (Springer-Verlag Berlin Heidelberg, 2010).

266. M. G. A. Bernard and G. Duraffourg, "Laser conditions in semiconductors," *Phys. Status Solidi* **1**, 699–703 (1961).

267. N. G. Basov, O. N. Krokhin, and Y. M. Popov, "Production of negative-temperature states in p-n junctions of degenerate semiconductors," *Sov. Phys. JETP-USSR.* **13**, 1320–1321 (1961).

268. R. N. Hall, R. O. Carlson, T. J. Soltys, G. E. Fenner, and J. D. Kingsley, "Coherent light emission from GaAs junctions," *Phys. Rev. Lett.* **9**, 366–368 (1962).

269. M. I. Nathan, W. P. Dumke, G. Burns, F. H. Dill, and G. Lasher, "Stimulated emission of radiation from GaAs p-n junctions," *Appl. Phys. Lett.* **1**, 62–64 (1962).

270. T. M. Quist, R. H. Rediker, R. J. Keyes, W. E. Krag, B. Lax, A. L. Mcwhorter, and H. J. Zeigler, "Semiconductor maser of GaAs," *Appl. Phys. Lett.* **1**, 91–92 (1962).

271. Z. I. Alferov, V. M. Andreev, E. L. Portnoi, and M. K. Trukan, "AlAs-GaAs heterojunction injection lasers with a low room-temperature threshold," *Sov. Phys. Semicond.* **3**, 1107 (1970).

272. I. Hayashi, M. B. Panish, P. W. Foy, and S. Sumski, "Junction lasers which operate continuously at room temperature," *Appl. Phys. Lett.* **17**, 109–111 (1970).

273. T. P. Lee, C. A. Burrus, R. A. Linke, and R. J. Nelson, "Short-cavity single-frequency InGaAsP buried-heterostructure lasers," *Electron. Lett.* **19**, 82–83 (1983).

274. G. P. Agrawal, *Single-Longitudinal-Mode Semiconductor Lasers*, vol. 26 of *Progress in Optics* (Elsevier Science Publishers, 1988).

275. D. Renner and J. E. Carroll, "Analysis of the effect of spontaneous-emission coupling on the number of excited longitudinal modes in semiconductor-lasers," *Electron. Lett.* **14**, 779–781 (1978).

276. T. P. Lee, C. A. Burrus, J. A. Copeland, A. G. Dentai, and D. Marcuse, "Short-cavity InGaAsP injection-lasers – Dependence of mode spectra and single-longitudinal-mode power on cavity length," *IEEE J. Quantum Elect.* **18**, 1101–1113 (1982).

277. S. Wang, "Principles of distributed feedback and distributed Bragg-reflector lasers," *IEEE J. Quantum Elect.* **Qe10**, 413–427 (1974).

278. C. Voumard, "External-cavity-controlled 32-MHz narrow-band CW GaAlAs-diode lasers," *Opt. Lett.* **1**, 61–63 (1977).

279. K. C. Harvey and C. J. Myatt, "External-cavity diode-laser using a grazing-incidence diffraction grating," *Opt. Lett.* **16**, 910–912 (1991).

280. Y. D. Jeong, Y. H. Won, S. O. Choi, and J. H. Yoon, "Tunable single-mode Fabry-Pérot laser diode using a built-in external cavity and its modulation characteristics," *Opt. Lett.* **31**, 2586–2588 (2006).

281. G. Galbács, "A review of applications and experimental improvements related to diode laser atomic spectroscopy," *Appl. Spectrosc. Rev.* **41**, 259–303 (2006).

282. H. Nasim and Y. Jamil, "Recent advancements in spectroscopy using tunable diode lasers," *Laser Phys. Lett.* **10**, 043001 (2013).

283. M. Fukuda, "Optical source reliability in recent optical fiber transmission systems and consumer electronics," *Microelectron. Reliab.* **46**, 263–269 (2006).

284. T. Numai, *Fundamentals of Semiconductor Lasers*, Optical Sciences (Springer, Verlag New York, 2004).

285. C. E. Wieman and L. Hollberg, "Using diode-lasers for atomic physics," *Rev. Sci. Instrum.* **62**, 1–20 (1991).

286. H. Unlu, "A thermodynamic model for determining pressure and temperature effects on the bandgap energies and other properties of some semiconductors," *Solid State Electron* **35**, 1343–1352 (1992).

287. M. Nakamura, K. Aiki, N. Chinone, R. Ito, and J. Umeda, "Longitudinal-mode behaviors of mode-stabilized $Al_xGa_{1-x}As$ injection-lasers," *J. Appl. Phys.* **49**, 4644–4648 (1978).

288. C. H. Henry, R. A. Logan, and K. A. Bertness, "Spectral dependence of the change in refractive-index due to carrier injection in GaAs-lasers," *J. Appl. Phys.* **52**, 4457–4461 (1981).

289. J. Manning, R. Olshansky, and C. B. Su, "The carrier-induced index change in AlGaAs and 1.3 μm InGaAsP diode-lasers," *IEEE J. Quantum Elect.* **19**, 1525–1530 (1983).

290. G. M. Tino, "Atomic spectroscopy with diode-lasers," *Phys. Scripta* **T51**, 58–66 (1994).

291. M. Fukuda, T. Mishima, N. Nakayama, and T. Masuda, "Temperature and current coefficients of lasing wavelength in tunable diode laser spectroscopy," *Appl. Phys. B* **100**, 377–382 (2010).

292. J. E. Carroll, J. Whiteaway, and D. Plumb, *Distributed Feedback Semiconductor Lasers*, IEEE Circuits, Devices and Systems (The Institution of Electrical Engineers: SPIE Optical Engineering Press, London, UK, 1998).

293. O. Ueda, *Materials and Reliability Handbook for Semiconductor Optical and Electron Devices* (Springer, New York, 2012).

294. S. Murata, I. Mito, and K. Kobayashi, "Spectral characteristics for a 1.5 μm DBR laser with frequency-tuning region," *IEEE J. Quantum Elect.* **23**, 835–838 (1987).

295. B. Broberg and S. Nilsson, "Widely tunable active Bragg reflector integrated lasers in InGaAsP-InP," *Appl. Phys. Lett.* **52**, 1285–1287 (1988).

296. S. Murata and I. Mito, "Frequency-tunable semiconductor-lasers," *Opt. Quant. Electron.* **22**, 1–15 (1990).

297. K. Kobayashi, "Single frequency and tunable laser-diodes," *J. Lightwave Technol.* **6**, 1623–1633 (1988).

298. Y. Kotaki and H. Ishikawa, "Wavelength tunable DFB and DBR lasers for coherent optical fiber communications," *IEEE Proceedings-J. Optoelectronics* **138**, 171–177 (1991).

299. V. Jayaraman, D. A. Cohen, and L. A. Coldren, "Demonstration of broad-band tunability in a semiconductor-laser using sampled gratings," *Appl. Phys. Lett.* **60**, 2321–2323 (1992).

300. F. Favre, D. Leguen, J. C. Simon, and B. Landousies, "External-cavity semiconductor-laser with 15-nm continuous tuning range," *Electron. Lett.* **22**, 795–796 (1986).

301. L. Ricci, M. Weidemuller, T. Esslinger, A. Hemmerich, C. Zimmermann, V. Vuletic, W. König, and T. W. Hänsch, "A compact grating-stabilized diode-laser system for atomic physics," *Opt. Commun.* **117**, 541–549 (1995).

302. R. Wyatt and W. J. Devlin, "10-kHz linewidth 1.5 μm InGaAsP external cavity laser with 55-nm tuning range," *Electron. Lett.* **19**, 110–112 (1983).

303. W. Zeller, L. Naehle, P. Fuchs, F. Gerschuetz, L. Hildebrandt, and J. Koeth, "DFB lasers between 760 nm and 16 μm for sensing applications," *Sensors-Basel* **10**, 2492–2510 (2010).

304. W. B. Joyce and R. W. Dixon, "Thermal resistance of heterostructure lasers," *J. Appl. Phys.* **46**, 855–862 (1975).

305. P. Correc, O. Girard, and I. F. Defaria, "On the thermal contribution to the FM response of DFB lasers – Theory and experiment," *IEEE J. Quantum Elect.* **30**, 2485–2490 (1994).

306. E. Marin, I. Camps, M. Sanchez, and P. Diaz, "Thermal resistance of double heterostructure separate confinement GaAs/AlGaAs semiconductor lasers in stripe geometry configuration," *Rev. Mex. Fis.* **42**, 414–424 (1996).

307. J. Vermaak, M. Ranallo, R. Martinelli, R. Menna, and J. Connolly, "Packing techniques to increase wavelength tuning of distributed feedback lasers," in Proceedings of CLEO, vol. CTuA35, pp. 161–162 (2000).

308. M. Gehrtz, G. C. Bjorklund, and E. A. Whittaker, "Quantum-limited laser frequency-modulation spectroscopy," *J. Opt. Soc. Am. B* **2**, 1510–1526 (1985).

309. J. U. White, "Long optical paths of large aperture," *J. Opt. Soc. Am.* **32**, 285–288 (1942).

310. D. Herriott, R. Kompfner, and H. Kogelnik, "Off-axis paths in spherical mirror interferometers," *Appl. Opt.* **3**, 523–526 (1964).

311. J. Hodgkinson, D. Masiyano, and R. Tatam, "Using integrating spheres as absorption cells: Path-length distribution and application of Beer's law," *Appl. Opt.* **48**, 5748–5758 (2009).

312. E. I. Moses and C. L. Tang, "High-sensitivity laser wavelength-modulation spectroscopy," *Opt. Lett.* **1**, 115–117 (1977).

313. G. C. Bjorklund, "Frequency-modulation spectroscopy – New method for measuring weak absorptions and dispersions," *Opt. Lett.* **5**, 15–17 (1980).

314. C. B. Carlisle, D. E. Cooper, and H. Preier, "Quantum noise-limited FM spectroscopy with a lead-salt diode-laser," *Appl. Opt.* **28**, 2567–2576 (1989).

315. D. S. Bomse, A. C. Stanton, and J. A. Silver, "Frequency-modulation and wavelength modulation spectroscopies – Comparison of experimental methods using a lead-salt diode-laser," *Appl. Opt.* **31**, 718–731 (1992).

316. J. A. Silver, "Frequency-modulation spectroscopy for trace species detection - Theory and comparison among experimental methods," *Appl. Opt.* **31**, 707–717 (1992).

317. F. S. Pavone and M. Inguscio, "Frequency-modulation and wavelength-modulation spectroscopies – Comparison of experimental methods using an AlGaaAs diode-laser," *Appl. Phys. B* **56**, 118–122 (1993).

318. P. Kluczynski and O. Axner, "Theoretical description based on Fourier analysis of wavelength-modulation spectrometry in terms of analytical and background signals," *Appl. Opt.* **38**, 5803–5815 (1999).

319. P. Kluczynski, J. Gustafsson, A. M. Lindberg, and O. Axner, "Wavelength modulation absorption spectrometry – An extensive scrutiny of the generation of signals," *Spectrochim. Acta B* **56**, 1277–1354 (2001).

320. T. Fernholz, H. Teichert, and V. Ebert, "Digital, phase-sensitive detection for in situ diode-laser spectroscopy under rapidly changing transmission conditions," *Appl. Phys. B* **75**, 229–236 (2002).

321. H. J. Li, G. B. Rieker, X. Liu, J. B. Jeffries, and R. K. Hanson, "Extension of wavelength-modulation spectroscopy to large modulation depth for diode laser absorption measurements in high-pressure gases," *Appl. Opt.* **45**, 1052–1061 (2006).

322. L. Persson, M. Lewander, M. Andersson, K. Svanberg, and S. Svanberg, "Simultaneous detection of molecular oxygen and water vapor in the tissue optical window using tunable diode laser spectroscopy," *Appl. Opt.* **47**, 2028–2034 (2008).

323. R. L. P. van Veen, H. J. C. M. Sterenborg, A. Pifferi, A. Torricelli, E. Chikoidze, and R. Cubeddu, "Determination of visible near-IR absorption coefficients of mammalian fat using time- and spatially-resolved diffuse reflectance and transmission spectroscopy," *J. Biomed. Opt.* **10**, 054004 (2005).

324. T. Svensson, E. Alerstam, J. Johansson, and S. Andersson-Engels, "Optical porosimetry and investigations of the porosity experienced by light interacting with porous media," *Opt. Lett.* **35**, 1740–1742 (2010).

325. T. Svensson, E. Adolfsson, M. Lewander, C. Xu, and S. Svanberg, "Disordered, strongly scattering porous materials as miniature multipass gas cells," *Phys. Rev. Lett.* **107**, 143901 (2011).

326. X. Lou, C. Xu, S. Svanberg, and G. Somesfalean, "Multimode diode laser correlation spectroscopy using gas-filled porous materials for pathlength enhancement," *Appl. Phys. B* **109**, 453–460 (2012).

327. J. Alnis, B. Anderson, M. Sjöholm, G. Somesfalean, and S. Svanberg, "Laser spectroscopy of free molecular oxygen dispersed in wood materials," *Appl. Phys. B* **77**, 691–695 (2003).

328. M. Andersson, L. Persson, M. Sjöholm, and S. Svanberg, "Spectroscopic studies of wood-drying processes," *Opt. Exp.* **14**, 3641–3653 (2006).

329. L. Persson, H. Gao, M. Sjöholm, and S. Svanberg, "Diode laser absorption spectroscopy for studies of gas exchange in fruits," *Opt. Laser Eng.* **44**, 687–698 (2005).

330. U. Tylewicz, P. Lundin, L. Cocola, K. Dymek, P. Rocculi, S. Svanberg, P. Dejmek, and F. G. Galindo, "Gas in scattering media absorption spectroscopy (GASMAS) detected persistent vacuum in apple tissue after vacuum impregnation," *Food Biophys.* **7**, 28–34 (2012).

331. M. Lewander, Z. Guan, L. Persson, A. Olsson, and S. Svanberg, "Food monitoring based on diode laser gas spectroscopy," *Appl. Phys. B* **93**, 619–625 (2008).

332. P. Lundin, L. Cocola, M. Lewander, A. Olsson, and S. Svanberg, "Non-intrusive headspace gas measurements by laser spectroscopy – Performance validation by a reference sensor," *J. Food Eng.* **111**, 612–617 (2012).

333. T. Svensson, M. Andersson, L. Rippe, S. Svanberg, S. Andersson-Engels, J. Johansson, and S. Folestad, "VCSEL-based oxygen spectroscopy for structural analysis of pharmaceutical solids," *Appl. Phys. B* **90**, 345–354 (2008).

334. L. Persson, M. Andersson, M. Cassel-Engquist, K. Svanberg, and S. Svanberg, "Gas monitoring in human sinuses using tunable diode laser spectroscopy," *J. Biomed. Opt.* **12**, 054001 (2007).

335. M. Lewander, Z. Guan, K. Svanberg, and S. Svanberg, "Clinical system for non-invasive in situ monitoring of gases in the human paranasal sinuses," *Opt. Exp.* **17**, 10849–10863 (2009).

336. M. Lewander, S. Lindberg, T. Svensson, R. Siemund, K. Svanberg, and S. Svanberg, "Non-invasive diagnostics of the maxillary and frontal sinuses based on diode laser gas spectroscopy," *Rhinology* **50**, 26–32 (2012).

337. S. Lindberg, M. Lewander, T. Svensson, R. Siemund, K. Svanberg, and S. Svanberg, "Method for studying gas composition in the human mastoid cavity by use of laser spectroscopy," *Ann. Oto. Rhinol. Laryn.* **121**, 217–223 (2012).

338. M. Lewander, A. Bruzelius, S. Svanberg, K. Svanberg, and V. Fellman, "Nonintrusive gas monitoring in neonatal lungs using diode laser spectroscopy: Feasibility study," *J. Biomed. Opt.* **16**, 127002 (2011).

339. P. Lundin, E. K. Svanberg, L. Cocola, M. Lewander Xu, S. Andersson-Engels, J. Jahr, V. Fellman, K. Svanberg, and S. Svanberg, "Noninvasive monitoring of gas in the lungs and intestines of newborn infants using diode lasers: Feasibility study," *J. Biomed. Opt.* **18**, 127005 (2013).

340. T. Svensson and Z. J. Shen, "Laser spectroscopy of gas confined in nanoporous materials," *Appl. Phys. Lett.* **96**, 021107 (2010).

341. T. Svensson, M. Lewander, and S. Svanberg, "Laser absorption spectroscopy of water vapor confined in nanoporous alumina: Wall collision line broadening and gas diffusion dynamics," *Opt. Exp.* **18**, 16460–16473 (2010).

342. C. T. Xu, M. Lewander, S. Andersson-Engels, E. Adolfsson, T. Svensson, and S. Svanberg, "Wall-collision line broadening of molecular oxygen within nanoporous materials," *Phys. Rev. A* **84**, 042705 (2011).

343. T. Svensson, E. Adolfsson, M. Burresi, R. Savo, C. T. Xu, D. S. Wiersma, and S. Svanberg, "Pore size assessment based on wall collision broadening of spectral lines of confined gas: Experiments on strongly scattering nanoporous ceramics with fine-tuned pore sizes," *Appl. Phys. B* **110**, 147–154 (2013).

344. S. Svanberg, "Optical analysis of trapped gas – Gas in scattering media absorption spectroscopy," *Laser Phys.* **20**, 68–77 (2010).

345. S. Svanberg, "Gas in scattering media absorption spectroscopy From basic studies to biomedical applications," *Laser and Photonics Reviews* **7**, 779–796 (2013).

346. M. Lewander, *Laser Absorption Spectroscopy of Gas in Scattering Media*, Ph.D. thesis, Lund University (2010).

347. M. Andersson, R. Grönlund, L. Persson, M. Sjöholm, K. Svanberg, and S. Svanberg, "Laser spectroscopy of gas in scattering media at scales ranging from kilometers to millimeters," *Laser Phys.* **17**, 893–902 (2007).

348. Z. G. Guan, M. Lewander, R. Grönlund, H. Lundberg, and S. Svanberg, "Gas analysis within remote porous targets using lidar multi-scatter techniques," *Appl. Phys. B* **93**, 657–663 (2008).

349. D. W. Richerson, *The Magic of Ceramics* (Wiley/American Ceramic Society, Hoboken, N.J., 2012), 2nd ed.

350. C. B. Carter and M. G. Norton, *Ceramic Materials: Science and Engineering* (Springer, New York, 2013), 2nd ed.

351. I. J. Church and A. L. Parsons, "Modified atmosphere packaging technology – A review," *J. Sci. Food Agr.* **67**, 143–152 (1995).

352. C. A. Phillips, "Review: Modified atmosphere packaging and its effects on the microbiological quality and safety of produce," *Int. J. Food Sci. Tech.* **31**, 463–479 (1996).

353. L. P. Kou, E. R. Turner, and Y. G. Luo, "Extending the shelf life of edible flowers with controlled release of 1-methylcyclopropene and modified atmosphere packaging," *J. Food Sci.* **77**, S188–S193 (2012).

354. O. J. Caleb, P. V. Mahajan, F. A. Al-Said, and U. L. Opara, "Modified atmosphere packaging technology of fresh and fresh-cut produce and the microbial consequences – A review," *Food Bioprocess Tech.* **6**, 303–329 (2013).

355. L. Persson, E. Kristensson, L. Simonsson, and S. Svanberg, "Monte Carlo simulations related to gas-based optical diagnosis of human sinusitis," *J. Biomed. Opt.* **12**, 054002 (2007).

356. A. Buck, "New equations for computing vapor-pressure and enhancement factor," *J. Appl. Meteorol.* **20**, 1527–1532 (1981).

357. L. P. Giver, B. Gentry, G. Schwemmer, and T. D. Wilkerson, "Water-absorption lines, 931-961 nm – Selected intensities, N_2-collision-broadening coefficients, self-broadening coefficients, and pressure shifts in air," *J. Quant. Spectrosc. Rad. Transf.* **27**, 423–436 (1982).

358. S. Langlois, T. P. Birbeck, and R. K. Hanson, "Temperature-dependent collision-broadening parameters of H_2O lines in the 1.4-μm region using diode-laser absorption-spectroscopy," *J. Mol. Spectrosc.* **167**, 272–281 (1994).

359. J. Rouquerol, D. Avnir, C. W. Fairbridge, D. H. Everett, J. H. Haynes, N. Pernicone, J. D. F. Ramsay, K. S. W. Sing, and K. K. Unger, "Recommendations for the characterization of porous solids," *Pure Appl. Chem.* **66**, 1739–1758 (1994).

360. S. Lowell, *Characterization of Porous Solids and Powders: Surface Area, Pore Size, and Density*, Particle Technology Series (Springer, Boston, 2006).

361. N. K. Kanellopoulos, *Nanoporous Materials: Advanced Techniques for Characterization, Modeling, and Processing* (CRC Press, Boca Raton, Fla., 2011).

362. Z. Y. Gao, Q. H. Hu, and H. C. Liang, "Gas diffusivity in porous media: Determination by mercury intrusion porosimetry and correlation to porosity and permeability," *J. Porous Media* **16**, 607–617 (2013).

363. S. Westermarck, A. M. Juppo, K. Koiranen, and J. Yliruusi, "Mercury porosimetry of pharmaceutical powders and granules," *J. Porous. Mat.* **5**, 77–86 (1998).

364. S. P. Rigby, R. S. Fletcher, and S. N. Riley, "Characterisation of porous solids using integrated nitrogen sorption and mercury porosimetry," *Chem. Eng. Sci.* **59**, 41–51 (2004).

365. M. Yates, "Application of mercury porosimetry to predict the porosity and strength of ceramic catalyst supports," *Part. Part. Syst. Char.* **23**, 94–100 (2006).

366. H. Giesche, "Mercury porosimetry: A general (practical) overview," *Part. Part. Syst. Char.* **23**, 9–19 (2006).

367. S. Lowell and J. E. Shields, "Equivalency of mercury porosimetry and gas-adsorption," *Powder Technol.* **29**, 225–231 (1981).

368. K. S. W. Sing, "The use of gas-adsorption for the characterization of porous solids," *Colloid. Surface.* **38**, 113–124 (1989).

369. M. C. Mittelmeijer-Hazeleger and J. M. Martin-Martinez, "Microporosity development by CO_2 activation of an anthracite studies by physical adsorption of gases, mercury porosimetry, and scanning electron microscopy," *Carbon* **30**, 695–709 (1992).

370. E. V. Kogan, Y. M. Volfkovich, V. V. Kulakov, A. M. Kenigfest, V. V. Avdeev, V. E. Sosenkin, and N. F. Nikol'skaya, "Porous structure of carbon-carbon friction composites studied by gas adsorption and standard contact porosimetry techniques," *Inorg. Mater.* **48**, 676–679 (2012).

371. V. Felix, Y. Jannot, and A. Degiovanni, "A thermal porosimetry method to estimate pore size distribution in highly porous insulating materials," *Rev. Sci. Instrum.* **83**, 054903 (2012).

372. A. C. Alvarez, N. Passe-Coutrin, and S. Gaspard, "Determination of the textural characteristics of carbon samples using scanning electronic microscopy images: Comparison with mercury porosimetry data," *Adsorption* **19**, 841–850 (2013).

373. W. B. Lindquist, A. Venkatarangan, J. Dunsmuir, and T. F. Wong, "Pore and throat size distributions measured from synchrotron X-ray tomographic images of Fontainebleau sandstones," *J. Geophys. Res. - Sol. Earth* **105**, 21509–21527 (2000).

374. D. J. Bergman, "Dielectric-constant of a composite-material – Problem in classical physics," *Phys. Rep.* **43**, 378–407 (1978).

375. D. A. G. Bruggeman, "Calculation of various physics constants in heterogenous substances. I. Dielectricity constants and conductivity of mixed bodies from isotropic substances," *Ann. Phys.- Berlin* **24**, 636–664 (1935).

376. J. C. M. Garnett, "Colours in metal glasses and in metallic films," *Philos. Trans. R. Soc. Lond.* **203**, 385–420 (1904).

377. H. Looyenga, "Dielectric constants of heterogeneous mixtures," *Physica* **31**, 401–406 (1965).

378. N. A. Clark, J. H. Lunacek, and G. B. Benedek, "A study of Brownian motion using light scattering," *Am. J. Phys.* **38**, 575–585 (1970).